Distribution Agreement

Signature:

______________________________ _______________
Qiongyi Shang Date

Interfacial Charge Transfer in $CsPbI_3$ Perovskite Quantum Dots

By

Qiongyi Shang
Doctor of Philosophy

Chemistry

Tianquan Lian
Advisor

Brian Dyer
Committee Member

Craig L. Hill
Committee Member

Accepted:

Lisa A. Tedesco, Ph.D.
Dean of the James T. Laney School of Graduate Studies

Date

Interfacial Charge Transfer in $CsPbI_3$ Perovskite Quantum Dots

By

Qiongyi Shang
B.S., Zhejiang University, 2014

Advisor: Tianquan Lian, PhD

An abstract of
A dissertation submitted to the Faculty of the
James T. Laney School of Graduate Studies of Emory University
in partial fulfillment of the requirements for the degree of
Doctor of Philosophy
in Chemistry
2019

Abstract

Interfacial Charge Transfer in $CsPbI_3$ Perovskite Quantum Dots

By Qiongyi Shang

$CsPbI_3$ perovskite quantum dots (QDs) are of great interests in their light-harvesting and emitting properties. Notably, $CsPbI_3$ QD solar cell (with a reported efficiency of 13.43% and high stability) is a promising device platform for further improvement. Understanding the charge carrier dynamics in $CsPbI_3$ QDs may provide some relevant insights to develop high-performance photovoltaic devices more rationally. In this dissertation, we put efforts to measure the interfacial charge transfer rates involving $CsPbI_3$ QDs by visible ultrafast transient absorption (TA) spectroscopy.

To resolve the factors that influence charge transfer rates, we studied QD-electron acceptor systems in both solution phase and solid phase. In thin-film solid phase, the photochemical interaction between QDs and metal oxide nanoparticles is directly related to the performance of photovoltaic devices. In solution phase, because nonpolar solvent environment is benign to the QDs, we can reveal the photochemical properties of perovskite QDs more easily.

In solution phase study, we investigated the influence of anion composition and QD size on charge transfer rates in $CsPbI_3$ QD-Rhodamine B (RhB) complex systems. By replacing the iodide partially or fully by bromide, the charge separation (CS) and charge recombination (CR) rates decrease significantly. By decreasing the size of $CsPbI_3$ QDs, the CS and CR rates of QD-RhB complexes increase, which is primarily due to the increase of electronic coupling strength.

In thin-film study, we measured the charge transfer rates between $CsPbI_3$ QDs and metal oxide nanoparticle films by TA and time-resolved photoluminescence (PL) spectroscopy. We found that both the CS and CR rates at QD/TiO_2 interface were ~5-10 times faster than those at QD/ZnO interface, suggesting that these processes depend sensitively on the nature of electron extraction layer material. We also measured the CS and CR rates in QD-TiO_2 films with QDs treated by different post-synthesis purification methods. With methyl acetate (MeOAc) wash, the CS rate increased while the CR rate decreased, compared to the direct precipitate QDs, indicating that removal of surface ligands using MeOAc wash was beneficial to the performance of $CsPbI_3$ QD solar cells.

Interfacial Charge Transfer in $CsPbI_3$ Perovskite Quantum Dots

By

Qiongyi Shang
B.S., Zhejiang University, 2014

Advisor: Tianquan Lian, PhD

A dissertation submitted to the Faculty of the
James T. Laney School of Graduate Studies of Emory University
in partial fulfillment of the requirements for the degree of
Doctor of Philosophy
in Chemistry
2019

Table of Content

Chapter 1. Introduction 1

1.1. Motivation to understand charge transfer dynamics in $CsPbI_3$ QDs 1

1.2. Factors that influence charge transfer dynamics........ 2

1.3. Charge transfer study on $CsPbI_3$ QDs in organic solutions 5

1.4. Charge transfer study on $CsPbI_3$ QDs in solid films 6

1.5. Conclusion........ 7

Chapter 2. Experimental methods........ 8

2.1. Sample preparations........ 8

2.1.1. Perovskite QDs and CdSe QDs synthesis in Chapter 3 8

2.1.2. Sample preparations in chapter 4........ 11

2.1.3 Synthesis of $CsPbI_3$ QDs with different sizes in Chapter 5 13

2.1.4 Sample preparations in Chapter 6........ 14

2.1.5 QDs with different post-synthesis treatments in Chapter 7........ 16

2.2. Time-resolved spectroscopy 16

2.2.1. Visible femtosecond transient absorption setup 16

2.2.2 Visible nanosecond transient absorption setup 17

2.2.3. Static PL and Time-resolved PL decay measurements........ 18

Chapter 3. Effect of residual PbI_2 in $CsPbI_3$ QDs........ 19

3.1. Introduction 19

3.2. The influence of QDs size distribution on PLE spectra........ 19

3.2.1. PLE measurement without considering the size distribution of QDs........ 19

3.2.2. PLE measurement considering the size distribution of QDs 21

3.3. Influence of PbI_2 in $CsPbI_3$ QDs........ 22

3.4. Conclusion........ 25

Chapter 4. Anion composition dependent charge transfer in $CsPbI_3$ QDs........ 26

4.1. Introduction 26

4.2. Results and discussion 27

4.2.1. Characterization of perovskite QDs 27

4.2.2. Electron transfer and charge recombination kinetics in $CsPbBr_3$ QDs........ 29

4.2.3. Electron transfer and charge recombination kinetics in $CsPbBr_{0.75}I_{2.25}$ and $CsPbI_3$ QDs ..32

4.2.4. Hole transfer from $CsPbX_3$ QDs to PTZ 35

4.3. Conclusion 38

Appendix 1. Kinetics fitting in free $CsPbX_3$ QDs 39

Appendix 2. Kinetics fitting in QD-RhB complexes 40

Appendix 3. PL decay kinetics fitting in QD-PTZ complexes 47

Chapter 5. Size dependent charge transfer in $CsPbI_3$ QDs 50

5.1. Introduction 50

5.2. Results and discussion 52

5.2.1. Sample characterizations 52

5.2.2. TA study of $CsPbI_3$ QD-RhB complexes 53

5.2.3. Theoretical calculation of charge transfer rates 58

5.3. Conclusion 63

Appendix 1. XB kinetics fitting model 65

Chapter 6. Charge transfer at the interface of $CsPbI_3$ QDs and metal oxide layer 69

6.1. Introduction 69

6.2. Results and discussion 70

6.2.1. Sample characterizations 70

6.2.2. TA study of charge transfer in $CsPbI_3$ QD-metal oxide films 72

6.2.3. Analysis of PL decay and XB kinetics 73

6.2.4. Implications on perovskite thin-film solar cells 75

6.3. Conclusion 76

Appendix 1. Pump power dependent TA measurements 77

Appendix 2. XB kinetics fitting in QD-Metal oxide NP films 80

Appendix 3. PL decay kinetics fitting 85

Chapter 7. Charge transfer study on $CsPbI_3$ QD-TiO_2 films and the influence of different post-synthesis treatments 87

7.1. Introduction 87

7.2. Results and discussion 89

7.2.1. Sample characterizations 89

7.2.2. TA study on QD-TiO_2 films 93

7.2.3. Analysis of PL decay and XB kinetics 95

7.2.4. Implications on perovskite QD devices 97

7.3. Conclusion 98

Appendix 1. FTIR of films adsorbed with ligands 99
Appendix 2. Electron and hole contribution to XB 100
Appendix 3. XB kinetics and PL decay kinetics fitting in QD-Metal oxide NP films 103
Chapter 8. Summary 103
References 109

List of Figures

Figure 1.1. Structure of a thin-film solar cell and possible charge carrier transfer pathways. ET: electron transfer; HT: hole transfer; CR: charge recombination……………………………………...2

Figure 1.2. Schematic energy level diagram and charge separation and recombination pathways at the $CsPbI_3$ QD-Rhodamine B interface: conduction band (CB) and valence band (VB) edges in $CsPbI_3$, charge separation (CS) between QD and RhB (blue arrow), charge recombination (CR) process (green arrow), and electron-hole recombination inside the QD (dashed grey arrow) 5

Figure 1.3. Left: A sketch illustration of a mesoporous TiO_2 film deposited with $CsPbI_3$ QDs. Right: Schematic energy level diagram and charge separation and recombination pathways at the $CsPbI_3$ QD/TiO_2 NP Interface: conduction band (CB) and valence band (VB) edges in $CsPbI_3$, TiO_2 and Al_2O_3 (black horizontal solid lines), charge separation (CS) from QD to TiO_2 (dark blue arrows), charge recombination (CR) process (green arrow), and electron-hole recombination inside the QD (dashed grey arrow)..6

Figure 2.1. Characterizations of nanocrystals used in Chapter 3: a), c), e), g) are TEM images of CdSe, $CsPbBr_3$, $CsPb(Br/I)_3$, $CsPbI_3$ quantum dots, respectively. Scale bar is 50 nm. b), d), f), h) are normalized absorption and photoluminescence spectra of CdSe, $CsPbBr_3$, $CsPb(Br/I)_3$, $CsPbI_3$ quantum dots, respectively..10

Figure 2.2 TEM images of $CsPbBr_3$ QDs (a), $CsPbBr_{0.75}I_{2.25}$ QDs (b), and $CsPbI_3$ QDs (c) along with corresponding size distribution histograms measured along the long edge and short edge...................12

Figure 2.3. Size distribution histograms of $CsPbI_3$ QDs with three different average edge lengths...14

Figure 2.4. Size distribution histograms of $CsPbI_3$ QDs measured along the long edge (left panel) and short edge (right panel) 14

Figure 2.5. (a) Photograph of the $CsPbI_3$ QD-metal oxide nanoparticle films. (b) Absorption spectra of blank Al_2O_3 NP film (black line) and QD-Al_2O_3 NP film (red line). The obvious non-zero OD value of blank Al_2O_3 NP film is due to light reflection and scattering. (c) Absorption spectra of blank ZnO NP film (black line) and QD-ZnO NP film (red line). (d) Absorption spectra of blank TiO_2 NP film (black line) and QD- TiO_2 NP film (red line) 15

Figure 3.1. Abpt and scaled PLE spectra. a) absorptance spectrum (solid line) and PLE spectrum (dashed line) of CdSe QDs solution. b), c), d) are absorptance spectra (solid line) and PLE spectra (dashed line) of $CsPbBr_3$, $CsPb(Br/I)_3$, $CsPbI_3$ QDs solutions, respectively..20

Figure 3.2. Abpt and PLE comparison after considering size distribution of QDs. a) Normalized PL spectra of CdSe, $CsPb(Br/I)_3$ and $CsPbI_3$ QDs. The arrows point to the five emission wavelengths at which we measured PLE. b), c), d) are absorptance spectra (solid line) and scaled average PLE spectra (dashed line) of CdSe, $CsPb(Br/I)_3$, $CsPbI_3$ QDs solutions, respectively...22

Figure 3.3. UV-Vis absorption and TA study on $CsPbI_3$ QDs, PbI_2 and their mixture. a) UV-Vis spectra of $CsPbI_3$ QDs, PbI_2 and the mixture. b) TA spectra of $CsPbI_3$ QDs pumped by 400 nm femtosecond laser pulses at indicated delay time. XB: exciton bleach signal; PA: photoinduced absorption signal. c) and d) Normalized XB kinetics (c) and PA kinetics (d) of $CsPbI_3$ QDs and QDs + PbI_2 mixture. e) TA spectra of PbI_2 precursor solution pumped by 400 nm laser pulses at indicated delay time. f) The decay kinetics of PA signal in PbI_2 solution...24

Figure 4.1. Energy level diagram of $CsPbX_3$ QD-RhB and QD-PTZ complexes and possible charge transfer pathways. Black solid lines: CB and VB edges of perovskite QDs. Grey dashed arrow: exciton recombination in QD. ET: electron transfer; HT: hole transfer; CR: charge recombination...............27

Figure 4.2. (a) UV-Vis absorption, (b) normalized PL spectra and (c) normalized PL decay curves of $CsPbBr_3$ QDs, mixed anion perovskite QDs and $CsPbI_3$ QDs in heptane. (d) Calculated band edge positions of $CsPbBr_3$ QDs, $CsPbBr_{0.75}I_{2.25}$ QDs and $CsPbI_3$ QDs..28

Figure 4.3. (a) UV-Vis absorption spectra of $CsPbBr_3$ QDs without (black line) and with (red line) RhB molecules attached on surfaces. Inset: absorption spectra zoomed in from 520 to 610 nm, showing the static absorption of RhB on QDs with a peak around 555 nm. (b) TA spectra of free $CsPbBr_3$ perovskite QDs measured with 400 nm excitation at indicated delay time from 1 ps to 300 ns. Exciton bleach (XB) feature is labeled. (c) TA spectra of $CsPbBr_3$ QD-RhB complexes measured with 400 nm excitation at indicated delay time from 1 ps to 10 us. Exciton bleach (XB) and the reduced RhB features are labeled. Inset shows the enlarged RhB ground state bleach signal at indicated delay time. (d) XB recovery kinetics of free $CsPbBr_3$ QDs (green line), XB recovery kinetics of $CsPbBr_3$ QD-RhB complexes (blue square dots) and RhB ground state bleach signal formation and decay kinetics (red round dots). The RhB signal kinetics curve is scaled to match the XB recovery at the charge recombination stage. Black solid lines are multi-exponential fits...30

Figure 4.4. UV-Vis absorption spectra of $CsPbBr_{0.75}I_{2.25}$ (left panel) and $CsPbI_3$ QDs (right panel) with and without RhB in heptane. Inset: The absorption spectra of RhB on QD surfaces by subtracting the free QDs absorption from the QD-RhB complexes absorption...33

Figure 4.5. (a) TA spectra of $CsPbBr_{0.75}I_{2.25}$ QDs and (b) $CsPbI_3$ QDs without (upper) and with RhB (lower) measured with 500 nm excitation at indicated delay time. (c) TA kinetics of free $CsPbBr_{0.75}I_{2.25}$ QDs and QD-RhB complexes: XB recovery kinetics of free QDs (green line), XB recovery kinetics of QD-RhB complexes (blue square dots) and RhB ground state bleach signal formation and decay kinetics (red round dots). The RhB signal kinetics is scaled to match the XB recovery at the charge recombination stage. Black solid lines are multi-exponential fits. (d) TA kinetics of free $CsPbI_3$ QDs and QD-RhB complexes with the same denotations in (c)...35

Figure 4.6 (a) UV-Vis absorption spectra of $CsPbBr_3$ QDs with PTZ concentration from 0 to 3.2 mM. The grey arrow indicates the increasing [PTZ]. (b) PL decay curves of solutions in (a), showing that PL decays faster as [PTZ] increases. Black solid lines are multiexponential fittings of each decay curve. (c) Normalization of PL decay curves at the tail to extract the average PTZ/QD ratio. (d) Plot of the half-lives with different PTZ/QD ratios in $CsPbBr_3$ QD-PTZ samples......................................37

Figure A.4.1. The charge transfer and recombination processes in $CsPbX_3$ QD-RhB complexes......41

Figure A.4.2. XB recovery kinetics in $CsPbBr_3$-RhB (blue squares), $CsPbBr_{0.75}I_{2.25}$-RhB (red dots), and $CsPbI_3$-RhB (green triangles). Black solid lines are fittings with function A.4.16............................43

Figure A.4.3. XB recovery kinetics in $CsPbBr_3$-RhB (blue squares), $CsPbBr_{0.75}I_{2.25}$-RhB (red dots), and $CsPbI_3$-RhB (green triangles). Black solid lines are fittings with function A.4.21 (for $CsPbBr_3$-RhB) or A.4.24 (for $CsPbBr_{0.75}I_{2.25}$-RhB and $CsPbI_3$-RhB) 46

Figure A.4.4. a), b) and c) are UV-Vis absorption spectra of $CsPbX_3$ QDs with increasing PTZ concentration. d), e), and f) are PL decay kinetics of samples in a), b), and c), respectively. Black solid lines are multi-exponential fittings. Arrows indicate the increasing of PTZ concentrations from 0 to 3.2 mM..47

Scheme 5.1. Schematic energy level diagram and charge separation and recombination pathways at the $CsPbI_3$ QD-Rhodamine B Interface: conduction band (CB) and valence band (VB) edges in $CsPbI_3$, charge separation (CS) between QD and RhB (blue arrow), charge recombination (CR) process (green arrow), and electron-hole recombination inside the QD (dashed grey arrow) 51

Figure 5.1. Morphology and optical properties of $CsPbI_3$ perovskite QDs. Absorption (black) and emission (red) spectra (a,b,c) and corresponding TEM images (d,e,f) of three QDs of average sizes of (a,d)11.8±1.6 nm, (b,e) 10.8±1.5 nm and (c,f) 6.5±1.1 nm; scale bars in (d-f): 50 nm…………………..53

Figure 5.2. TA spectra and kinetics of $CsPbI_3$ QD-RhB complexes. (a) UV-Vis absorption spectra of 676 QDs-RhBn, n=1-5 with increasing RhB loading amount. TA spectra of free 676 QDs (b) and 676 QD-RhB5 complexes (c) measured with 500 nm excitation at indicated delay times from 1 ps to 2 μs. XB and RhB indicate exciton bleach and RhB ground state bleach features, respectively. (d) XB kinetics of free $CsPbI_3$ QDs (brown squares), XB kinetics of QD-RhB1 to QD-RhB5 and kinetics of

RhB ground state bleach (black hollow dots) in QD-RhB5. The RhB signal has been scaled to match the XB recovery at the charge recombination stage. Also shown are fitting results according to the model in Appendix 1 (black solid lines) 55

Figure 5.3. Absorption spectra of 665 QD-RhBn series (left panel) and 650 QD-RhBn series (right panel) 56

Figure 5.4. TA study of smaller size QDs. (a), (c) TA spectra of free 665 QDs (a) and free 650 QDs (c) measured with 500 nm excitation at indicated delay time from 1 ps to 2 μs. (b) XB kinetics of free 665 QDs (brown squres) and XB kinetics of 665 QD-RhB series. (d) XB kinetics of free 650 QDs (brown squres) and XB kinetics of 650 QD-RhB series. Black solid fitting results according to the model in Appendix 1..........57

Figure 5.5. Size dependent charge separation (CS) and charge recombination (CR) rates at 300K. Filled circles and squares are the experimental values extracted from XB kinetics (Table 5.1). The lines with open circles and squares are piecewise linear interpolations of the unscaled ($\alpha = 1$) theoretical calculation results (Eq. 5.2). with λ_{QD} variationally determined to be 40 meV..........62

Figure 5.6. Squared overlaps of the electron and hole wavefunctions (ψ) with the LUMO plotted as functions of the inverse volume of the QD, data taken from Table 5.2..........63

Scheme 6.1. Schematic energy level diagram and charge separation and recombination pathways at the $CsPbI_3$ QD/metal oxide (MO) NP Interface: conduction band (CB) and valence band (VB) edges in $CsPbI_3$, TiO_2, ZnO and Al_2O_3 (black horizontal solid lines), electron transfer (ET) from QD to MO (dark blue arrows), back charge recombination (CR) process (green arrow), and electron-hole recombination inside the QD (dashed grey arrow) 70

Figure 6.1. Absorption spectrum and TEM image of $CsPbI_3$ perovskite QDs. (a) Absorption (black solid line) and photoluminescence (red dashed line) spectra of $CsPbI_3$ QDs dispersed in heptane. Inset:

Photograph of QD-MO NP films. (b) Representative TEM image of QDs. The average edge size is 12.7 nm……………………………………………………………………………………...71

Figure 6.2. TA spectra and kinetics of $CsPbI_3$ perovskite QDs on metal oxide NP films measured with 500 nm excitation. TA spectra of $CsPbI_3$ QDs on Al_2O_3 (a), ZnO (b) and TiO_2 (c) NP films at indicated time delays after 500 nm excitation. The dominant signal is exciton bleach (XB) peaked at ~680 nm. (d) Comparison of XB recovery kinetics of $CsPbI_3$ QDs on Al_2O_3 (blue squares), ZnO (red circles) and TiO_2 (green triangles) NP films. Black solid lines are multi-exponential fits according to the model provided in Appendix 2..73

Figure 6.3. PL decay kinetics of $CsPbI_3$ QDs on MO. a) Comparison of PL decay on Al_2O_3, ZnO and TiO_2. b-d) Comparison of PL decay (red) and XB kinetics (black) on b) Al_2O_3, c) ZnO and d) TiO_2. Green curve in panel b) is the XB kinetics of QDs in solution..74

Figure A.6.1. TA spectra of $CsPbI_3$ QDs on Al_2O_3 NP film measured at different excitation densities. The right bottom panel compares the XB recovery kinetics at different excitation densities..............77

Figure A.6.2. TA spectra of $CsPbI_3$ QDs on ZnO NP film measured at different excitation densities. The right bottom panel compares the XB recovery kinetics at different excitation densities...............78

Figure A.6.3. TA spectra of $CsPbI_3$ QDs on TiO_2 NP film measured at different excitation densities. The right bottom panel compares the XB recovery kinetics at different excitation densities................78

Figure A.6.4. Linear dependence of XB signal amplitudes on excitation densities within single exciton region. The different slopes for three film samples are due to the optical density differences of QDs (Figure 2.5) 79

Figure A.6.5. The charge transfer and recombination processes in $CsPbI_3$ QD-MO NP films.........81

Figure A.6.6. XB recovery kinetics of QDs on ZnO and TiO_2 NP films. Black solid lines are fits by equation A.6.7..83

Figure A.6.7. Scaled PL decay curves of QDs on ZnO and TiO_2 NP films. Black solid lines are bi-exponential decay fits..85

Scheme 7.1. Schematic energy level diagram and charge separation and recombination pathways at the $CsPbI_3$ QD/TiO_2 NP interface: conduction band (CB) and valence band (VB) edges in $CsPbI_3$, TiO_2 and Al_2O_3 (black horizontal solid lines), charge separation (CS) from QD to TiO_2 (dark blue arrows), charge recombination (CR) process (green arrow), and electron-hole recombination inside the QD (dashed grey arrow) 89

Figure 7.1. Spectroscopic and TEM characterization of QDs. a) UV-vis absorption spectra of original QDs and washed QDs in hexane. b) and c) TEM images of original QDs and washed QDs. Scale bar: 50 nm. Insets are size distribution statistics. d) PL spectra of QD solutions in a). Inset is the normalized spectra. e) PL decay kinetics of QD solutions in a), excited at 490 nm. f) FTIR spectra of original QDs and washed QDs spin-coated on the sapphire windows. The amplitudes have been corrected with QD absorption at 680 nm to compare the ligand quantity on QDs……………………………………90

Figure 7.2. FTIR spectra of QDs on a) ALD TiO_2 and b) TiO_2 films prepared with (QD washed) and without (QD original) post-synthesis MeOAc wash of QDs. The amplitudes have been scaled with QD absorption at 680 nm to compare the relative ligand quantities. Insets are photos of the QD sensitized films………………………………………………………………………………92

Figure 7.3. a), b), d) and e) UV-vis absorption of films before and after QD adsorption. c) and f) Absorption spectra of QDs on the film after scattering subtraction...92

Figure 7.4. TA spectra and kinetics of $CsPbI_3$ perovskite QDs on metal oxide films measured with 500 nm excitation. TA spectra of original QDs on (a) ALD TiO_2 and (b) TiO_2 films at indicated time delays after 500 nm excitation. c) Comparison of XB recovery kinetics of original QDs on ALD TiO_2 (blue squares) and TiO_2 (red circles) films. TA spectra of washed QDs on (d) ALD TiO_2 (d) and (e) TiO_2 films at indicated time delays after 500 nm excitation. f) Comparison of XB recovery kinetics of

washed QDs on ALD TiO_2 (blue squares) and TiO_2 (red circles) NP films. Black solid lines are multi-exponential fits according to the model provided in Appendix 3..........94

Figure 7.5. PL decay kinetics of $CsPbI_3$ QDs on NP films. a) and d) Comparison of PL decay on ALD TiO_2 and TiO_2. Black solid lines are fitting of PL decays described in Appendix 3. b), c) and e), f) Comparison of PL decay (red) and XB kinetics (blue) of QDs on NP films. Insets are the dominant processes in each film: exciton recombination or electron transfer and charge recombination..........96

Figure 7.6. The influence of ligand quantity per QD (IR/Vis) on PL decay rates (Data adopted from Table A.7.3). Average PL decay rates vary with IR/Vis value slightly (red line). PL decay rates of QDs on TiO_2 films (blue stars) are far above the red line, indicating the existence of electron transfer process..........97

Figure A.7.1. FTIR spectra of films after soaking in dilute ligand solution for 42 h..........99

Figure A.7.2. TA study of free original QDs and QD-RhB complexes in solution. a) Absorption spectra of free original QDs and QD-RhB complexes. b) TA spectra of free original QDs measured with 500 nm pump at indicated delay time. c) TA spectra of original QD-RhB complexes measured at the same conditions as the free QDs. d) XB kinetics of original QDs and QD-RhB complexes. Black lines are multiexponential fits..........100

Figure A.7.3. TA study of washed QDs and QD-RhB complexes in solution. a) Absorption spectra of washed QDs and QD-RhB complexes. b) TA spectra of free washed QDs measured with 500 nm pump at indicated delay time. c) TA spectra of washed QD-RhB complexes measured at the same conditions as the free QDs. d) XB kinetics of washed QDs and QD-RhB complexes. Black lines are multiexponential fits..........101

Figure A.7.4. Scaled PL decay curves to match the XB kinetics in QD-TiO_2 films. The matching part of XB kinetics is the CS dominant time range..........103

List of Tables

Table 4.1. Fitting results for $CsPbX_3$ QD-RhB XB recovery kinetics......32

Table 4.2. Average ET and CR time constants in QD-RhB and HT time constant in QD-PTZ systems......38

Table A.4.1. Fitting parameters for free $CsPbX_3$ QDs XB recovery kinetics......39

Table A.4.2. Fitting parameters for $CsPbX_3$ QD-RhB complexes XB recovery kinetics......40

Table A.4.3. Fitting parameters for $CsPbX_3$ QD-RhB XB recovery kinetics with A.4.16......44

Table A.4.4. Fitting parameters for $CsPbX_3$ QD-PTZ PL decay curves......48

Table A.4.5. Hole transfer parameters and rates......49

Table 5.1. Size dependent CS and CR time constants in QD-RhB complexes......58

Table 5.2. Orbital overlaps, quantum mechanical coupling factors H (in meV) calculated using Eqs 5.4 and the orbital energies, and driving force ΔG (eV), for cubic $CsPbI_3$ dots of side L (nm). The CB of $CsPbI_3$ is at -3.7 eV, and VB at -5.4 eV. The energy of RhB LUMO is -3.95 eV......60

Table A.5.1. Fitting parameters for XB kinetics of QD and QD-RhB5......65

Table A.5.2. Fitting parameters for XB kinetics of QD-RhB series......68

Table A.6.1. Fitting parameters for XB kinetics in $CsPbI_3$ QD-Metal oxide NP films......80

Table A.6.2. Fitting parameters for XB kinetics in $CsPbI_3$ QD-MO NP films by A.6.7......83

Table A.6.3. Time constants of ET and CR in $CsPbI_3$ QD-MO NP films......84

Table A.6.4. ET efficiencies......84

Table A.6.5. Bi-exponential decay fitting parameters for PL kinetics......86

Table 7.1. IR/Vis values of films determined by FTIR and UV-vis absorption......93

Table A.7.1. Fitting parameters of XB kinetics in original QDs and QD-RhB complexes......101

Table A.7.2. Fitting parameters of XB kinetics in washed QDs and QD-RhB complexes......102

Table A.7.3. PL decay fitting parameters and CS time constants calculated from PL decays............104

Table A.7.4. XB Kinetics fitting in QD-Metal oxide NP films...105

Chapter 1. Introduction

1.1. Motivation to understand charge transfer dynamics in $CsPbI_3$ QDs

Organic-inorganic hybrid lead halide perovskite photovoltaic device was first reported on 2009, with a power conversion efficiency (PCE) of 3.81%.[1] Over the past decade, the PCE has risen to 24.2%,[2] showing the great potential of lead halide perovskites as a new type of solar energy conversion materials. However, the stability of the organic-inorganic hybrid lead halide perovskite structure, which is a main limitation factor of this material for industrial applications, has little improvement in this decade yet.[3] Among the efforts to stabilize the perovskites, incorporating inorganic cations (Cs^+ or Rb^+)[4-6] and using all-inorganic $CsPbI_3$ perovskite[7-9] have been explored as promising alternatives. Recently in 2018, $CsPbI_3$ perovskite solar cells have been reported with PCE of 15.07%[10] and 17.06%.[11] Before these achievements, the best $CsPbI_3$ perovskite solar cells were fabricated with $CsPbI_3$ QDs, with PCE 10.77% and 13.43%, reported in 2016 and 2017, respectively.[7, 12] Notably, $CsPbI_3$ QD solar cell ranked the highest PCE among all quantum dot solar cells until the record was broken at the beginning of 2019.[2]

To help design the device more rationally and further improve the performance, understanding the charge carrier dynamics inside the device are necessary. Figure 1.1 shows the basic thin film photovoltaic device structure and the possible charge transfer (CT) pathways. In a working device, the PCE is determined by the destination of charge carriers. Favorable CT pathways are carrier diffusion, electron transfer (ET) and hole transfer (HT). Unfavorable CT pathways are e-h recombination, carrier trapping and charge recombination (CR) at interfaces. In this dissertation, we mainly focus on studying the ET and CR processes at the interface of $CsPbI_3$ QDs and some factors that may influence the CT processes.

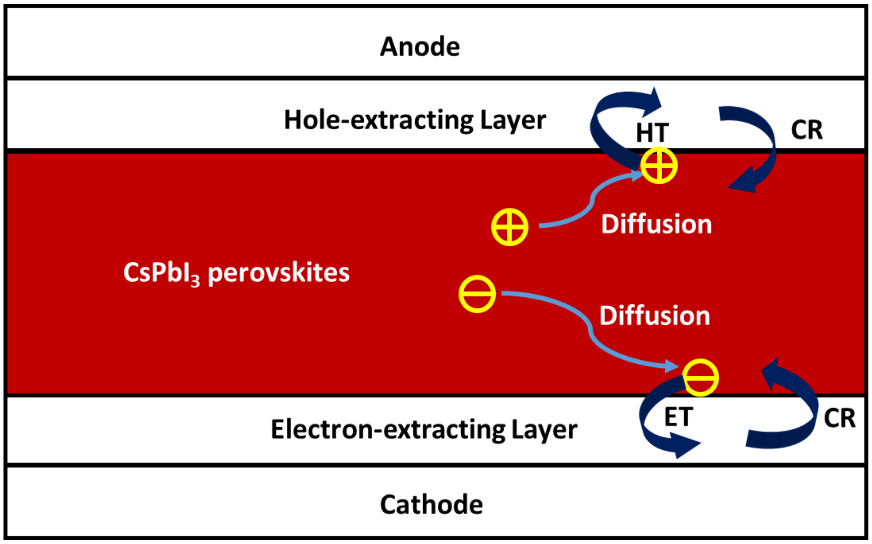

Figure 1.1. Structure of a thin-film solar cell and possible charge carrier transfer pathways. ET: electron transfer; HT: hole transfer; CR: charge recombination.

1.2. Factors that influence charge transfer dynamics

According to Marcus's non-adiabatic electron transfer theory,[13] shown in Eq. 1, the ET rate is controlled by the driving force ΔG, the quantum mechanical coupling strength between the initial and final states $|<i|H|f>|$, and reorganization energy λ. That is, at a constant temperature, any factor that can influence the driving force, electronic coupling strength and reorganization energy will change the resultant electron transfer rate.

$$\frac{1}{\tau(T)} = k(T) = \frac{\pi\left|\langle i|\hat{H}|f\rangle\right|^2}{\hbar\sqrt{\pi\lambda k_B T}}\exp\left[-\frac{(\Delta G+\lambda)^2}{4\lambda k_B T}\right] \tag{1.1}$$

In the above equation, $\tau(T)$ is ET time constant; $k(T)$ is ET rate constant; T is temperature in Kelvin; $\hbar$ is the reduced Planck's constant; k_B is the Boltzmann constant.

For ET or HT at the interface of $CsPbI_3$ QDs, possible influence factors can be categorized as: 1) chemical composition factor; 2) morphology factor; 3) interfacial contact factor; 4) property of electron or hole acceptor; 5) property of the environment; 6) defects and trapping in the nanocrystals and interfaces. Notably, these factors may or may not be independent mutually, especially when comes to perovskite QDs, whose surface and structure are sensitive and prone to change.

1) Chemical composition factor. $CsPbI_3$ QDs consist of Cs^+ cations, Pb^{2+} cations and I^- anions which can be replaced partially or fully by some other ions. For example, Cs^+ can be substituted with Rb^+, methylammonium (MA^+) or formamidinium (FA^+);[14-15] Pb^{2+} can be replaced with Sn^{2+}, Mn^{2+};[16-18] I^- can be replaced with Br^-, Cl^-.[19-20] Changing the chemical composition leads to the shift of the conduction band (CB) and valence band (VB) edge positions, thus changing the ET and CR driving forces. Changing the composition may also change the electronic coupling strength and reorganization energy. Therefore, ion composition is an important factor to influence the charge transfer rates. In chapter 4, we studied the influence of anion composition on the charge transfer rates in $CsPbI_3$ QDs.

2) Morphology factor. The size and shape of quantum dots may also influence the charge transfer rates. The shape of $CsPbI_3$ QDs used in this dissertation are quasi-cubic. We did not study other shapes. For the size factor, on the one hand, QDs with different sizes have different CB and VB energy levels because of quantum confinement effect.[21-23] On the other hand, the surface electronic densities may vary with QD sizes, thus influencing electronic coupling strength between the electron donor and acceptor.[24] Consequently, variable QD size changes the driving force of charge transfer (ΔG) as well as the electronic coupling strength (H), both of which, according to Marcus theory (Eq. 1.1), will change the charge transfer rates.[24-25] In chapter 5, we study the size dependent charge separation (CS) and charge recombination (CR) rates in $CsPbI_3$ QD-RhB systems.

3) Interfacial contact factor. Close contact between charge donor and charge acceptor is necessary for interfacial charge transfer to happen. ET rates will decrease significantly with distance between the donor and acceptor because the electronic coupling will reduce with distance.[26-27] For colloidal nanocrystals, surface ligand is an indispensable part to maintain the stability and quality.[28] Since the ligands are typically long C-H organic chains, so in some systems, the surface ligands may be a hindering factor for charge transfer. When fabricating the photovoltaic device, people tried to eliminate most of the surface ligands.[7] In chapter 7, we study the possible influence of ligand quantity on the ET and CR processes in $CsPbI_3$ QD-TiO_2 films.

4) Property of electron or hole acceptor. The energy level of electron (hole) acceptor can influence the driving force of electron (hole) transfer.[24, 29-30] The different electronic property and geometric structure of electron (hole) acceptor may influence the electronic coupling strength and reorganization energy. So, the property of electron (hole) acceptor is also an important factor that changes charge transfer rates.[30] In chapter 6, we compare the CT rates in $CsPbI_3$ QD-ZnO and $CsPbI_3$ QD-TiO_2 films.

5) Property of the environment. The state of environment may influence the reorganization energy. For example, in solution phase, organic electron acceptor molecules have intramolecular rotational freedom, while in solid phase, they cannot rotate. Also, the dielectric constant of the solvent will influence the reorganization energy of solvent. We did not study this factor experimentally. In the theoretical calculation part of Chapter 5, the dielectric constant of solvent was taken into consideration.

6) Defects and trapping in the nanocrystals and interfaces. Defects and trapping may or may not influence the driving force, electronic coupling strength and reorganization energy. Or at least the influence is very difficult to characterize. However, carrier trapping is a nonnegligible competition for the charge transfer processes. With more charge carriers trapped, the charge transfer process will be less efficient. Therefore, any factor that may influence the trapping will also change the charge transfer efficiency. In this dissertation, we do not study the trapping influence independently. But trapping processes do exist in most systems, especially in the QD-metal oxide films.

1.3. Charge transfer study on $CsPbI_3$ QDs in organic solutions

$CsPbI_3$ QDs are synthesized and preserved in organic solvents, as most colloidal nanocrystals are. Organic solvents such as hexane, heptane and toluene are benign to perovskite QDs coating with oleic acid/oleylamine ligands. $CsPbI_3$ QDs may suffer ligand loss, surface rearrangement, aggregation and degradation to some extent when transferred to solid-state usage. Therefore, studying the charge carrier dynamics in organic solutions can better reflect the intrinsic charge carrier properties of $CsPbI_3$ QDs. Based on previous work, electron acceptors and hole acceptors can be chemically adsorbed onto the QD surface.[24, 31] Figure 1.2 shows a main system we study in this dissertation, the QD-RhB complex. After photo excitation, the electron can recombine with the hole within QD directly or transfer to the LUMO of RhB and recombine with the hole later. The rate difference can be reflected on the exciton bleach (XB) recovery kinetics in transient absorption (TA) spectroscopy. We mainly used the QD-RhB system in solution to study the anion composition dependent and size dependent charge transfer rates.

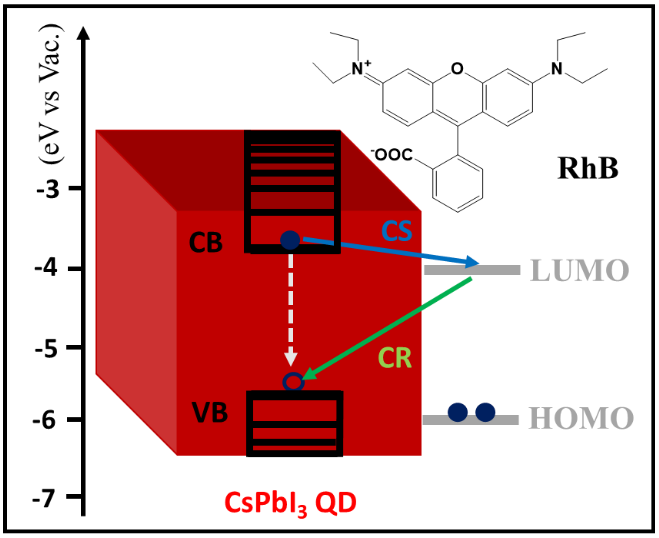

Figure 1.2. Schematic energy level diagram and charge separation and recombination pathways at the $CsPbI_3$ QD-Rhodamine B interface: conduction band (CB) and valence band (VB) edges in $CsPbI_3$,

charge separation (CS) between QD and RhB (blue arrow), charge recombination (CR) process (green arrow), and electron-hole recombination inside the QD (dashed grey arrow).

1.4. Charge transfer study on $CsPbI_3$ QDs in solid films

Since the thin-film solar cells work in solid state, studying charge carrier dynamics in the film is more relevant to understand the mechanism of the photovoltaic device. In the most common structure of perovskite solar cells, the electron-extracting layer is a layer of mesoporous TiO_2 nanocrystals.[7, 12, 32-45] To measure the electron transfer from QDs to TiO_2, we fabricated the mesoporous TiO_2 films and deposited QDs by soaking the films in QD solution. Left panel in Figure 1.3 sketchily illustrated the structure and composition of the films we used. In this type of films, all the QDs can be assumed to be in contact with TiO_2 and stacking of QDs is negligible. To extract charge transfer rates, we used Al_2O_3 film as a controlled experiment, where charge transfer is forbidden because Al_2O_3 is an insulator. See the right panel in Figure 1.3. We conducted TA spectroscopic study on these films and compared the ET and CR rates of QD-ZnO and QD-TiO_2. Also, we studied the influence of different post-synthesis treatments of QDs on the ET and CR rates in QD-TiO_2 films.

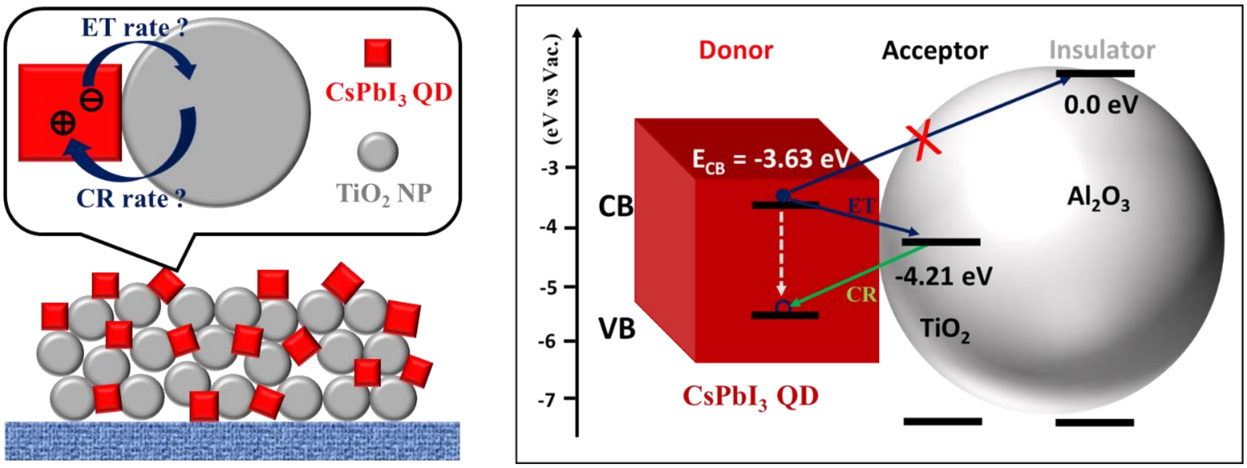

Figure 1.3. Left: A sketch illustration of a mesoporous TiO_2 film deposited with $CsPbI_3$ QDs. Right: Schematic energy level diagram and charge separation and recombination pathways at the $CsPbI_3$ QD/TiO_2 NP Interface: conduction band (CB) and valence band (VB) edges in $CsPbI_3$, TiO_2 and Al_2O_3 (black horizontal solid lines), charge separation (CS) from QD to TiO_2 (dark blue arrows), charge recombination (CR) process (green arrow), and electron-hole recombination inside the QD (dashed grey arrow).

1.5. Conclusion

In conclusion, we have conducted a series of transient absorption spectroscopic study on the charge transfer dynamics involving the $CsPbI_3$ QDs. In the solution phase, we studied the influence of anion composition and QD size on the charge transfer rates. In the solid-state films, we measured the ET and CR rates from QDs to TiO_2 and investigated the influence of metal oxide type and post-synthesis treatment methods. These research works may provide some insights of the $CsPbI_3$ QD involved systems for the future solar energy conversion applications.

The rest of this dissertation is presented as follows: Chapter 2 introduces the experimental procedures, including sample preparations and time-resolved spectroscopic techniques we adopted for the experiments. Chapter 3 briefly summarizes the effect of residual PbI_2 on the absorption and emission properties of $CsPbI_3$ QDs. Chapter 4 studies the anion composition dependent charge transfer in $CsPbI_3$ QDs. Chapter 5 examines the size dependent charge transfer in $CsPbI_3$ QD-RhB complexes. Chapter 6 studies the electron transfer from $CsPbI_3$ QDs to ZnO and TiO_2 nanoparticle films. Chapter 7 investigates the influence of post-synthesis treatment of QDs on the ET and CR rates of QD-TiO_2 couples.

Chapter 2. Experimental methods

2.1. Sample preparations

2.1.1. Perovskite QDs and CdSe QDs synthesis in Chapter 3

Synthesis of $CsPbX_3$ (X = Br, I) QDs. We synthesized $CsPbBr_3$, $CsPb(Br/I)_3$, $CsPbI_3$ QDs following published procedures[19-20, 46]. First step is the preparation of cesuim oleate precursor. 0.407 g Cs_2CO_3, 1.25 mL oleic acid (OA), and 20 mL octadecene (ODE) were loaded into a 50 mL 3-neck flask and heated under Argon atmosphere to 150 ºC until dissolving all the Cs_2CO_3. The Cs-oleate precursor solution was kept at 100 ºC to prevent precipitation of Cs-oleate out of ODE. In another 25 mL 3-neck flask, 0.069 g $PbBr_2$ (0.188 mmol) and 5 mL of ODE were purged by Argon for 30 min at 120 ºC. 0.5 mL OA and 0.5 mL oleylamine (OLAM) were injected into the flask at 120 ºC under Argon atmosphere. After complete dissolution of $PbBr_2$, the temperature was raised to 170 -190 ºC. 0.4 mL of Cs-oleate precursor solution was swiftly injected and the reaction was quenched by an ice-water bath within 10 seconds. The crude solution was purified by centrifugation at 14000 rpm for 15 min to precipitate the aggregated nanocrystals out. The precipitation was re-dispersed in heptane for various spectroscopic studies.

For the synthesis of $CsPbI_3$ QDs, the PbI_2 precursor was 0.087g and the ligands were 0.7 mL OA and 0.7 mL OLAM. Cs-oleate was injected at 180-190 ºC. For the synthesis of $CsPb(Br/I)_3$ QDs, the PbI_2 and $PbBr_2$ precursor were 0.042 g and 0.035 g respectively, and the ligands were 0.6 mL OA and 0.6 mL OLAM. Cs-oleate solution was also injected at 180-190 ºC.

Synthesis of CdSe QDs. We synthesized CdSe QDs following a reported method[47-48]. First, 0.1356 g Cd-stearate (0.1 mmol) was loaded into a 25 mL flask with 3 mL ODE. The mixture was heated to 250 °C after purging by argon for 10 min. 0.5 mL of 0.1 M Se-SUS (selenium powder suspension in

ODE) was swiftly injected into the flask and the reaction temperature was kept at 250 °C for growth of the nanocrystals. After 10 min of growth, more Se-SUS was dropped into the flask slowly for further growth of CdSe QDs. Needle-tip aliquots were taken and dissolved in chloroform for measuring UV−vis absorption spectra until reaching the desired first excitonic absorption peak position. The reaction was quenched by a cold-water bath. In situ purification were conducted according to the published procedure[47-48] and the CdSe nanocrystals were finally dispersed in hexane for further study. Figure 2.1 shows the TEM images and normalized absorption and PL emission spectra of nanocrystals used in Chapter 3.

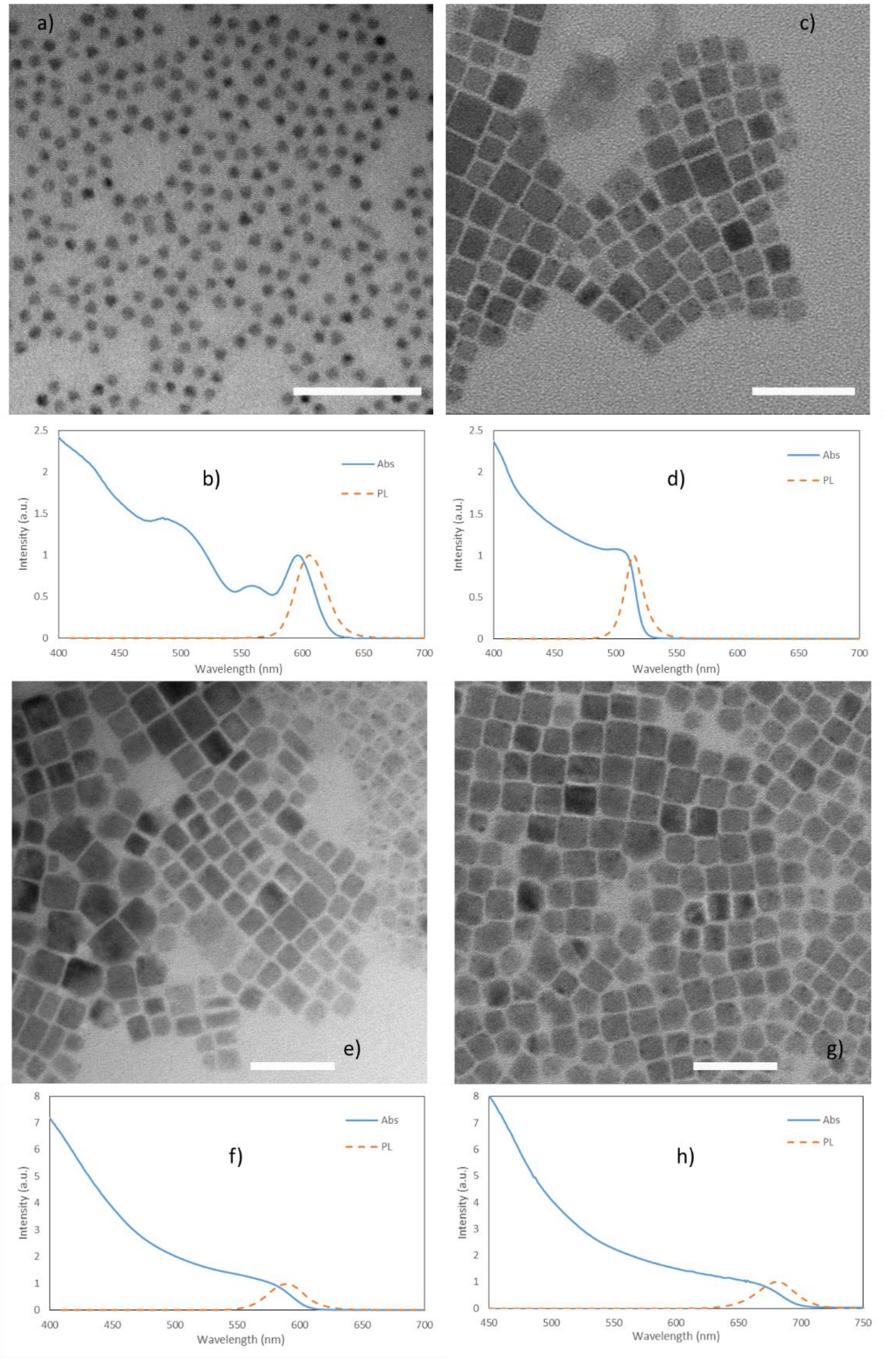

Figure 2.2. Characterizations of nanocrystals used in Chapter 3: a), c), e), g) are TEM images of CdSe, $CsPbBr_3$, $CsPb(Br/I)_3$, $CsPbI_3$ quantum dots, respectively. Scale bar is 50 nm. b), d), f), h) are

normalized absorption and photoluminescence spectra of CdSe, $CsPbBr_3$, $CsPb(Br/I)_3$, $CsPbI_3$ quantum dots, respectively.

2.1.2. Sample preparations in chapter 4

Perovskite QDs synthesis and anion exchange. We synthesized the $CsPbX_3$ (X = Br or I) QDs according to the published methods.[19-20, 31, 46] The procedures have been described in section 2.1.1. To control the anion composition of QDs, room temperature anion exchange reactions were conducted based on reported procedures.[19-20] We adopted inter-particle anion exchange reaction which was conducted by mixing the $CsPbBr_3$ and $CsPbI_3$ QDs heptane solutions directly and stirring for 30 min. No further purification was required for this mixed anion QDs sample. The concentration of as-synthesized $CsPbX_3$ QDs solution was calculated by Beer-Lambert law after estimation of QD extinction coefficients.[31, 49-50] The bromide to iodide ratio was estimated to be 1 to 3. We denote this sample as $CsPbBr_{0.75}I_{2.25}$ QDs. Figure 2.2 shows the TEM images and size statistics of these perovskite QDs.

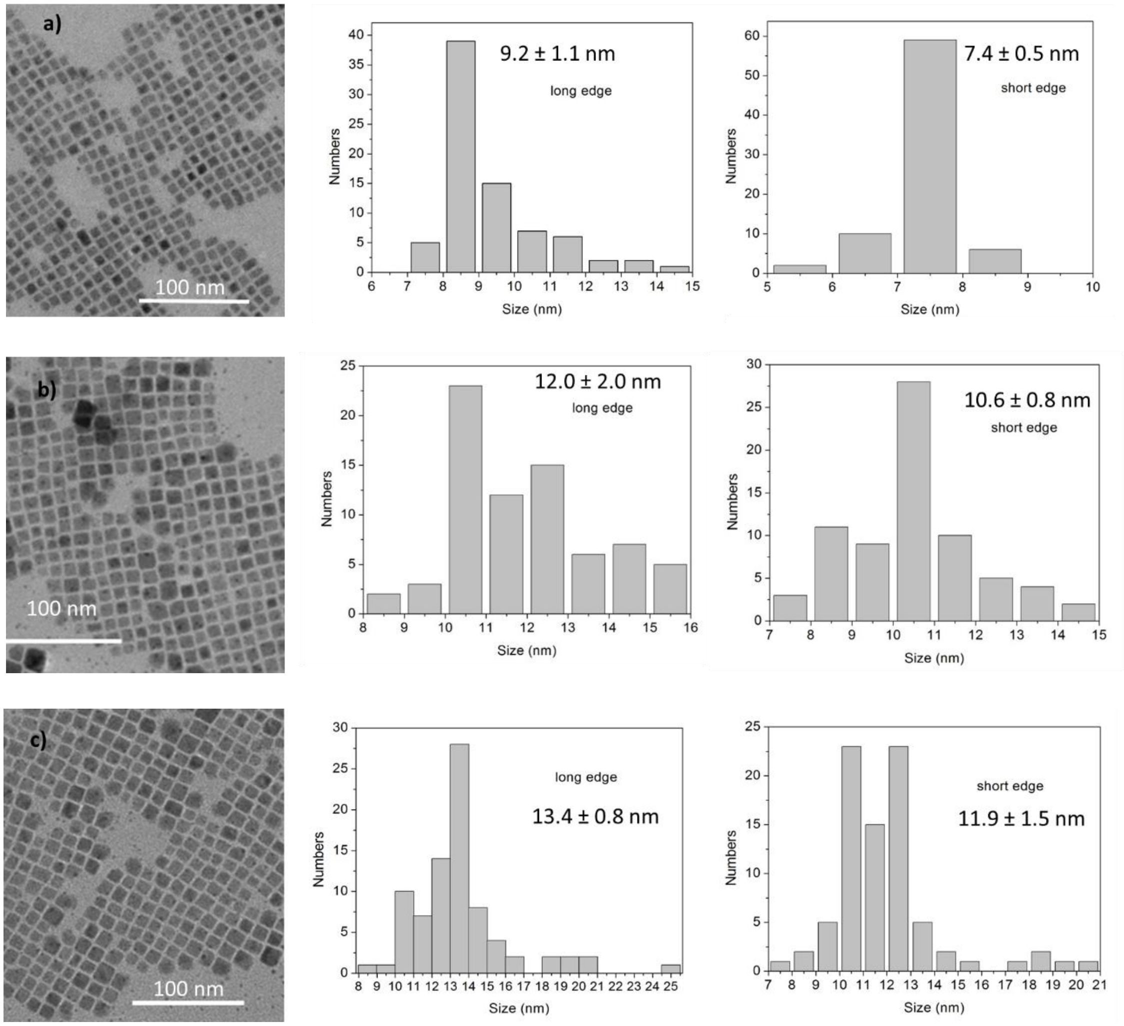

Figure 2.2 TEM images of $CsPbBr_3$ QDs (a), $CsPbBr_{0.75}I_{2.25}$ QDs (b), and $CsPbI_3$ QDs (c) along with corresponding size distribution histograms measured along the long edge and short edge.

QD-RhB and QD-PTZ complexes preparation. We prepared QD-RhB complexes by adding RhB powder into QD solutions in heptane and sonicating for 1 min before filtration to remove the undissolved RhB molecules.[31, 49, 51] Since RhB has negligible solubility in heptane, all dissolved RhB molecules were believed to be attached to the QD surfaces. Therefore, the average number of adsorbed RhB on each QD could be determined by UV-Vis absorption spectroscopy based on the molar extinction coefficients of RhB (116000 M^{-1} cm^{-1} at 555 nm)[52] and QDs (estimated from TA experiments).[31, 49] The number of RhB per QD was assumed to obey a Poisson distribution.[53-54]

To compare the anion dependent hole transfer rates from $CsPbX_3$ QDs to PTZ, the number of adsorbates per QD must be considered. However, different with RhB, PTZ is soluble in heptane so that we cannot determine the average number of adsorbed PTZ molecules per QD by absorbance measurements. According to previous studies,[31, 55-56] measurements of acceptor concentration dependent charge transfer kinetics can help determine the intrinsic charge transfer rates and the number of adsorbates on QD surfaces. Hence, we prepared the QD-PTZ complex solutions by adjusting the PTZ concentration from 0 to 3.2 mM and keeping the concentration of QDs constant. Each solution was sonicated for 3 min to reach an equilibrium between free PTZ molecules in heptane and those bound to the QD surfaces.

2.1.3 Synthesis of $CsPbI_3$ QDs with different sizes in Chapter 5

We synthesized the $CsPbI_3$ QDs according to the published procedure.[7, 46] First, Cs-oleate precursor stock solution was prepared by loading 0.203 g Cs_2CO_3, 0.63 mL oleic acid (OA) and 10 mL octadecene (ODE) into a 25 mL three-neck flask and heating them to 150 ºC under Ar atmosphere until getting clear solution. The precursor solution was kept at 100 ºC to avoid the precipitation of Cs-oleate. In a 100 mL three-neck flask, 0.5 g of PbI_2 and 25 mL ODE were heated at 120 ºC under Ar flow for 30 min. 2.5 mL OA and 2.5 mL oleylamine (OAm) were injected at 120 °C to dissolve the PbI_2. The solution was heated to 175 °C and 2 mL Cs-oleate precursor solution was injected swiftly. After 5 seconds, the reaction was quenched by an ice-water bath. 1:1 volume ratio of methyl acetate was added to the crude solution before centrifuge at 5500 rpm for 10 min. After centrifugation, the QD precipitate was dispersed in heptane for further use. For smaller QD samples, the Cs-oleate precursor injection temperatures were set at 150 °C and 130 °C, respectively, to obtain 10.8 nm and

6.5 nm QDs. Figure 2.3 shows the size distribution histograms of $CsPbI_3$ QDs with average sizes of 11.8 nm, 10.8 nm and 6.5 nm. TEM images can be found in Figure 5.1, Chapter 5.

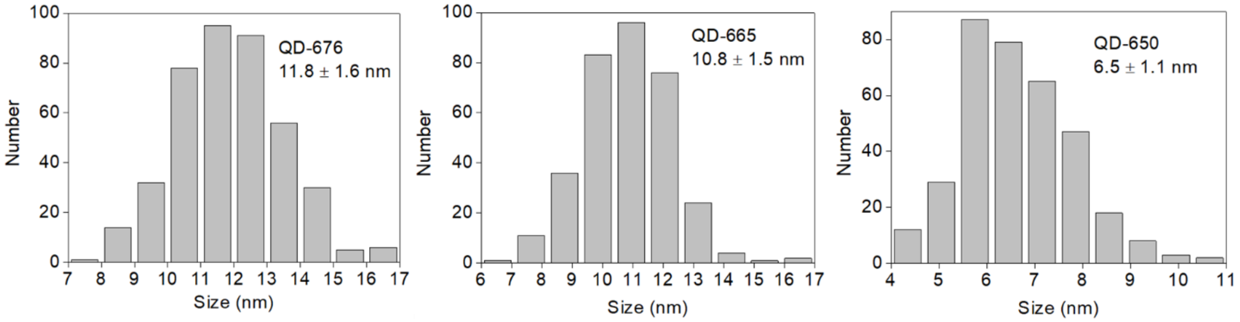

Figure 2.3. Size distribution histograms of $CsPbI_3$ QDs with three different average edge lengths.

2.1.4 Sample preparations in Chapter 6

$CsPbI_3$ QDs synthesis. The QDs synthesis steps are the same as in 2.1.1. TEM image is presented in Figure 6.1, Chapter 6. Figure 2.4 shows the size distribution histograms of $CsPbI_3$ QDs measured along the long edge and short edge with average lengths of 13.4 nm and 11.9 nm, respectively.

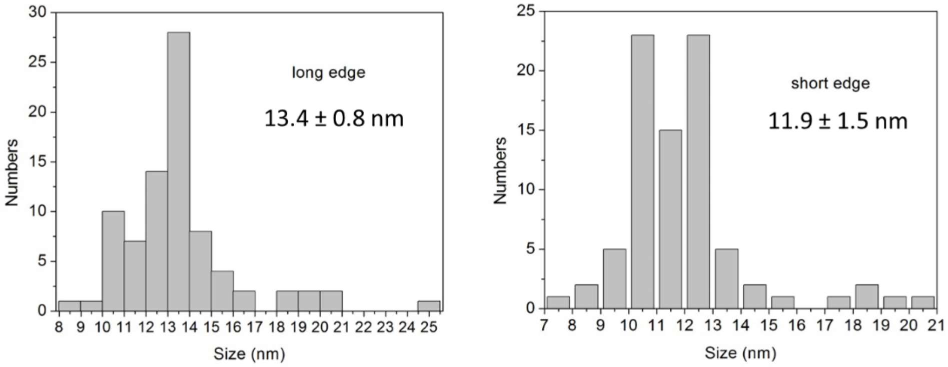

Figure 2.4. Size distribution histograms of $CsPbI_3$ QDs measured along the long edge (left panel) and short edge (right panel).

QD-Metal oxide nanoparticle films preparation. Metal oxide nanoparticle (NP) films were fabricated by doctor blading of the following colloidal solutions onto sapphire windows and annealing at 450°C for 1 h.[25, 57-58] (1) Al_2O_3 (insulator as control experiment) colloidal solution: 5 mL Aluminum oxide colloidal solution (Alfa, NanoArc® 30 % in 1,2-propanediol monomethyl ether acetate, diameter: 30 nm) and 5-10 drops of triton X-100 were mixed and stirred for 12 h. (2) ZnO colloidal solution: 5 mL ZnO NP solution (Alfa, NanoArc® 40 % in 1,2-propanediol monomethyl ether acetate, diameter: 20 nm), 5-10 drops of triton X-100 and 0.5 mL 10% (wt) ethyl cellulose in ethanol were mixed and stirred for 12 h. (3) TiO_2 colloidal solution: Titanium dioxide paste (Dyesol, diameter, 20 nm) dispersed in ethanol. The annealed NP films were immersed in concentrated $CsPbI_3$ QDs solution for 48 h. The films were then removed from the QDs solution, rinsed with heptane and dried in the air. UV-Vis absorption spectra were measured before and after QDs adsorption on the NP films. Figure 2.5 shows the photograph of QD-Metal oxide NP films and the absorption spectra before and after QDs adsorption.

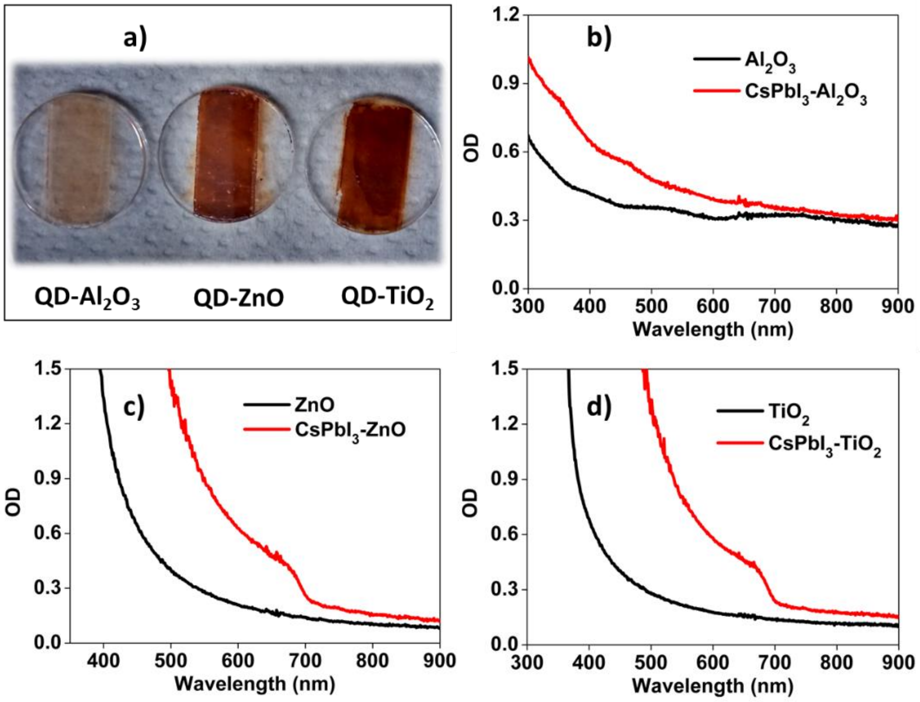

Figure 2.5. (a) Photograph of the $CsPbI_3$ QD-metal oxide nanoparticle films. (b) Absorption spectra of blank Al_2O_3 NP film (black line) and QD-Al_2O_3 NP film (red line). The obvious non-zero OD value of blank Al_2O_3 NP film is due to light reflection and scattering. (c) Absorption spectra of blank ZnO NP film (black line) and QD-ZnO NP film (red line). (d) Absorption spectra of blank TiO_2 NP film (black line) and QD- TiO_2 NP film (red line).

2.1.5 QDs with different post-synthesis treatments in Chapter 7

The procedure of hot-injection synthesis of $CsPbI_3$ QDs are the same as described in 2.1.3. The difference is the post-synthesis purification method. To obtain the original QD sample, the crude solution was centrifuged at 5500 rpm for 15 min to precipitate the aggregated QDs. After centrifugation, the precipitate was dispersed in heptane for further use. To obtain the washed QD sample, methyl acetate (1:1 volume) was added into the crude solution, followed by centrifugation at 5500 rpm for 15 min. The precipitate was dissolved by 1 mL hexane in each centrifuge tube (6 in total). Another 1 mL methyl acetate was added into each tube, followed by centrifugation at 5500 rpm for 10 min. The precipitate was dispersed in heptane for future use. Both the original and washed samples were centrifuged to remove aggregates in solution before use.

2.2. Time-resolved spectroscopy

2.2.1. Visible femtosecond transient absorption setup

The pump-probe transient absorption (TA) experiments were based on a regeneratively amplified Ti:sapphire laser system (Coherent Legend, 800 nm, 150 fs, 2.3 mJ/pulse, and 1 kHz repetition rate). The femtosecond TA measurements were performed with a Helios spectrometer (Ultrafast Systems LLC). 400 nm pump pulses were generated by frequency doubling of the 800 nm pulse at a BBO crystal. 500 nm pump pulses were generated by sum-frequency generation at the BBO crystal using the 1333 nm signal of an optical parametric amplifier (OPA, Opera, Coherent) and the 800 nm laser beam. The power of the pump beam was adjusted by a neutral-density filter. The pump beam was collimated and then focused at the sample with a beam waist from 300 to 400 μm. A white light continuum (WLC) from 420 to 800 nm was generated by focusing ∼10 μJ of the 800 nm pulse into a sapphire window. The WLC was split into probe and reference beams. The probe beam was collimated and then focused with an Al parabolic reflector onto the sample (with a beam waist of 150 μm at the sample). Both the reference and probe beams were sent into a fiber optics-coupled multichannel spectrometer with complementary metal-oxide-semiconductor (CMOS) sensors and detected at a frequency of 1 kHz. The reference beam intensity was used to correct the pulse-to-pulse fluctuation of the white-light continuum. The pump beam was chopped by a chopper synchronized to 500 Hz. The pump induced absorbance change was calculated by comparing the probe intensities of the pumped and unpumped sample. The delay time between the pump and probe pulses was controlled by a motorized delay stage. The instrument response function (IRF) of this system was determined to be ~150 fs by measuring solvent responses under the same experimental conditions (with a higher excitation power). Solution samples were loaded into 1 mm quartz cuvettes and stirred constantly by a magnetic stir bar during the measurements.

2.2.2 Visible nanosecond transient absorption setup

Nanosecond TA experiments were conducted with the EOS spectrometer (Ultrafast Systems LLC). The pump beams were generated in the same way as the femtosecond TA measurements. The white light continuum (380-1700 nm, 0.5 ns pulse width, 20 kHz repetition rate) used here was generated by focusing a Nd:YAG laser into a photonic crystal fiber. The delay time between the pump and probe beam was controlled by a digital delay generator (CNT-90, Pendulum Instruments). The probe and reference beams were detected with the same multichannel spectrometers used in the femtosecond TA experiments. To connect spectra and kinetics from femtosecond and nanosecond TA measurements, we scaled the amplitudes of the nanosecond data by a factor to overlap with the femtosecond data in the delay time from 0.7 to 1.2 ns.

2.2.3. Static PL and Time-resolved PL decay measurements

Steady-state emission spectra were measured with a FluoroMax-3 Spectrofluorometer of HORIBA Scientific. 1 cm quartz cuvette was used as solution holder and placed at a right-angle geometry. Time-correlated single photon counting (TCSPC) technique was adopted to measure the PL decay kinetics. The excitation pulses at 400 nm (or 490 nm) were generated by frequency-doubling of the output pulses centered at 800 nm (or 980nm) (~100 fs, 80 MHz) from a mode-locked Ti:Sapphire laser (Tsunami oscillator pumped by a 10 W Millennia Pro, Spectra-Physics) through a BBO crystal. The emitted photons from QDs were detected by a microchannel-plate photomultiplier tube (Hamamatsu R3809U-51), whose output was amplified and analyzed by a TCSPC board (Becker & Hickel SPC 600). The IRF of this system was determined to be ~700 ps when the time window is 1000 ns, ~200 ps when the time window is 50 ns.

Chapter 3. Effect of residual PbI_2 in $CsPbI_3$ QDs

3.1. Introduction

This chapter is about our work on the hot carrier trapping in $CsPbI_3$ QDs by UV-Vis spectroscopy, photoluminescence excitation (PLE) spectroscopy and pump-probe transient absorption (TA) spectroscopy. Although the results finally prove the inexistence of hot carrier trapping, there are still two points worth mentioning in this dissertation. First is that the size distribution of QDs will influence the PLE spectra. The second point is that PbI_2 absorbs light with wavelengths shorter than 420 nm, thus influencing the PLE spectra significantly in the UV range and TA spectra and kinetics when pump wavelength is 400 nm. Because of the second point, we always use 500 nm excitation instead of 400 nm in the following study on $CsPbI_3$ QDs to avoid the influence from PbI_2.

3.2. The influence of QDs size distribution on PLE spectra

3.2.1. PLE measurement without considering the size distribution of QDs

To see the hot carrier trapping effect in $CsPbX_3$ perovskite nanocrystals, we measured the photoluminescence excitation spectra of CdSe and $CsPbX_3$ quantum dots solutions to compare with the corresponding absorptance spectra. The absorptance (Abpt) spectra of samples were transformed from the UV-Vis absorption (Abs) spectra. Because $\mathrm{Abs} = -\lg(1 - \mathrm{Abpt})$, $\mathrm{Abpt} = 1 - 10^{-Abs}$. The absorptance spectra showed the proportion of absorbed light at each wavelength. The PLE spectra were measured by exciting the QDs solution using 360-800 nm wavelength with a step of 1 nm and monitoring the photoluminescence emission intensity at a fixed wavelength around the PL spectra peak. Figure 3.1 presents the comparison of PLE spectra and absorptance spectra of the corresponding quantum dots solutions. The PLE spectra were scaled to match the absorptance spectra around the band edge absorption wavelengths. From the comparison between absorptance and PLE spectra, we can see for the CdSe QDs solution, the Abpt and PLE spectra are matched well, which means quantum yields of the CdSe QDs by different wavelengths excitation are quite close. When quantum dots absorb more light at certain wavelengths, the emission of fluorescence excited by the corresponding wavelengths increases proportionally. No extra excited hot charge carrier was trapped when excited by higher energy photons. Similarly, we concluded that in $CsPbBr_3$ perovskite nanocrystals, no hot carrier trapping effect existed. However, for $CsPb(Br/I)_3$ and $CsPbI_3$ QDs samples, an obvious gap between Abpt and PLE appeared at short wavelength parts. This might indicate the existence of hot carrier trapping in these samples: When short wavelength photons excited these nanocrystals, part of excited hot carriers did not relax to the band edge, which reduced the electron-hole pair recombination at the band edge, thus reducing PL emission.

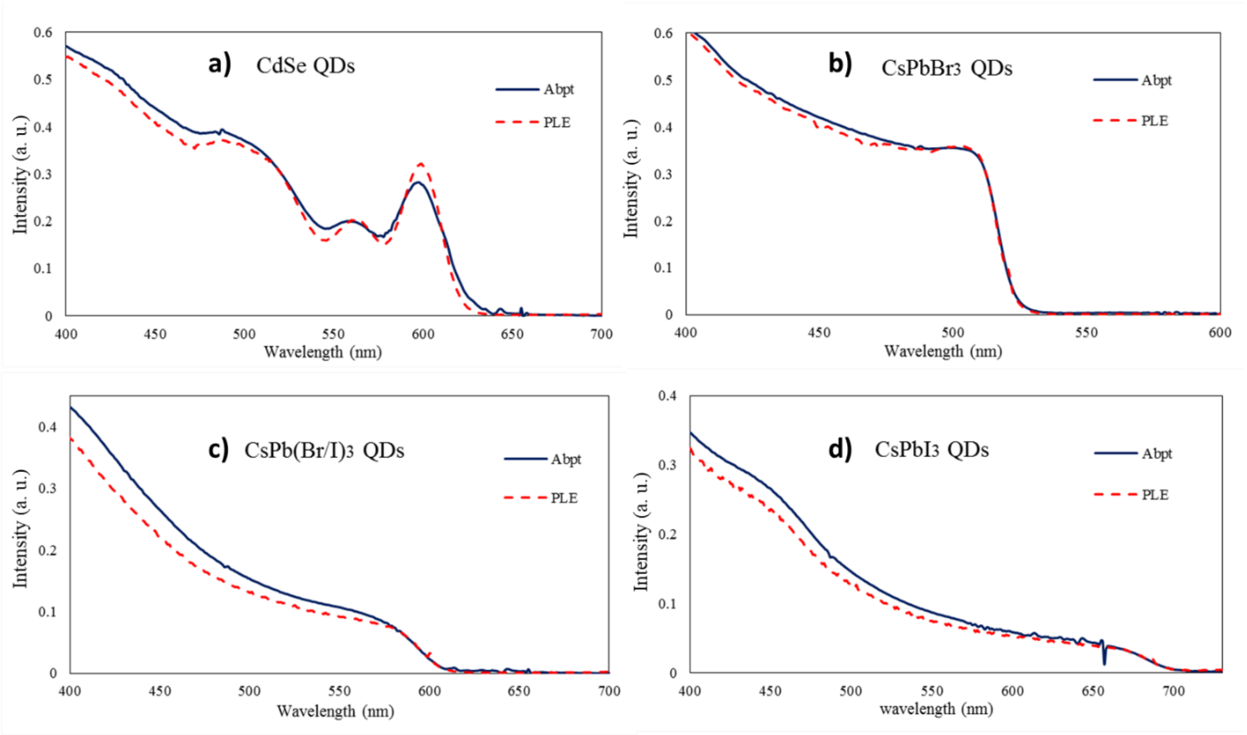

Figure 3.1. Abpt and scaled PLE spectra. a) absorptance spectrum (solid line) and PLE spectrum (dashed line) of CdSe QDs solution. b), c), d) are absorptance spectra (solid line) and PLE spectra (dashed line) of $CsPbBr_3$, $CsPb(Br/I)_3$, $CsPbI_3$ QDs solutions, respectively.

3.2.2. PLE measurement considering the size distribution of QDs

In 3.2.1, when measuring the PLE spectra, photons with a single emission wavelength were detected and both the shorter and longer parts are neglected. However, QDs samples always have a size distribution with smaller size QDs emitting shorter wavelength and larger size QDs emitting longer wavelength photons. When measuring UV-Vis absorption spectra, all the quantum dots were detected while in the PLE measurements the size distribution was not considered. That is why in Figure 3.1a the peaks in Abpt spectrum of CdSe QDs are obviously broader than peaks in PLE spectrum. To solve this problem, we selected 5 wavelengths covering the main PL emission peak of each sample to measure 5 PLE spectra to obtain an averaged PLE spectrum for each sample. The results are shown in Figure 3.2. Obviously, the Abpt and PLE match better than that in Figure 3.1. The gaps between Abpt and PLE spectra in both $CsPb(Br/I)_3$ and $CsPbI_3$ QDs disappear, which means that we cannot see the hot carrier trapping effect.

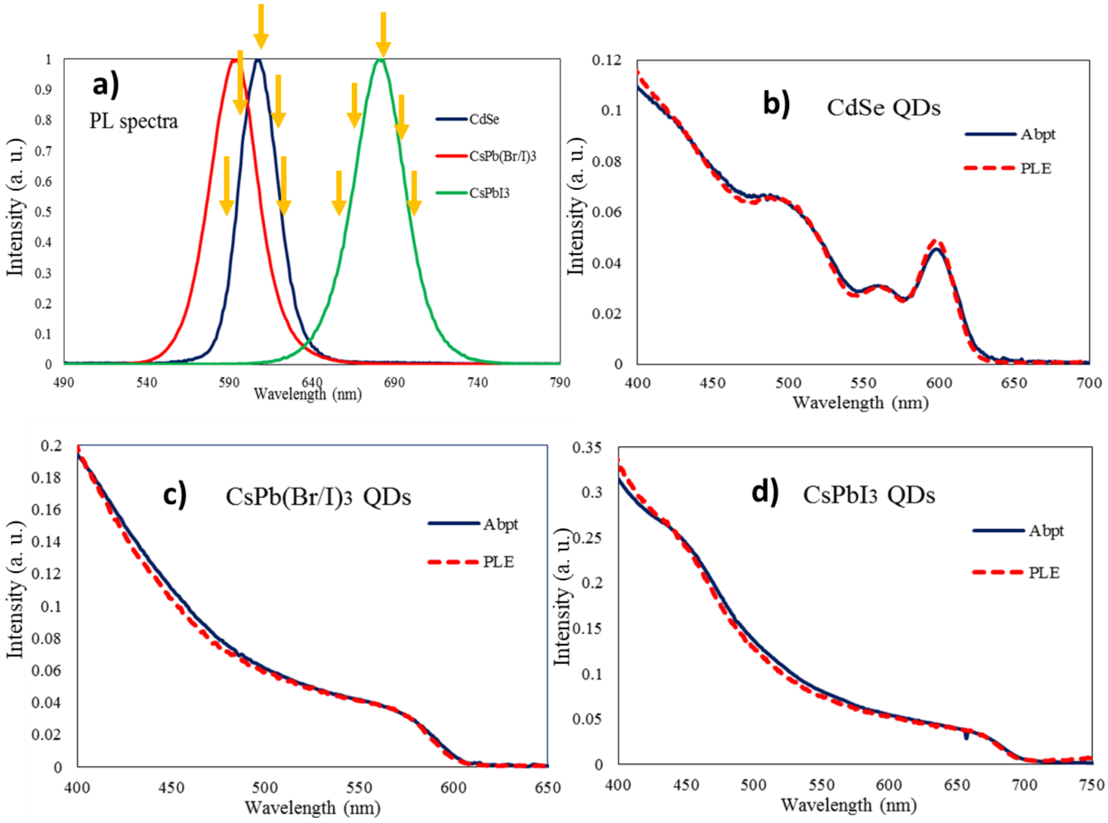

Figure 3.2. Abpt and PLE comparison after considering size distribution of QDs. a) Normalized PL spectra of CdSe, $CsPb(Br/I)_3$ and $CsPbI_3$ QDs. The arrows point to the five emission wavelengths at which we measured PLE. b), c), d) are absorptance spectra (solid line) and scaled average PLE spectra (dashed line) of CdSe, $CsPb(Br/I)_3$, $CsPbI_3$ QDs solutions, respectively.

3.3. Influence of PbI_2 in $CsPbI_3$ QDs

Although QDs size distribution explained the gap between PLE and Abpt spectra of $CsPbI_3$ QDs above the wavelength 400 nm, we noticed that in the UV wavelength, the Abpt spectra are still above PLE, indicating additional absorption species other than QDs. Among the precursors of QDs, only PbI_2 has visible vivid yellow color. We thus suspected that residual PbI_2 may absorbed some UV and visible light and investigated how additional PbI_2 may influence the spectroscopic properties of $CsPbI_3$ QDs by adding PbI_2 into the QD solution.

We measured the UV-Vis absorption spectra and TA spectra of $CsPbI_3$ QDs, PbI_2 solution and their mixture. Figure 3.3 shows the results. During the QDs synthesis, the PbI_2 was dissolved in the mixture of oleic acid, oleylamine and ODE. We took out some precursor solution for optical studies. PbI_2 precursor solution has significant absorption at 400 nm as shown in Figure 3.3a. After adding some PbI_2 precursor solution into the $CsPbI_3$ samples, the UV-Vis absorption of the mixture is the sum of two components.

As to the TA study, the main features of TA spectra of $CsPbI_3$ QDs are: 1) exciton bleach (XB) signal due to the band edge state filling; 2) photoinduced absorption (PA) of the excited carriers. See Figure 3.3b. The TA kinetics of the original $CsPbI_3$ nanocrystals and the $CsPbI_3$ QDs + PbI_2 mixture are compared in Figure 3.3c and d. With PbI_2 addition, the decay kinetics of exciton bleach (XB) and photoinduced absorption (PA) significantly accelerate, which conforms to the assumption that the unreacted PbI_2 may influence the TA kinetics of $CsPbI_3$ QDs at 400 nm pump. The TA measurement was also conducted for PbI_2 precursor solution, whose results have been presented in graph e) and f) in Figure 3.3. PbI_2 solution has broad PA signal over the visible spectrum at the time range before ~100 ps. To avoid its influence on the TA spectroscopy of $CsPbI_3$ QDs, we used 500 nm pump wavelength instead of 400 nm in the future studies.

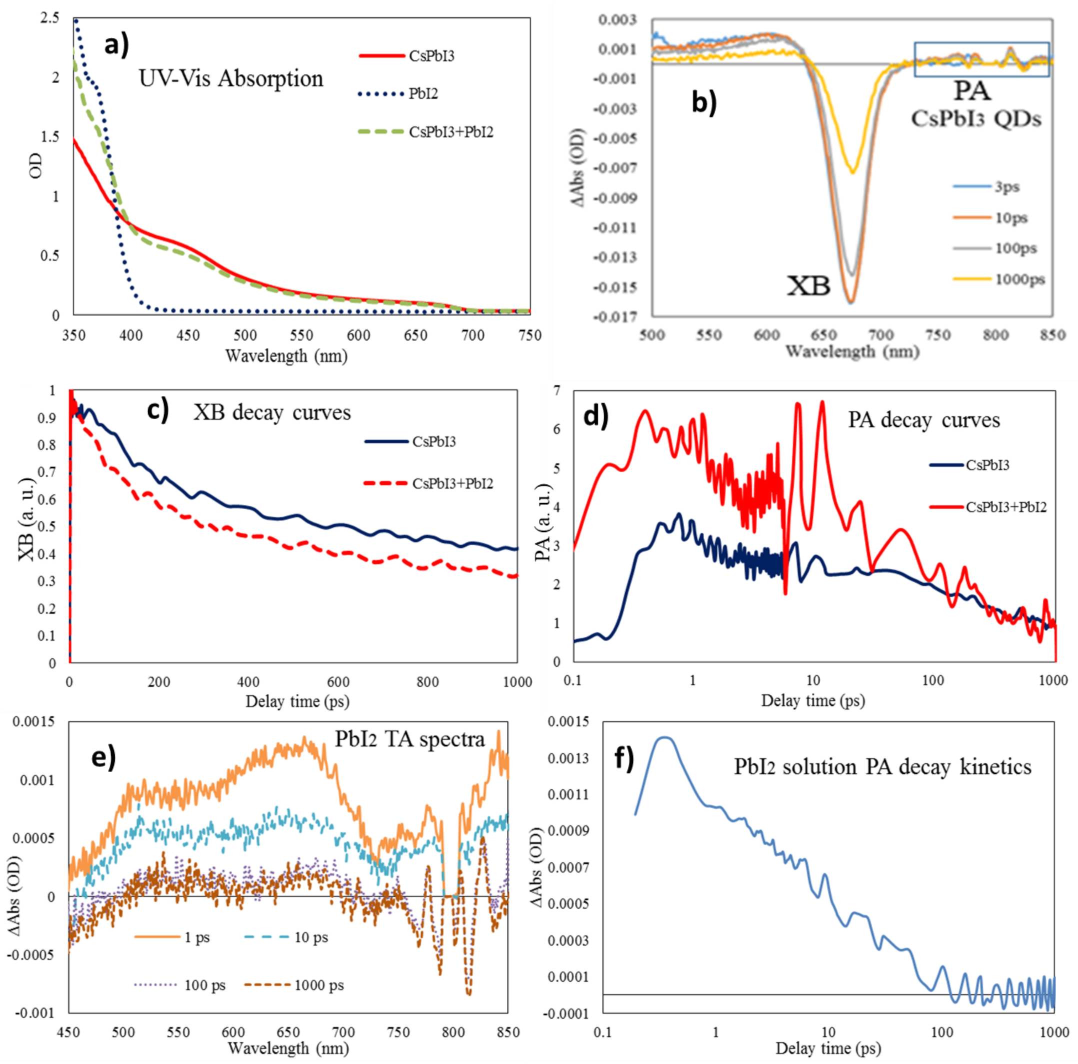

Figure 3.3. UV-Vis absorption and TA study on $CsPbI_3$ QDs, PbI_2 and their mixture. a) UV-Vis spectra of $CsPbI_3$ QDs, PbI_2 and the mixture. b) TA spectra of $CsPbI_3$ QDs pumped by 400 nm femtosecond laser pulses at indicated delay time. XB: exciton bleach signal; PA: photoinduced absorption signal. c) and d) Normalized XB kinetics (c) and PA kinetics (d) of $CsPbI_3$ QDs and QDs + PbI_2 mixture. e) TA spectra of PbI_2 precursor solution pumped by 400 nm laser pulses at indicated delay time. f) The decay kinetics of PA signal in PbI_2 solution.

3.4. Conclusion

In summary, this chapter records two lessons we learned from our work on the fictional hot carrier trapping in $CsPbI_3$ QDs. First, when we measure PLE spectra, the broadening of PL spectra by the size distribution of QDs need to be considered. Secondly, the residual PbI_2 will influence the spectroscopic characteristics of $CsPbI_3$ QDs when the excitation wavelength is 400 nm or shorter because PbI_2 absorbs light at the wavelength range shorter than 420 nm. Starting from next chapter, we focus on studying charge transfer involving $CsPbI_3$ QDs.

Chapter 4. Anion composition dependent charge transfer in $CsPbI_3$ QDs

4.1. Introduction

We reported ultrafast interfacial charge transfer from $CsPbBr_3$ QDs to electron and hole acceptors in 2015.[31] Noticeably, the anion composition of these perovskite QDs could be easily controlled by synthesis or post-synthetic ion exchange reactions,[19-20] thus tuning the band gap to cover the whole visible spectrum. To gain further insight into the electronic properties of $CsPbX_3$ QDs, we asked the question that how the anion compositions will influence the charge carrier behavior, interfacial charge transfer rates specifically. We have found Rhodamine B (RhB) molecules as electron acceptors adsorbed on the perovskite QDs can selectively remove the electron from the excited QDs,[31, 49, 51] and phenothiazine (PTZ) molecules as hole acceptors can extract hole from the excited QDs effectively.[31, 54, 56] These two facts lay the foundation for us to investigate the anion dependent charge transfer processes in solution phase. Starting with excited QD-RhB or QD-PTZ complexes, the charge carrier migration can be expressed as following equations.

$$\mathrm{CsPb}X_3(\mathrm{e-h})-\mathrm{RhB}\overset{ET}{\rightarrow}\mathrm{CsPb}X_3(\mathrm{h})-\mathrm{RhB(e)}\overset{CR}{\rightarrow}\mathrm{CsPb}X_3-\mathrm{RhB}\quad(4.1)$$

$$\mathrm{CsPb}X_3(\mathrm{e-h})-\mathrm{PTZ}\overset{HT}{\rightarrow}\mathrm{CsPb}X_3(\mathrm{e})-\mathrm{PTZ(h)}\overset{CR}{\rightarrow}\mathrm{CsPb}X_3-\mathrm{PTZ}\quad(4.2)$$

In this chapter, we study the anion composition dependent interfacial charge transfer from $CsPbX_3$ (X = Br, I, or mixed Br/I) perovskite QDs to RhB using transient absorption spectroscopy and anion dependent hole transfer from $CsPbX_3$ QDs to PTZ using time-resolved PL decay measurements (Figure 4.1). Results show that in perovskite QD-RhB complexes, excited electron-hole pair gets separated in short time periods (10s to 1000s picoseconds) and the charge separate states recombine in long time periods (1 to 10 microseconds). The interfacial electron transfer (ET) and charge recombination (CR) rates increase from $CsPbBr_3$ to $CsPbI_3$ QDs. Plus, rates of hole transfer (HT) to

PTZ increase slightly from $CsPbBr_3$ to $CsPbI_3$ QDs. This study clearly reflects the anion dependent charge dynamics of perovskite QDs and provides a valuable reference for the future solar energy conversion applications using perovskite nanocrystals.

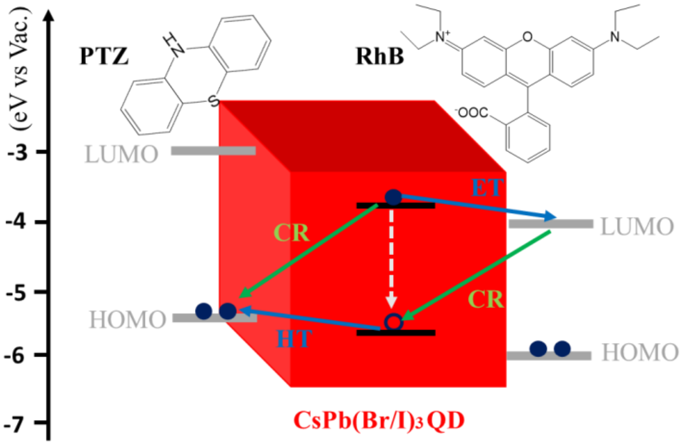

Figure 4.2. Energy level diagram of $CsPbX_3$ QD-RhB and QD-PTZ complexes and possible charge transfer pathways. Black solid lines: CB and VB edges of perovskite QDs. Grey dashed arrow: exciton recombination in QD. ET: electron transfer; HT: hole transfer; CR: charge recombination.

4.2. Results and discussion

4.2.1. Characterization of perovskite QDs

Figure 4.2a and b show the static UV-vis absorption and PL spectra of $CsPbBr_3$, $CsPbBr_{0.75}I_{2.25}$ and $CsPbI_3$ QDs. With changing the anion composition from bromide to iodide, both the absorption onset and emission peak are redshifted significantly due to decreasing of the band gap.[46] PL lifetime elongates from $CsPbBr_3$ to $CsPbI_3$ QDs (Figure 1c), which is consistent with a previous report[59] that attributes the elongation to anion dependent band gap and Kane energy.[60-62] These perovskite QDs have orthorhombic (quasi square) shapes under TEM (see Chapter 2), which is also consistent with previous observations.[19-20, 46] Based on the QD sizes we observed and band edge positions of corresponding bulk perovskites,[8, 63-66] we calculated the anion dependent band positions of 1S excitonic states as shown in Figure 4.2d. From the results we can see the valence band (VB) maximum energy shifts remarkably from $CsPbBr_3$ (-5.85 eV vs Vac.) to $CsPbI_3$ QDs (-5.36 eV vs Vac.) while the conduction band (CB) minimal energy shift is much less. These trends are consistent with reported band edge positions measured by experimental methods.

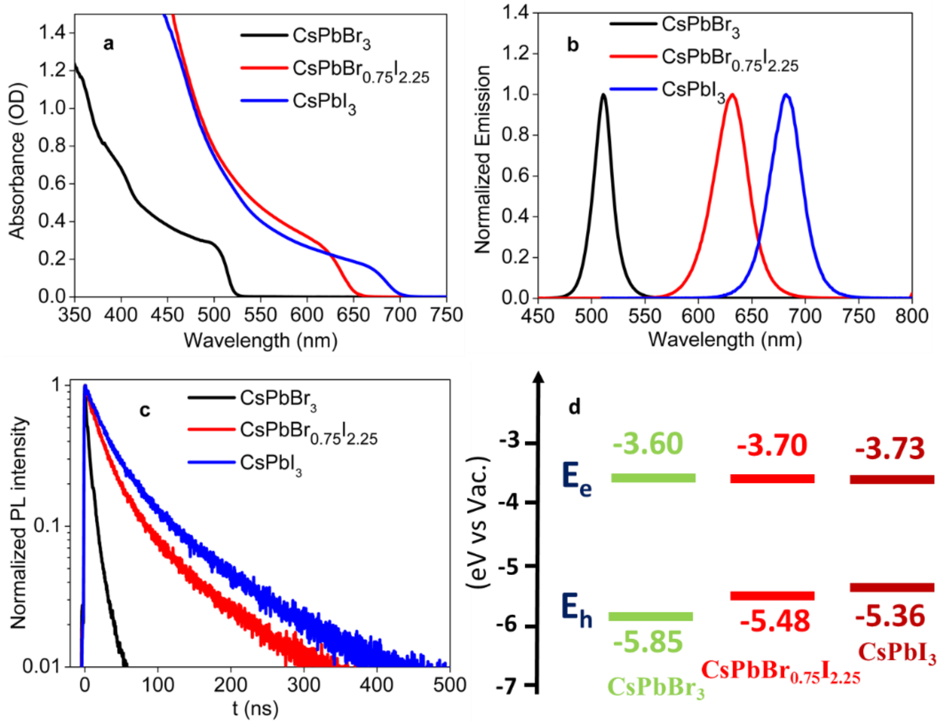

Figure 4.2. (a) UV-Vis absorption, (b) normalized PL spectra and (c) normalized PL decay curves of $CsPbBr_3$ QDs, mixed anion perovskite QDs and $CsPbI_3$ QDs in heptane. (d) Calculated band edge positions of $CsPbBr_3$ QDs, $CsPbBr_{0.75}I_{2.25}$ QDs and $CsPbI_3$ QDs.

4.2.2. Electron transfer and charge recombination kinetics in $CsPbBr_3$ QDs

Before measuring TA spectra, we characterize the $CsPbBr_3$ QDs and QD-RhB complexes with UV-Vis absorption. As shown in Figure 4.3a, the absorption of QD-RhB complexes has negligible difference from free QDs at the region from 350 to 520 nm, which means the energetics of QDs have no significant change after RhB attached on the QD surfaces. Additionally, the zoomed in spectra (Inset in Figure 4.3a) from 520 nm to 610 nm confirm the existence of RhB on QD surfaces with an evident ground state absorption peak around 555 nm. From the optical density of RhB molecules and QDs, the average RhB/QD ratio is estimated to be 5.7.

The TA spectra of free $CsPbBr_3$ QDs and QD-RhB complexes are plotted in Figure 4.3b and 4.3c, respectively. In free QDs TA spectra, the main feature is the state-filling-induced exciton bleach (XB) signal (with a peak around 508 nm and initial amplitude ~7 mOD) formed within 1 ps because of hot carrier relaxation. Following the formation, the XB signal decays gradually because of exciton recombination. The kinetics curve of free QDs XB is plotted in Figure 4.3d (green line) and the decay can be fit by a bi-exponential function (black line). Different from free QDs, another bleach signal appears in the TA spectra of QD-RhB complexes. The signal, mainly located from 535 to 580 nm (Figure 4.3c inset), is attributed to the ground state bleach of the RhB due to electron transfer from $CsPbBr_3$ QD to the LUMO of RhB (Figure 4.1). Through plotting the kinetics of XB and RhB signal (with subtraction of the photo-induced absorption (PA) signal),[31] we can clearly see the formation process of RhB ground state bleach (red dots in Figure 4.3d). Compared to the free QDs XB kinetics, the XB decay rates of QD-RhB (blue dots in Figure 4.3d) significantly increase due to electron transfer process which is faster than the exciton recombination. Furthermore, the RhB signal kinetics curve can be scaled to match the XB recovery at the later time stage from 30 ns to 10 μs (Figure 4.3d) when charge recombination process happens. Through multi-exponential fitting, the growth of RhB bleach signal and the decay of XB signal can be fit by the same rate constants (Table A.4.2), which further confirms the ET and CR processes. From above analysis, we can also find the hole contribution to XB in $CsPbBr_3$ QDs is around 35%, with only a little deviation from our previous reported value (32.8%)[31] due to sample variations.

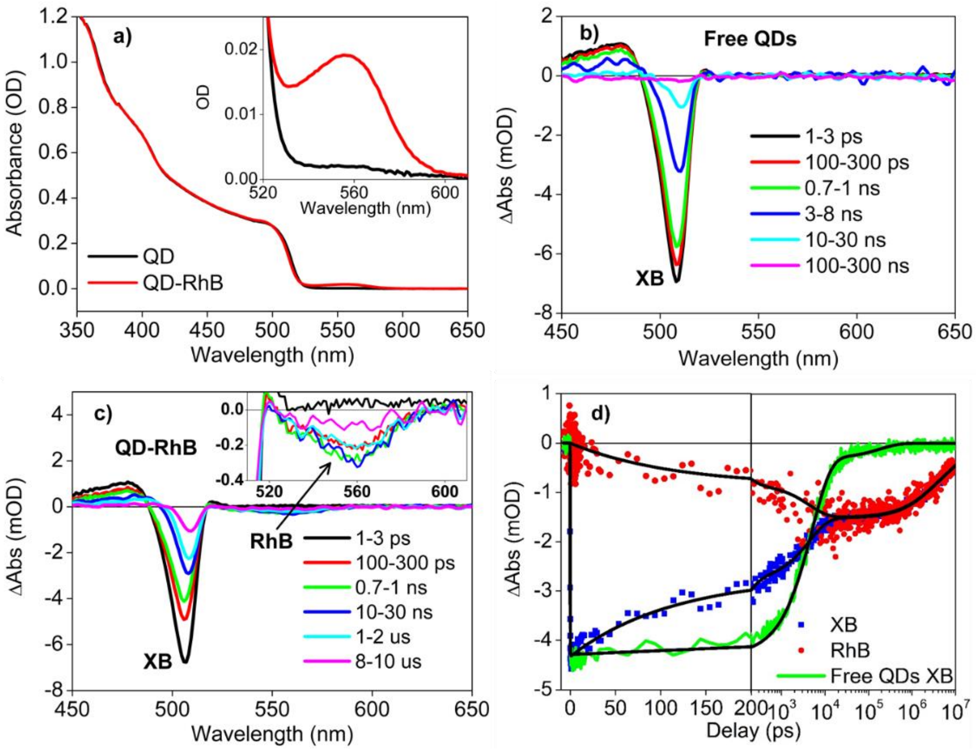

Figure 4.3. (a) UV-Vis absorption spectra of $CsPbBr_3$ QDs without (black line) and with (red line) RhB molecules attached on surfaces. Inset: absorption spectra zoomed in from 520 to 610 nm, showing the static absorption of RhB on QDs with a peak around 555 nm. (b) TA spectra of free $CsPbBr_3$ perovskite QDs measured with 400 nm excitation at indicated delay time from 1 ps to 300 ns. Exciton bleach (XB) feature is labeled. (c) TA spectra of $CsPbBr_3$ QD-RhB complexes measured with 400 nm excitation at indicated delay time from 1 ps to 10 us. Exciton bleach (XB) and the reduced RhB features are labeled. Inset shows the enlarged RhB ground state bleach signal at indicated delay time. (d) XB recovery kinetics of free $CsPbBr_3$ QDs (green line), XB recovery kinetics of $CsPbBr_3$ QD-RhB complexes (blue square dots) and RhB ground state bleach signal formation and decay

kinetics (red round dots). The RhB signal kinetics curve is scaled to match the XB recovery at the charge recombination stage. Black solid lines are multi-exponential fits.

To extract the intrinsic ET and CR rates from the XB recovery kinetics, we derived a fitting function considering the Poisson distribution of RhB molecules on each QD, the contribution of electron and hole to the XB signal along with the contribution of exciton recombination (grey dashed line in Figure 1) to the XB decay in QD-RhB complexes. Detailed derivation is provided in Appendix 2. The fitting function is:

$$XB(t) = XB(0)\Big\{p \cdot [b \cdot g(t) \cdot e^{-m} EXP(me^{-k_1 t}) + (1-b) \cdot g(t) \cdot e^{-m} EXP(me^{-k_2 t})] + (1-p) \cdot \sum_{i=1}^{2} a_i \sum_{n=0}^{\infty} \frac{m^n e^{-m}}{n!} \cdot [b \cdot \frac{k_{i0}-k_{CR}}{k_{i0}+nk_1-k_{CR}} exp[-(k_{i0}+nk_1)t] + b \cdot \frac{nk_1}{k_{i0}+nk_1-k_{CR}} exp(-k_{CR}t) + (1-b) \cdot \frac{k_{i0}-k_{CR}}{k_{i0}+nk_2-k_{CR}} exp[-(k_{i0}+nk_2)t] + (1-b) \cdot \frac{nk_2}{k_{i0}+nk_2-k_{CR}} exp(-k_{CR}t)]\Big\} \tag{4.3}$$

where XB(0) stands for the initial amplitude of XB signal, $g(t) = \sum_{i=1}^{2} a_i \cdot e^{-k_{i0}t}$ is the XB decay kinetics of free QDs, $f(n) = \frac{m^n e^{-m}}{n!}$ (Poisson distribution) is the fraction of QDs with n RhB molecules attached on each QD, m is the average number of RhB molecules per QD, p is the contribution of electron, k_1 and k_2 are two intrinsic ET rate components, b is the fraction of QD-RhB complexes ET through k_1 rate constant, k_{CR} is the charge recombination rate constant. By considering n from 0 to 14, over 99.9% QDs have been considered. Due to the influence of k_1 and k_2 on the hole contribution part in equation 4.3, the electron contribution to XB was adjusted to be 60% instead of 65% to obtain the best fitting. From fitting results listed in Table 4.1 (plot in Figure A.4.3), we conclude that 50% and the other 50% $CsPbBr_3$ QD-RhB complexes conduct electron transfer by intrinsic ET rates of $1.5 \times 10^{-3}\ ps^{-1}$ and $8.0 \times 10^{-5}\ ps^{-1}$, respectively. The charge recombination rate is $1.3 \times 10^{-7}\ ps^{-1}$.

Table 4.1. Fitting results for $CsPbX_3$ QD-RhB XB recovery kinetics

	$CsPbBr_3$-RhB	$CsPbBr_{0.75}I_{2.25}$-RhB	$CsPbI_3$-RhB
m	5.7	5.0	8.1
n	$0,1,2,3 \ldots 13,14$	$0,1,2,3 \ldots 13,14$	$0,1,2,3 \ldots 17,18$
p	60%	57%	50%
b	0.50	0.48	0.55
$k_1\ (ps^{-1})$	1.5×10^{-3}	5.2×10^{-3}	5.8×10^{-3}
$k_2\ (ps^{-1})$	8.0×10^{-5}	NA	NA
$k_{CR1}\ (ps^{-1})$	1.3×10^{-7}	4.5×10^{-6}	5.0×10^{-6}
$k_{CR2}\ (ps^{-1})$	NA	3.2×10^{-7}	4.5×10^{-7}

4.2.3. Electron transfer and charge recombination kinetics in $CsPbBr_{0.75}I_{2.25}$ and $CsPbI_3$ QDs

To figure out the anion composition dependent ET and CR rates of perovskite QDs, we conducted similar treatments (RhB adsorption) and measurements (UV-Vis absorption and TA) on $CsPbBr_{0.75}I_{2.25}$ and $CsPbI_3$ QDs to determine the ET and CR kinetics. The UV-Vis absorption spectra of these two QD samples without and with RhB adsorption are provided in Figure 4.4. Although the ground state absorption of RhB is overlapped with QDs absorption in these two samples, the RhB absorption can still be numerated through subtraction of free QDs absorption (Insets in Figure 4.4). The average RhB/QD ratios are estimated to be 5.0 and 8.1 for $CsPbBr_{0.75}I_{2.25}$ -RhB and $CsPbI_3$-RhB complexes, respectively (Table 4.1).

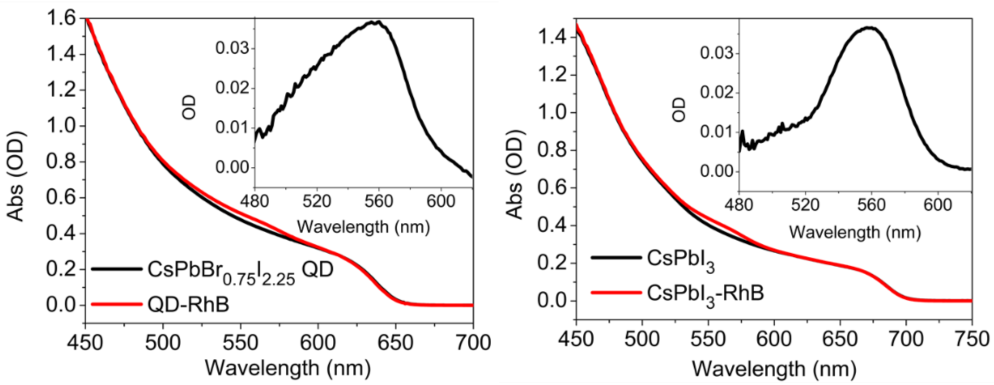

Figure 4.4. UV-Vis absorption spectra of $CsPbBr_{0.75}I_{2.25}$ (left panel) and $CsPbI_3$ QDs (right panel) with and without RhB in heptane. Inset: The absorption spectra of RhB on QD surfaces by subtracting the free QDs absorption from the QD-RhB complexes absorption.

The TA spectra of $CsPbBr_{0.75}I_{2.25}$ QDs and $CsPbI_3$ QDs without and with RhB adsorption are shown in Figure 4.5a and b, where the upper panels are TA spectra of free QDs and the lower panels are those of QD-RhB complexes. These spectra were measured with 500 nm excitation to avoid the absorption of PbI_2 residual in the samples, which may induce additional TA signal.[67] The $CsPbBr_{0.75}I_{2.25}$ QDs sample displays an XB peak around 629 nm and the $CsPbI_3$ QDs presents an XB peak at 676 nm, consistent with the redshift of absorption and emission spectra. Although the RhB ground state bleach signal overlaps with the positive exciton absorption from 520 to 590 nm, the exciton absorption can be subtracted due to its same kinetics with XB. The normalized kinetics curves are plotted in Figure 4.5c and d, from which we validate the existence of ET and CR processes in $CsPbBr_{0.75}I_{2.25}$ -RhB and $CsPbI_3$-RhB complexes. Again, through multi-exponential fitting, we estimate the hole contributions to XB are 40.0% and 48.4% in $CsPbBr_{0.75}I_{2.25}$ QDs and $CsPbI_3$ QDs, respectively (Table A.4.2).

To extract intrinsic ET and CR rates from the XB recovery kinetics, we used following function to fit the XB kinetics:

$$XB(t) = XB(0)\Big\{p \cdot [g(t) \cdot e^{-m} EXP(me^{-k_1 t})] + (1-p) \cdot \textstyle\sum_{i=1}^{2} a_i \sum_{n=0}^{\infty} \frac{m^n e^{-m}}{n!} \cdot$$

$$[\,b \frac{k_{i0}-k_{CR1}}{k_{i0}+nk_1-k_{CR1}} exp[-(k_{i0}+nk_1)t] + b \frac{nk_1}{k_{i0}+nk_1-k_{CR1}} exp(-k_{CR1}t) \;\; + (1 -$$

$$b)\ \frac{k_{i0}-k_{CR2}}{k_{i0}+nk_1-k_{CR2}} exp[-(k_{i0}+nk_1)t] + (1-b) \frac{nk_1}{k_{i0}+nk_1-k_{CR2}} exp(-k_{CR2}t)]\Big\} \qquad (4.4)$$

Here, different from the $CsPbBr_3$-RhB case, only one intrinsic ET rate constant k_1 is enough to obtain good fitting. While for CR processes, two CR rate constants, k_{CR1} and k_{CR2}, are required to fit the experimental kinetics. Therefore, b is the fraction of QD-RhB complexes CR with rate constant k_{CR1}. Fitting results are listed in Table 1 (plotted in Figure A.4.3), from which we conclude that $CsPbBr_{0.75}I_{2.25}$-RhB and $CsPbI_3$-RhB complexes have intrinsic ET rate constants of $5.2 \times 10^{-3}\ ps^{-1}$ and $5.8 \times 10^{-3}\ ps^{-1}$, respectively.

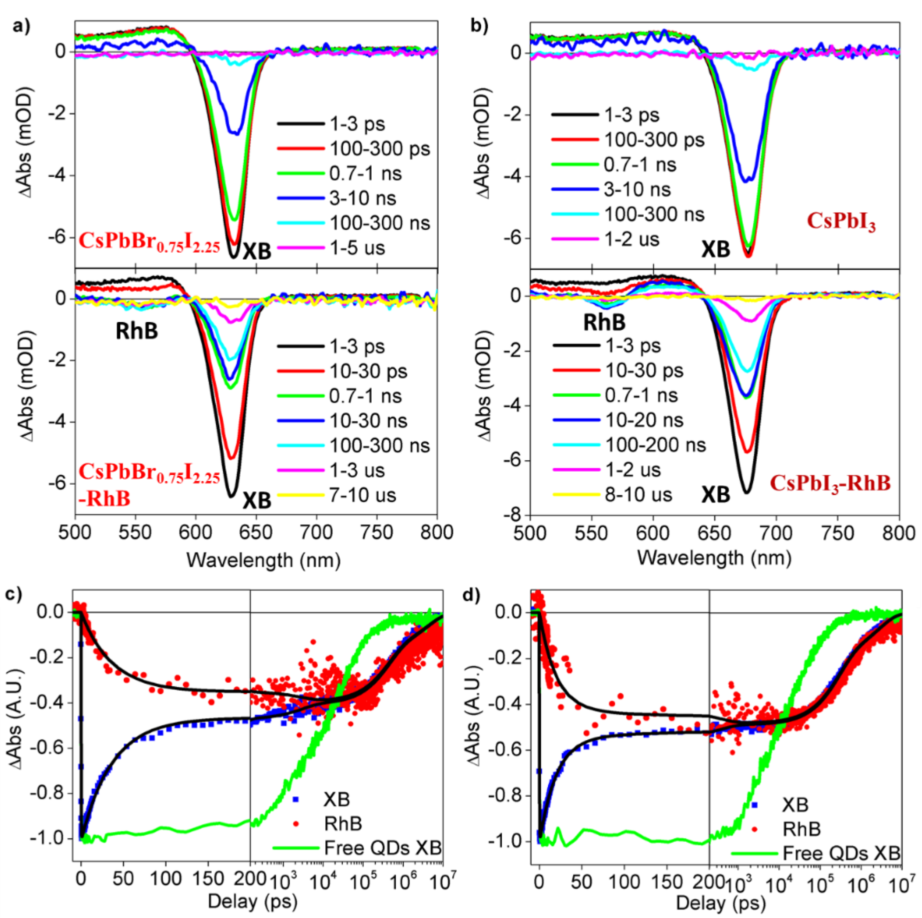

Figure 4.5. (a) TA spectra of CsPbBr$_{0.75}$I$_{2.25}$ QDs and (b) CsPbI$_3$ QDs without (upper) and with RhB (lower) measured with 500 nm excitation at indicated delay time. (c) TA kinetics of free CsPbBr$_{0.75}$I$_{2.25}$ QDs and QD-RhB complexes: XB recovery kinetics of free QDs (green line), XB recovery kinetics of QD-RhB complexes (blue square dots) and RhB ground state bleach signal formation and decay kinetics (red round dots). The RhB signal kinetics is scaled to match the XB recovery at the charge recombination stage. Black solid lines are multi-exponential fits. (d) TA kinetics of free CsPbI$_3$ QDs and QD-RhB complexes with the same denotations in (c).

4.2.4. Hole transfer from CsPbX$_3$ QDs to PTZ

To compare the anion identity dependent hole transfer from perovskite QDs, PTZ concentration dependent PL decay measurements were conducted. Figure 4.6a and b show the experimental results.

The absorption peak at 317 nm increases due to the PTZ concentration increasing, while the concentration of $CsPbBr_3$ QDs is kept constant. With higher total PTZ concentration, more PTZ molecules are adsorbed on the QDs at equilibrium. As shown in Figure 4.6b, the PL decay becomes faster and faster as PTZ concentration increases, which tells that hole transfer rate increases with the increasing of PTZ number on QDs. Unexpectedly, with high PTZ concentrations, some long component PL decay appears (especially in the $CsPbBr_{0.75}I_{2.25}$ samples, Figure A.4.4), which indicates some unknown interactions. Therefore, to extract the intrinsic hole transfer rates from QDs to PTZ, we only consider the cases in which the PTZ concentration is low. Those are the four curves with PTZ concentrations to be 0, 0.053, 0.106, and 0.213 mM.

By assuming that HT rate is proportional to the PTZ/QD ratio and the number of PTZ molecules adsorbed on each QD obeys Poisson distribution, we can calculate the intrinsic HT rate by the following equation,[24, 31]

$$k_1 = -\frac{1}{t_{1/2}} ln[1 - \frac{\ln(2g(t_{1/2})}{m}] \qquad (4.5),$$

where m is the average number of PTZ molecules per QD, $t_{1/2}$ is the half-life of exciton in QD-PTZ complexes and $g(t_{1/2})$ is the percentage of remaining PL amplitude in free QDs at the half-life of QD-PTZ complexes. Through multi-exponential fitting (Figure 4.6b, A.4.4 and Table A.4.4), we can obtain $t_{1/2}$ and $g(t_{1/2})$ for each QD-PTZ PL decay curve (Table A.4.5). To extract m, we normalized the PL decay curves at the tail (Figure 4c). The percentage of remaining PL amplitude at the time when the normalized QD-PTZ PL decay curve matches with the free QD decay (t_{match} in Table A.4.5) is the percentage of free QDs in the solution, which is $f(n) = \frac{m^n e^{-m}}{n!}$ when $n = 0$. Knowing $f(0) = e^{-m}$, we obtain $m = -lnf(0)$. Figure 4.6d shows that with increasing PTZ number per QD, the half-life of PL from QD-PTZ shortens due to faster HT. From above analysis, the intrinsic HT rates from $CsPbBr_3$, $CsPbBr_{0.75}I_{2.25}$ and $CsPbI_3$ to PTZ are determined to be 0.0101 ± 0.0025 ns^{-1}, 0.0127 ± 0.0042 ns^{-1} and 0.0158 ± 0.0045 ns^{-1}, respectively (Table A.4.5).

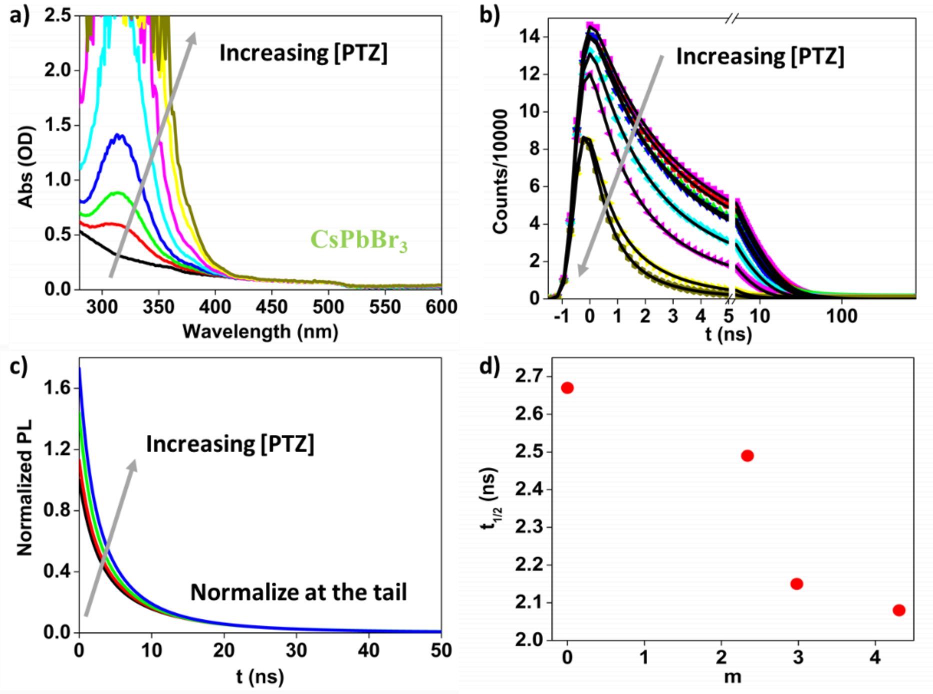

Figure 4.6 (a) UV-Vis absorption spectra of $CsPbBr_3$ QDs with PTZ concentration from 0 to 3.2 mM. The grey arrow indicates the increasing [PTZ]. (b) PL decay curves of solutions in (a), showing that PL decays faster as [PTZ] increases. Black solid lines are multiexponential fittings of each decay curve. (c) Normalization of PL decay curves at the tail to extract the average PTZ/QD ratio. (d) Plot of the half-lives with different PTZ/QD ratios in $CsPbBr_3$ QD-PTZ samples.

Based on above study and analysis, we calculate the average ET, CR and HT time constants in the QD-RhB and QD-PTZ systems. The results are presented in Table 4.2. From $CsPbBr_3$ to $CsPbI_3$ QDs, all the charge transfer time constants become smaller, indicating that $CsPbI_3$ QDs are more favorable for faster charge transfer.

Table 4.2. Average ET and CR time constants in QD-RhB and HT time constant in QD-PTZ systems

QDs	$\tau_{ET}\ (ps)$	$\tau_{CR}\ (ns)$	$\tau_{HT}\ (ns)$
$CsPbBr_3$	12834	7692	99
$CsPbBr_{0.75}I_{2.25}$	192	1732	79
$CsPbI_3$	172	1110	63

4.3. Conclusion

In conclusion, we study the anion dependent charge transfer rates in $CsPbX_3$ QD-RhB and QD-PTZ systems by TA spectroscopy and time-resolved PL decay in this chapter. When the iodide anions are replaced by bromide partially or fully, the ET, CR and HT rates all decrease. The average ET time constants are 172 ps in $CsPbI_3$ QD-RhB, 192 ps in $CsPbBr_{0.75}I_{2.25}$ QD-RhB and 12834 ps in $CsPbBr_3$ QDs. The corresponding CR time constants are 1110 ns, 1732 ns and 7692 ns, respectively. In QD-PTZ systems, the average HT time constants are extracted to be 63 ns ($CsPbI_3$), 79 ns ($CsPbBr_{0.75}I_{2.25}$) and 99 ns ($CsPbBr_3$). These trends of charge transfer rates indicate that $CsPbI_3$ QDs is advantageous in applications that require fast charge separation process, such as photovoltaics and photocatalysis. In next chapter, we are going to explore another factor that may influence the charge transfer rates in $CsPbI_3$ QDs: the size dependent property.

Appendix 1. Kinetics fitting in free $CsPbX_3$ QDs

Exciton bleach (XB) recovery kinetics of free $CsPbX_3$ QDs were fitted with the following equation:

$$XB(t) = A \cdot [\sum_{i=1}^{2} a_i \cdot e^{-t/\tau_i} - e^{-t/\tau_f}] \qquad \text{(A.4.1)},$$

where A is the initial signal amplitude, a_i and τ_i are the amplitude and time constant of multi-exponentials, and τ_f is the signal formation time constant. These fitting parameters are listed in Table A.4.1.

Table A.4.1. Fitting parameters for free $CsPbX_3$ QDs XB recovery kinetics

	τ_f/ps	τ_1/ps (a_1)	τ_2/ps (a_2)
$CsPbBr_3$	0.129	5050.5 (92.7%)	187617.3 (7.3%)
$CsPbBr_{0.75}I_{2.25}$	0.188	2252.3 (43.5%)	67456.8 (56.5%)
$CsPbI_3$	0.324	6293.2 (57.4%)	88324.4 (42.6%)

Appendix 2. Kinetics fitting in QD-RhB complexes

To assign the electron and hole contributions to the XB features in $CsPbX_3$ QDs, we fit the XB kinetics of QD-RhB complexes with the following four-exponential decay function:

$$XB(t) = A \cdot [\sum_{i=1}^{4} a_i \cdot e^{-t/\tau_i} - e^{-t/\tau_f}] \qquad \text{(A.4.2)},$$

where A is the initial signal size, a_i and τ_i are the amplitude and time constant of multi-exponentials, and τ_f is the signal formation time constant. These fitting parameters are listed in Table A.4.2. Meantime, RhB ground state bleach signal kinetics can be fit by the following equation with the same time constants and constrained amplitudes from XB kinetics fitting for each sample (See main text, Figure 4.3d, Figure 4.5c and d):

$$RhB(t) = B \cdot [-\sum_{i=1}^{2} a_i \cdot e^{-t/\tau_i} + \sum_{i=3}^{4} a_i \cdot e^{-t/\tau_i}] \qquad \text{(A.4.3)},$$

where B is the maximum RhB signal size, a_i and τ_i are the amplitude and time constant of multi-exponentials coming from XB kinetics fitting. Therefore, we attribute the first two decay components to be electron transfer process and other two longer decay components to be charge recombination process. The electron contribution to XB feature is $a_1 + a_2$, and hole contribution to XB is $a_3 + a_4$.

Table A.4.2. Fitting parameters for $CsPbX_3$ QD-RhB complexes XB recovery kinetics

		Electron transfer (ET)		Charge recombination (CR)			
	τ_f/ps	τ_1/**ps** (a_1)	τ_2/**ps** (a_2)	τ_3 /**ns** (a_3)	τ_3 /**ns** (a_3)	$\tau_{ET,ave}$ /**ps**	$\tau_{CR,ave}$ /**ns**
$CsPbBr_3$-RhB (XB)	0.16	108.5 (35.5%)	4353 (29.5%)	1930 (12.5%)	12765 (22.5%)	2036	8908
$CsPbBr_3$-RhB (RhB)	-	108.5 (54.6%)	4353 (45.4%)	1930 (35.6%)	12765 (64.4%)		

$CsPbBr_{0.75}I_{2.25}$-RhB (XB)	0.16	36.22 (53.4%)	2965 (6.6%)	420.2 (24.0%)	4296 (16.0%)	358.4	1970
$CsPbBr_{0.75}I_{2.25}$-RhB (XB)	-	36.22 (89.0%)	2965 (11.0%)	420.2 (60.0%)	4296 (40.0%)		
$CsPbI_3$-RhB (XB)	0.20	19.78 (46.2%)	376.4 (5.4%)	278.8 (29.7%)	2788 (18.7%)	57.23	1247
$CsPbI_3$-RhB (RhB)	-	19.78 (89.5%)	376.4 (10.5%)	278.8 (61.4%)	2788 (38.6%)		

To extract intrinsic ET rates from the XB kinetics, we derive a fitting function taking the electron and hole contributions, exciton recombination process and the Poisson distribution of RhB on QD surfaces into consideration. Before that, the population of excited state electron and hole should be derived first.

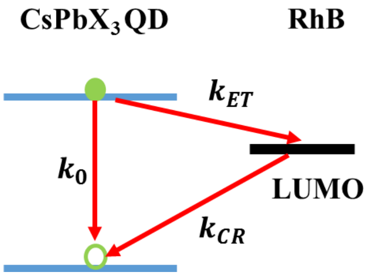

Figure A.4.1. The charge transfer and recombination processes in $CsPbX_3$ QD-RhB complexes.

After excitation, there exist three states in QD-RhB complex: excited state (E), charge transfer state (CT) and ground state (G). The populations of these states can be written as:

$$\frac{d[E]}{dt} = -(k_0 + k_{ET})[E] \qquad \text{(A.4.4)},$$

$$\frac{d[CT]}{dt} = k_{ET}[E] - k_{CR}[CT] \qquad \text{(A.4.5),}$$

$$\frac{d[G]}{dt} = k_0[E] + k_{CR}[CT] \qquad \text{(A.4.6),}$$

where $[E]$, $[CT]$, and $[G]$ are concentrations for the excited state, charge transferred state, and ground state, respectively. k_0 is the rate constant for band edge exciton recombination; k_{ET} is the rate constant for electron transfer from QD to RhB; k_{CR} is the rate constant for charge recombination between transferred electron and hole in the QD. Scheme S1 shows the multiple processes. The solutions to these equations are:

$$[E] = N_0\, exp[-(k_0 + k_{ET})t] \qquad \text{(A.4.7),}$$

$$[CT] = -N_0 \frac{k_{ET}}{k_0 + k_{ET} - k_{CR}} exp[-(k_0 + k_{ET})t] + Bexp(-k_{CR}t) \qquad \text{(A.4.8),}$$

$$[G] = -N_0 \frac{k_0 - k_{CR}}{k_0 + k_{ET} - k_{CR}} exp[-(k_0 + k_{ET})t] - B\, exp(-k_{CR}t) + C \qquad \text{(A.4.9),}$$

where N_0 is the initial concentration of excited state QD-RhB complexes. B and C are undetermined constants. Based on these results, the electron and hole populations can be expressed:

$$[e] = [E] = N_0\, exp[-(k_0 + k_{ET})t] \qquad \text{(A.4.10),}$$

$$[h] = [E] + [CT] = N_0 \frac{k_0 - k_{CR}}{k_0 + k_{ET} - k_{CR}} exp[-(k_0 + k_{ET})t] + B\, exp(-k_{CR}t) \qquad \text{(A.4.11).}$$

When $t = 0,\ [CT] = 0,\ [h] = N_0$, we can get $B = N_0 \frac{k_{ET}}{k_0 + k_{ET} - k_{CR}}$.

$$[h] = N_0 \frac{k_0 - k_{CR}}{k_0 + k_{ET} - k_{CR}} \exp[-(k_0 + k_{ET})t] + N_0 \frac{k_{ET}}{k_0 + k_{ET} - k_{CR}} \exp(-k_{CR}t) \qquad \text{(A.4.12).}$$

Next, we assume the number of RhB molecules per QD obeys Poisson distribution. The fraction of QDs with n RhB molecules on surfaces can be written as:

$$f(n) = \frac{m^n e^{-m}}{n!} \qquad \text{(A.4.13),}$$

where m is the average number of RhB molecules on each QD. Also, we assume the ET rates are proportional to the number of electron acceptors on QD surfaces. That is,

$$k_{ET} = k_n = \mathrm{n}k_1 \qquad \text{(A.4.14)},$$

where k_1 is the intrinsic electron transfer rate, k_{ET}, k_n are total ET rates. Based on these assumption and above derivations, the XB decay kinetics can be expressed as:

$$XB(t) = A \cdot \{p \cdot \sum_{n=0}^{\infty} f(n)\,[e] + q \cdot \sum_{n=0}^{\infty} f(n)\,[h]\} \qquad \text{(A.4.15)},$$

where A is the initial XB signal size, p and q are contributions of electron and hole to the XB feature, respectively. p + q = 1. Plug A.4.10, A.4.12, A.4.13 and A.4.14 into A.4.15,

$$XB(t) = A \cdot \Big\{p \cdot [g(t) \cdot e^{-m} EXP(me^{-k_1 t})] + (1-p) \cdot \sum_{i=1}^{2} a_i \sum_{n=0}^{\infty} \frac{m^n e^{-m}}{n!} \cdot$$

$$[\frac{k_{i0}-k_{CR}}{k_{i0}+nk_1-k_{CR}} \exp[-(k_{i0}+nk_1)t] \ + \frac{nk_1}{k_{i0}+nk_1-k_{CR}} \exp(-k_{CR}t)]\Big\} \qquad \text{(A.4.16)},$$

where $g(t) = \sum_{i=1}^{2} a_i \cdot e^{-k_{i0}t}$ is the bi-exponential decay function of free QDs XB obtained in section A.4.3. We fit the normalized XB kinetics with S16. Results are shown in Figure A.4.3 with parameters listed in Table A.4.3.

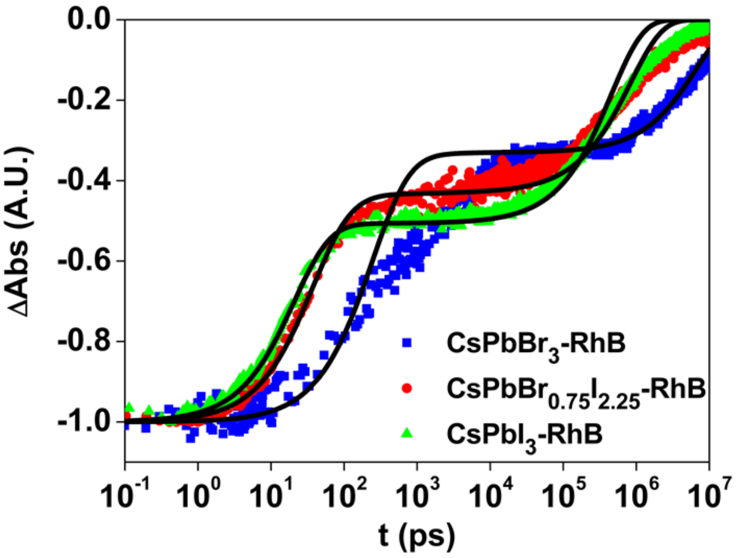

Figure A.4.2. XB recovery kinetics in $CsPbBr_3$-RhB (blue squares), $CsPbBr_{0.75}I_{2.25}$-RhB (red dots), and $CsPbI_3$-RhB (green triangles). Black solid lines are fittings with function A.4.16.

Table A.4.3. Fitting parameters for $CsPbX_3$ QD-RhB XB recovery kinetics with A.4.16

	$CsPbBr_3$-RhB	$CsPbBr_{0.75}I_{2.25}$-RhB	$CsPbI_3$-RhB
m	5.7	5.0	8.1
n	0,1,2,3 … 13,14	0,1,2,3 … 13,14	0,1,2,3 … 17,18
p	65%	57%	50%
$k_1\ (ps^{-1})$	6.8×10^{-4}	5.2×10^{-3}	5.9×10^{-3}
$k_{CR}\ (ps^{-1})$	1.5×10^{-7}	1.2×10^{-6}	2.2×10^{-6}

Obviously in $CsPbBr_3$-RhB (Figure A.4.3 blue squares), the electron transfer (ET) process is not fit well with a slow decay component deviating from the fitting results. While in $CsPbBr_{0.75}I_{2.25}$-RhB (Figure A.4.3 red dots) and $CsPbI_3$-RhB (Figure A.4.3 green triangles), the charge recombination (CR) processes are not fit well with A.4.16. To obtain better fitting, we modify function A.4.16 assuming there exist two batches of QD-RhB complexes in the solution contributing to different ET or CR rates.

For CsPbBr3-RhB, two populations of QD-RhB contribute to two different intrinsic ET rates, k_1 and k_2, respectively. From fitting with A.4.16, we know one k_{CR} rate constant is enough for CsPbBr3-RhB XB kinetics. Then we keep track of the two populations separately with equations A.4.4, A.4.5, A.4.6. The results of band edge electron and hole populations are:

$$[e] = bN_0 \exp[-(k_0 + k_{ET1})t] + (1 - b)\, N_0 \exp[-(k_0 + k_{ET2})t] \qquad \text{(A.4.17),}$$

$$[h] = bN_0 \frac{k_0 - k_{CR}}{k_0 + k_{ET1} - k_{CR}} \exp[-(k_0 + k_{ET1})t] + bN_0 \frac{k_{ET1}}{k_0 + k_{ET1} - k_{CR}} \exp(-k_{CR}t) +$$

$$(1 - b)N_0 \frac{k_0 - k_{CR}}{k_0 + k_{ET2} - k_{CR}} \exp[-(k_0 + k_{ET2})t] + (1 - b)N_0 \frac{k_{ET2}}{k_0 + k_{ET2} - k_{CR}} \exp(-k_{CR}t) \qquad \text{(A.4.18),}$$

where b is the fraction of QD-RhB complexes contributing to the k_{ET1} and $1-b$ is the fraction resulting in k_{ET2}. Still we assume both ET rates are proportional to the number of RhB molecules on QD surfaces. Therefore,

$$k_{ET1} = \mathrm{n}k_1 \qquad \text{(A.4.19)},$$

$$k_{ET2} = \mathrm{n}k_2 \qquad \text{(A.4.20)}.$$

Plug A.4.13, A.4.17, A.4.18, A.4.19 and A.4.20 into A.4.15, the fitting function is as follows (A.4.21).

$$XB(t) = XB(0)\Big\{p \cdot [b \cdot g(t) \cdot e^{-m}EXP(me^{-k_1 t}) + (1-b) \cdot g(t) \cdot e^{-m}EXP(me^{-k_2 t})] + (1-p) \cdot \textstyle\sum_{i=1}^{2} a_i \sum_{n=0}^{\infty} \frac{m^n e^{-m}}{n!} \cdot [b \cdot \frac{k_{i0}-k_{CR}}{k_{i0}+nk_1-k_{CR}} \exp[-(k_{i0}+nk_1)t] + b \cdot \frac{nk_1}{k_{i0}+nk_1-k_{CR}} \exp(-k_{CR}t) + (1-b) \cdot \frac{k_{i0}-k_{CR}}{k_{i0}+nk_2-k_{CR}} \exp[-(k_{i0}+nk_2)t] + (1-b) \cdot \frac{nk_2}{k_{i0}+nk_2-k_{CR}} \exp(-k_{CR}t)]\Big\} \qquad \text{(A.4.21)}.$$

For $CsPbBr_{0.75}I_{2.25}$-RhB and $CsPbI_3$-RhB, two CR rate constants, k_{CR1} and k_{CR2}, are needed for better fitting. Similarly, we keep track of the two populations (with fractions b and 1-b) separately. The electron and hole populations are:

$$[e] = N_0 \exp[-(k_0 + k_{ET})t] \qquad \text{(A.4.22)},$$

$$[h] = bN_0 \frac{k_0 - k_{CR1}}{k_0 + k_{ET} - k_{CR1}} \exp[-(k_0 + k_{ET})t] + bN_0 \frac{k_{ET}}{k_0 + k_{ET} - k_{CR1}} \exp(-k_{CR1}t) + (1-b)N_0 \frac{k_0-k_{CR2}}{k_0+k_{ET}-k_{CR2}} \exp[-(k_0 + k_{ET})t] + (1-b)N_0 \frac{k_{ET}}{k_0+k_{ET}-k_{CR2}} \exp(-k_{CR2}t) \qquad \text{(A.4.23)}.$$

Plug A.4.13, A.4.14, A.4.21 and A.4.22 into A.4.15, the fitting function becomes as follows (A.4.24).

$$XB(t) = XB(0)\Big\{p \cdot [g(t) \cdot e^{-m}EXP(me^{-k_1 t})] + (1-p) \cdot \textstyle\sum_{i=1}^{2} a_i \sum_{n=0}^{\infty} \frac{m^n e^{-m}}{n!} \cdot [b \frac{k_{i0}-k_{CR1}}{k_{i0}+nk_1-k_{CR1}} \exp[-(k_{i0}+nk_1)t] + b \frac{nk_1}{k_{i0}+nk_1-k_{CR1}} \exp(-k_{CR1}t) + (1-b) \frac{k_{i0}-k_{CR2}}{k_{i0}+nk_1-k_{CR2}} \exp[-(k_{i0}+nk_1)t] + (1-b) \frac{nk_1}{k_{i0}+nk_1-k_{CR2}} \exp(-k_{CR2}t)]\Big\} \qquad \text{(A.4.24)}.$$

Then we fit the $CsPbBr_3$-RhB XB kinetics with function A.4.21 and that of $CsPbBr_{0.75}I_{2.25}$-RhB and $CsPbI_3$-RhB with function A.4.24. Fitting results and parameters are presented in Figure A.4.4 and Table 4.1, respectively.

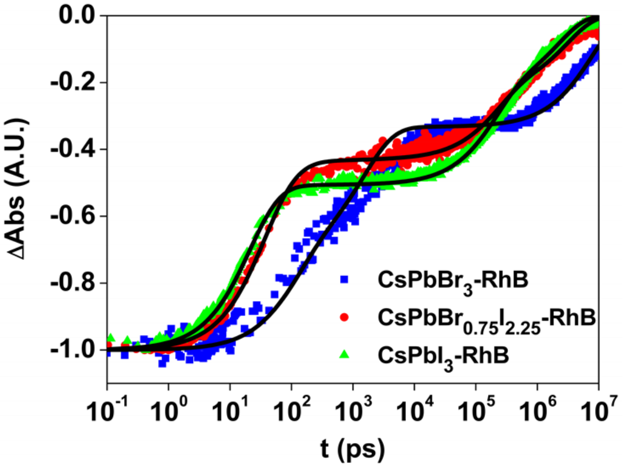

Figure A.4.3. XB recovery kinetics in $CsPbBr_3$-RhB (blue squares), $CsPbBr_{0.75}I_{2.25}$-RhB (red dots), and $CsPbI_3$-RhB (green triangles). Black solid lines are fittings with function A.4.21 (for $CsPbBr_3$-RhB) or A.4.24 (for $CsPbBr_{0.75}I_{2.25}$-RhB and $CsPbI_3$-RhB).

Appendix 3. PL decay kinetics fitting in QD-PTZ complexes

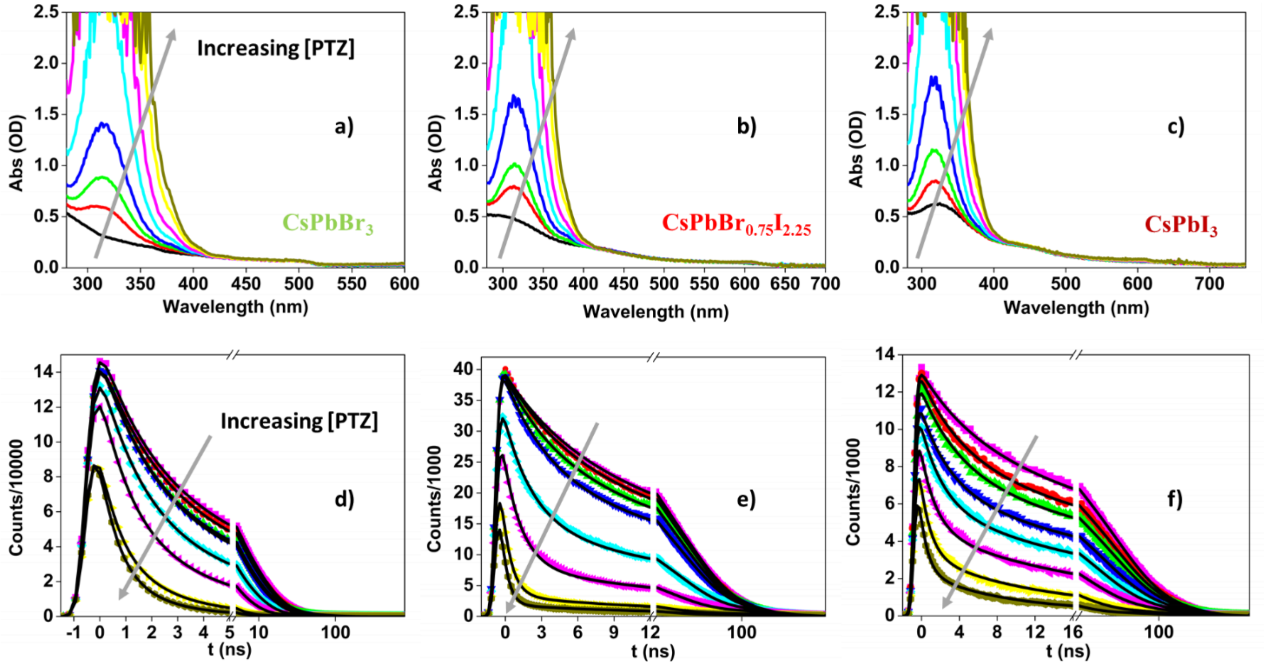

Figure A.4.4. a), b) and c) are UV-Vis absorption spectra of $CsPbX_3$ QDs with increasing PTZ concentration. d), e), and f) are PL decay kinetics of samples in a), b), and c), respectively. Black solid lines are multi-exponential fittings. Arrows indicate the increasing of PTZ concentrations from 0 to 3.2 mM.

From the results shown in Figure A.4.4, we found in high PTZ concentrations, some long components of PL decay appeared (especially in the $CsPbBr_{0.75}I_{2.25}$ samples), which indicated some unknown interactions. Therefore, to extract the intrinsic hole transfer rates from QDs to PTZ, we only consider the cases in which the PTZ concentration is low. Those are the four curves with PTZ concentrations to be 0, 0.053, 0.106, and 0.213 mM. We denote them X-0, X-1, X-2 and X-3 in Table A.4.4 and A.4.5. The increasing decay rates for increasing PTZ concentrations are attributed to the faster hole transfer from QDs to PTZ. Multi-exponential fitting parameters for PL decay curves of the free QDs and 3 lowest [PTZ] are listed in Table A.4.4. Parameters for calculating the HT rates and the extracted intrinsic HT rates are listed in Table A.4.5.

Table A.4.4. Fitting parameters for $CsPbX_3$ QD-PTZ PL decay curves

	a_1	τ_1/ns	a_2	τ_2/ns	a_3	τ_3/ns	a_4	τ_4/ns
Br-0	8.19	1.99	3.98	11.16	5.44	5.70	0.24	66.20
Br-1	6.59	1.61	2.49	13.96	8.38	5.19	0.12	100.0
Br-2	6.89	1.40	2.58	12.33	8.50	4.49	0.12	100.0
Br-3	6.98	1.39	2.49	11.81	8.65	4.35	0.09	100.0
BrI-0	9.61	3.36	22.56	18.41	9.68	65.13	0.76	316.2
BrI-1	11.58	3.32	22.08	18.54	8.91	66.01	0.63	340.6
BrI-2	13.15	3.02	21.05	17.50	8.47	63.49	0.63	354.1
BrI-3	15.88	2.72	19.31	16.26	7.56	62.47	0.79	351.0
I-0	3.02	3.49	6.52	23.85	4.23	78.35	0.24	421.5
I-1	4.08	2.93	5.65	20.93	4.01	73.69	0.28	387.3
I-2	4.35	2.98	5.30	20.45	3.49	73.00	0.22	448.4
I-3	4.42	2.34	4.59	16.06	3.19	62.66	0.24	353.9

Table A.4.5. Hole transfer parameters and rates

	t_{match} (ns)	m	$t_{1/2}$ (ns)	$g(t_{1/2})$	$k_1(ns^{-1})$	Average k_1 (ns^{-1})
Br-1	13.36	2.34	2.49	0.520	0.0067	0.0101 ± 0.0025
Br-2	17.29	2.98	2.15	0.542	0.0128	
Br-3	31.28	4.31	2.08	0.551	0.0110	
BrI-1	10.27	0.70	10.12	0.528	0.0081	0.0127 ± 0.0042
BrI-2	23.09	1.27	8.60	0.566	0.0118	
BrI-3	39.45	1.92	6.66	0.622	0.0182	
I-1	24.27	1.05	11.66	0.570	0.0114	0.0158 ± 0.0045
I-2	37.48	1.45	9.91	0.602	0.0139	
I-3	51.20	1.93	7.20	0.664	0.0221	

Chapter 5. Size dependent charge transfer in $CsPbI_3$ QDs

5.1. Introduction

Cesium lead halide ($CsPbX_3$) perovskite quantum dots(QDs), bridging the bulk lead halide perovskites (LHPs) and inorganic semiconductor nanocrystals, have shown wide applications in thin film solar cells,[7, 12, 68-69] light emitting diodes(LEDs),[70-80] low-threshold lasers,[81-84] luminescent solar concentrators[85] and photocatalysis.[86] Particularly, $CsPbI_3$ QDs, with its broad absorption spectrum covering whole visible range and stability in α phase at room temperature, become a promising candidate for high efficiency thin film solar cells, whose reported power conversion efficiency (PCE) has reached 13.43%.[7, 12] To further improve the optoelectronic device performance, exploring possible tunable parameters of the material is necessary. In addition to composition tunability by adjusting the anion and cations,[19-20, 87] the size of colloidal QDs offers another controllable parameter for maximizing the utility of $CsPbX_3$ perovskite nanomaterials.

Charge separation and recombination are essential processes in QD-based optoelectronic devices.[88-90] In solar cells, for instance, charge separation efficiency and charge recombination loss directly impact their PCE.[91-92] QD size may influence the charge separation (CS) and charge recombination (CR) rates significantly. On the one hand, QDs with different sizes have different conduction band (CB) and valence band (VB) energy levels because of quantum confinement effect, changing the driving force of charge separation (ΔG_{CS}) and charge recombination (ΔG_{CR}).[21-23] On the other hand, the surface electronic densities may vary with QD sizes, thus influencing electronic coupling strength between the electron donor and acceptor for both the charge separation(H_{CS}) and charge recombination (H_{CR}) processes.[24] Both effects, according to Marcus theory, change the charge transfer rates.[24-25] Although the size dependence of CS and CR in traditional cadmium chalcogenide QDs are well known,[24-25, 93] it is unclear whether similar dependence can be expected in perovskite QDs because of significant differences in nanocrystal structures and extents of quantum confinement.[46, 68, 94] Therefore, a quantitative study of size dependent CS and CR in $CsPbI_3$ QDs is critical to understand the possible influences of QD size on perovskite QD optoelectronic devices.

In this chapter, we investigate the size dependence of charge separation and recombination rates in $CsPbI_3$ QD-Rhodamine B (RhB) complexes by ultrafast transient absorption (TA) spectroscopy (see Eq. 5.1 and Scheme 5.1). By decreasing the average QD size from 11.8 nm to 10.8 nm to 6.5 nm, both CS and CR rates increase exponentially. We show that the observed trend can be explained by Marcus theory, using calculated CS and CR driving forces (ΔG_{CS} and ΔG_{CR}), reorganization energy (λ) and electronic coupling strength (H_{CS} and H_{CR}) in these QD-RhB systems.

$$\mathrm{CsPbI_3(e-h)-RhB} \overset{CS}{\rightarrow} \mathrm{CsPbI_3(h)-RhB(e)} \overset{CR}{\rightarrow} \mathrm{CsPbI_3-RhB} \quad (5.1)$$

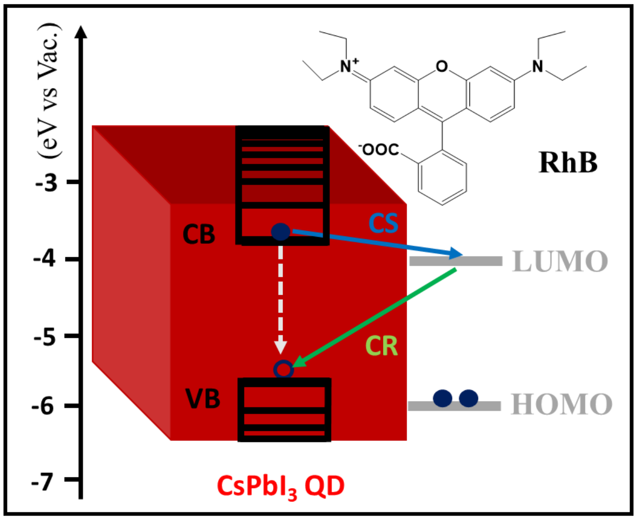

Scheme 5.1. Schematic energy level diagram and charge separation and recombination pathways at the $CsPbI_3$ QD-Rhodamine B Interface: conduction band (CB) and valence band (VB) edges in $CsPbI_3$, charge separation (CS) between QD and RhB (blue arrow), charge recombination (CR) process (green arrow), and electron-hole recombination inside the QD (dashed grey arrow).

5.2. Results and discussion

5.2.1. Sample characterizations

$CsPbI_3$ QDs of three different average sizes were synthesized according to published hot injection methods (see Chapter 2 for details).[7, 46] These QDs were purified and dispersed in heptane for the measurements discussed below, unless specified. Their TEM images (Figure 5.1d, e, and f) show that these QDs are in cubic crystal phase and exhibit orthorhombic shapes with average edge lengths of 11.8±1.6 nm, 10.8±1.5 nm and 6.5±1.1 nm, consistent with previous reports.[7, 46] The UV-Vis absorption and photoluminescence (PL) spectra of these QDs (Figure 5.1a, b, c) show that with decreasing sizes, the first exciton absorption peak blue shifts, indicating an increase of quantum confinement and band gap. These three samples are used in this study to investigate the size dependent CS and CR in $CsPbI_3$ perovskite QDs. As the first exciton absorption peaks of these three QDs locate at 676 nm, 665 nm and 650 nm, which are determined by the transient absorption (TA) study to be described below, we therefore denote them as 676 QD, 665 QD and 650 QD in the figures and texts.

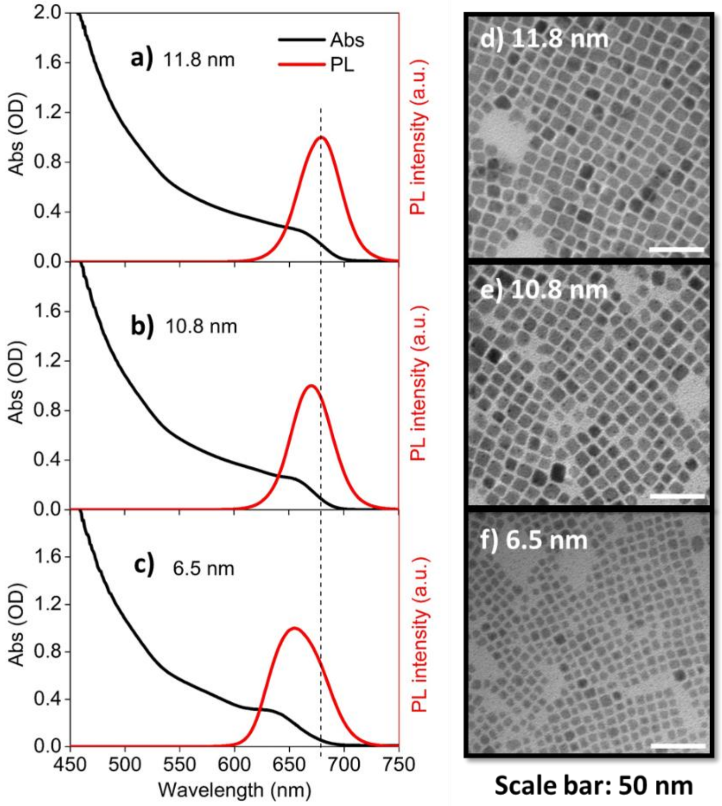

Figure 5.1. Morphology and optical properties of $CsPbI_3$ perovskite QDs. Absorption (black) and emission (red) spectra (a,b,c) and corresponding TEM images (d,e,f) of three QDs of average sizes of (a,d)11.8±1.6 nm, (b,e) 10.8±1.5 nm and (c,f) 6.5±1.1 nm; scale bars in (d-f): 50 nm.

5.2.2. TA study of $CsPbI_3$ QD-RhB complexes

Rhodamine B is selected as model electron acceptors because of its large binding constant on QD surface, suitable energetics, and pronounced absorption band in the visible, following our previous studies.[31, 49] To extract the intrinsic CS rates, a series of $CsPbI_3$ QD-RhBn (n=1-5) samples in heptane/chlorobenzene mixed solution with the same QD concentration and increased RhB concentration (n=1 to 5) were prepared. Because RhB is not soluble in heptane, we first prepared saturated solution of RhB in chlorobenzene and diluted it by a factor of 32, 16, 8, 4 and 1 for sample

RhB1 to RhB5, respectively. Then, a QD solution in heptane and the RhBn solution in chlorobenzene are mixed (volume ratio 5:2) to prepare the series of QD-RhBn samples. Figure 5.2a shows the absorption spectra of 676 QD and its QD-RhBn complexes. The presence of RhB molecules can be seen at the peak at 540-580 nm.

Ultrafast TA spectroscopy were used to measure the CS and CR rates, following previous report of TA study of $CsPbBr_3$ QD-RhB complexes.[31] The details of pump-probe TA setups have been described in Chapter 2. Briefly, a 500 nm pump pulse was focused onto the sample to excite the QDs, and a white light continuum probe pulse was used to record the absorbance change (ΔAbs) as a function of pump-probe delay time. Figure 5.2b and c show the TA spectra of 676 $CsPbI_3$ QDs and 676 QD-RhB5 complexes, respectively. For the free QDs, the TA spectra are dominated by an exciton bleach (XB) feature peaked at ~676 nm, caused by the state filling of the CB electron and VB hole at the band edges. The recovery of XB signal can be used to follow the electron and hole dynamics.[31] For QD-RhB5 complexes, in addition to the XB feature, a ground state bleach signal of RhB forms after the initial recovery of XB signal (Figure 5.2c). Compared with free QDs (Figure 5.2d), the XB of QD-RhB5 shows much faster decay to *ca* half of its initial amplitude, and the remaining half of the XB decay much slower. As will be shown below, these can be attributed to the fast decay of the QD CB electron, and the slower decay of the valence band hole, due to the CS and CR processes shown in Eq. (5.1), respectively. The evidence to support this assignment can be obtained from the comparison of QD XB kinetics with the RhB bleach kinetics. The RhB kinetics was obtained by subtracting the overlapping positive QD signal at 540-580 nm from the total TA signal of QD-RhB by assuming that the QD absorption signal at this wavelength decays with the same kinetics as the QD XB. This assumption is verified in samples of free QDs (without RhB). As shown in Figure 5.2d, the formation of RhB ground state bleach agrees well with the initial decay of the QD XB signal, due to the transfer of the CB electron to the RhB (Scheme 5.1), while the recovery of the RhB bleach follows the kinetics of XB bleach recovery on the slower time scale, indicating the recombination of the electron in the reduced RhB with the VB hole in the QD.

TA measurements under the same conditions were also conducted with other four QD-RhB complexes. The XB decay kinetics have been plotted in figure 5.2d. As more RhB being adsorbed onto QD surface, the XB decays faster due to the faster CS process. To extract the intrinsic CS rates, we assume the CS rate is proportional to the number of electron acceptor and the number of adsorbed RhB obeys Poisson distribution. Based on these assumptions, we derived a model to fit the XB kinetics of QD-RhB series to get the intrinsic CS time constants. Details are provided in Appendix 1.

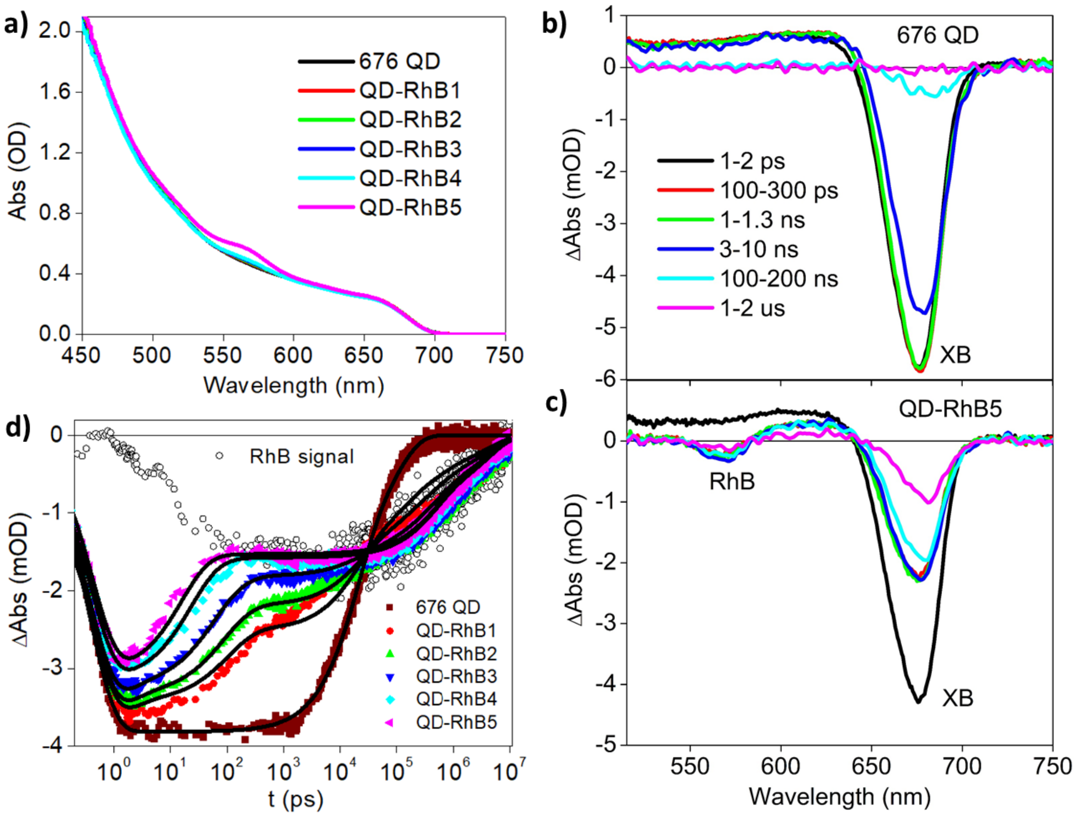

Figure 5.2. TA spectra and kinetics of CsPbI$_3$ QD-RhB complexes. (a) UV-Vis absorption spectra of 676 QDs-RhBn, n=1-5 with increasing RhB loading amount. TA spectra of free 676 QDs (b) and 676 QD-RhB5 complexes (c) measured with 500 nm excitation at indicated delay times from 1 ps to 2 µs.

XB and RhB indicate exciton bleach and RhB ground state bleach features, respectively. (d) XB kinetics of free $CsPbI_3$ QDs (brown squares), XB kinetics of QD-RhB1 to QD-RhB5 and kinetics of RhB ground state bleach (black hollow dots) in QD-RhB5. The RhB signal has been scaled to match the XB recovery at the charge recombination stage. Also shown are fitting results according to the model in Appendix 1 (black solid lines).

Similar TA studies were conducted for the smaller QD samples shown in Figure 5.1. The absorption spectra of 665 QD-RhB series and 650 QD-RhB series are provided in Figure5.3. Figure 5.4a and c show the TA spectra of free 665 QDs and 650 QDs, where the XB peaks blue shift compared with the 676 QDs. Figure 5.4b and d present the XB kinetics of 665 QD-RhB series and 650 QD-RhB series, which can be fit by the same model mentioned above to extract the intrinsic charge separation time constants. Table 5.1 lists the size-dependent CS and CR time constants in QD-RhB systems. Both average CS and average CR time constants decrease at smaller QD sizes.

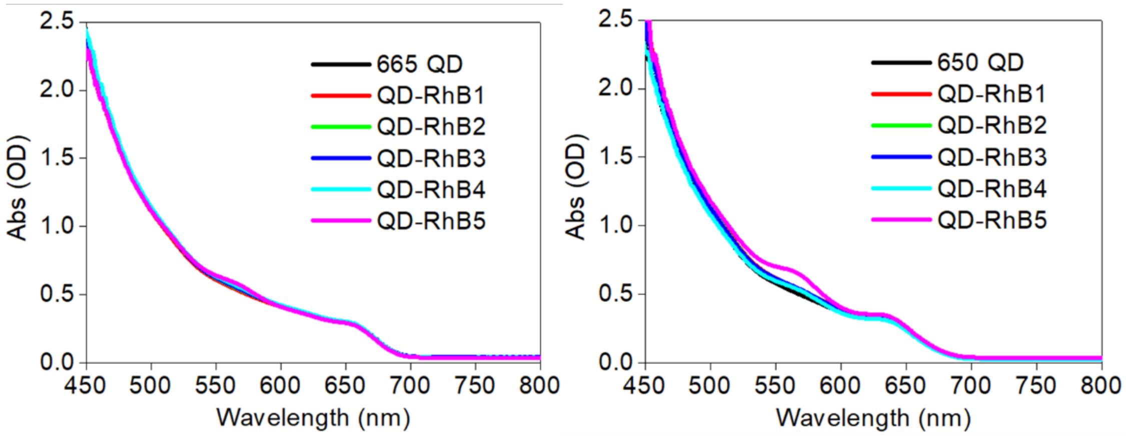

Figure 5.3. Absorption spectra of 665 QD-RhBn series (left panel) and 650 QD-RhBn series (right panel).

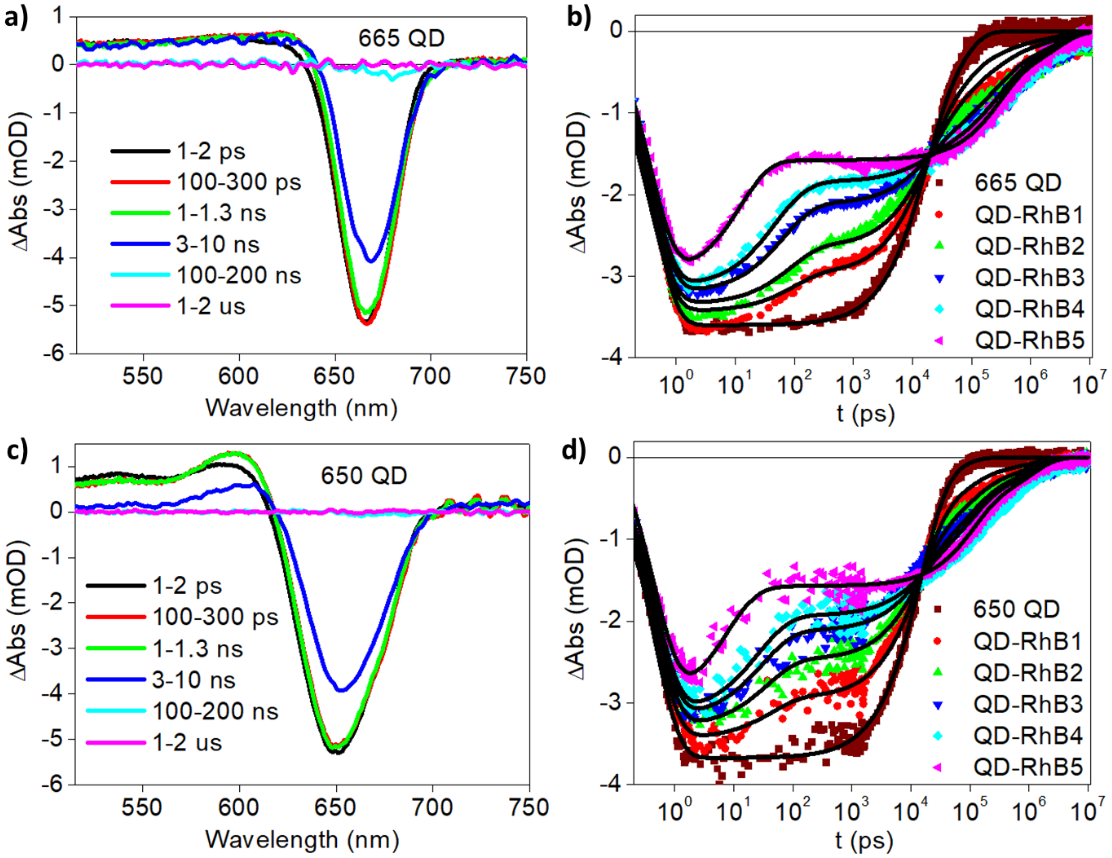

Figure 5.4. TA study of smaller size QDs. (a), (c) TA spectra of free 665 QDs (a) and free 650 QDs (c) measured with 500 nm excitation at indicated delay time from 1 ps to 2 μs. (b) XB kinetics of free 665 QDs (brown squres) and XB kinetics of 665 QD-RhB series. (d) XB kinetics of free 650 QDs (brown squres) and XB kinetics of 650 QD-RhB series. Black solid fitting results according to the model in Appendix 1.

Table 5.1. Size dependent CS and CR time constants in QD-RhB complexes

$CsPbI_3$	QD676-RhB	QD665-RhB	QD650-RhB
QD size (nm)	$\mathbf{11.8 \pm 1.6}$	$\mathbf{10.8 \pm 1.5}$	$\mathbf{6.5 \pm 1.1}$
$e\ contribution$	58.7%	55.3%	57.2%
$\tau_{cs1}\ (ps)$	2.3 (29.4%)	0.02 (27.1%)	0.15 (32.3%)
$\tau_{cs2}\ (ps)$	144.7 (70.6%)	109.2 (72.9%)	51.6 (67.7%)
$\boldsymbol{\tau_{cs(ave)}\ (ps)}$	**102.9**	**79.2**	**35.0**
$\tau_{cr1}\ (ns)$	444 (50.6%)	282 (63.5%)	108 (61.9%)
$\tau_{cr2}\ (ns)$	4220 (49.4%)	2710 (36.5%)	1054 (38.1%)
$\boldsymbol{\tau_{cr(ave)}\ (ns)}$	**2309**	**1168**	**468**

5.2.3. Theoretical calculation of charge transfer rates

To reveal the factors influencing the CS and CR rates, we turn to Marcus's non-adiabatic electron transfer theory.[13] Shown in Eq. 5.2, the ET rate is controlled by the driving force ΔG, the quantum mechanical coupling strength between the initial and final states $|<i|\ H\ |f>|$, and reorganization energy λ.

$$\frac{1}{\tau(T)} = k(T) = \frac{\pi\left|\langle i|\hat{H}|f\rangle\right|^2}{\hbar\sqrt{\pi\lambda k_B T}}\exp\left[-\frac{(\Delta G+\lambda)^2}{4\lambda k_B T}\right]. \qquad (5.2)$$

The driving force is the energy difference of the initial and final electron energy levels, i.e., $\Delta G_{CS} = E_{LUMO} - E_e$ for the charge sparation process and $\Delta G_{CR} = E_h - E_{LUMO}$ for the charge recombination process. E_{LUMO} is the energy of RhB's lowest unoccupied molecular orbital, and E_e and E_h are electron's energy levels in the valence and conduction bands of $CsPbI_3$, respectively. The Hamiltonian matrix element $<i|\ H\ |f>$, coupling the initial and the final states, is related to orbital overlaps, as we show below. The reorganization energy is lattice and molecular geometry deformations and solvent molecule reorientations due to charge transfer. Thus, the following quantities are required: electron levels E_e, E_h, E_{LUMO}, with their corresponding orbital wavefunctions, and geometry relaxation between the neutral and charged quantum dot and, similarly, RhB. To address charge delocalization effects, we treat the total reorganization energy as a sum of three components in Equation 5.3.

$$\lambda = \lambda_{\mathrm{solvent}} + \lambda_{\mathrm{RhB}} + \lambda_{\mathrm{QD}}. \tag{5.3}$$

Estimating the solvent contribution to λ, requires the use of the electrostatic formula.[95] Based on the QD dimension, RhB size and the solvent dielectric, the obtained value for $\lambda_{\mathrm{solvent}}$ is 66 meV. The molecular component λ_{RhB} is defined as the difference between the energy of RhB$^-$ at the equilibrium geometry of RhB, i.e. electron acceptor's initial state, and the energy of RhB$^-$ at the equilibrium geometry of RhB$^-$, its final state. For this we use the B3LYP functional[96-97] with a 6-31++G(d,p) basis, with diffuse functions specifically added to properly describe the anion, as implemented in Gaussian 09.[98] The calculated value is $\lambda_{\mathrm{RhB}} = 0.488$ eV. The reorganization energy of the QD（λ_{QD}） is difficult to estimate using conventional electronic structure methods due to computational complexity. As discussed below, the unknown λ_{QD} is treated as an adjustable parameter which can be determined from the ratio of the measured charge separation and recombination rates.

Using the result of our previous investigations,[45,46] the transition matrix element from the conduction band of $\mathrm{CsPbI_3}$ to the lowest unoccupied molecular orbital (LUMO) of RhB, neglecting the mixing of excited states, is approximated as

$$H_{\mathrm{CS}} = \langle \psi_e | \hat{H} | \psi_{\mathrm{LUMO}} \rangle = \langle \psi_e | \psi_{\mathrm{LUMO}} \rangle (E_e + E_{\mathrm{LUMO}}) \tag{5.4a}$$

and from the LUMO to the valence band as,

$$H_{\mathrm{CR}} = \langle \psi_{\mathrm{LUMO}} | \hat{H} | \psi_h \rangle = \langle \psi_{\mathrm{LUMO}} | \psi_h \rangle (E_h + E_{\mathrm{LUMO}}). \tag{5.4b}$$

In Eq. 5.4a and 5.4b, ψ_{LUMO} is the LUMO orbital of RhB with an energy E_{LUMO}. Calculating the overlaps requires an estimate of the distance of approach of RhB to the surface of the quantum dot. To this end, we approximate QD's finite area surface by an infinite bulk surface and calculate molecule-surface interaction using a density functional theory with a plane wave basis. To proceed with evaluating Eqs. 5.4, we use the fact that the orbital overlap factors are dominated by the envelope parts of the corresponding full orbitals, since electron transfer across QD/RhB interface is manifestly a non-local process. Table 5.2 summarizes the overlaps, electronic coupling strength factors and transition energies.

Table 5.2. Orbital overlaps, quantum mechanical coupling factors H (in meV) calculated using Eqs 5.4 and the orbital energies, and driving force ΔG (eV), for cubic $CsPbI_3$ dots of side L (nm). The CB of $CsPbI_3$ is at -3.7 eV, and VB at -5.4 eV. The energy of RhB LUMO is -3.95 eV.[49, 99]

L (nm)	$<\psi_e \vert \psi_{\mathrm{LUMO}}>$	$<\psi_{\mathrm{LUMO}} \vert \psi_h>$	H_{CS} (meV)	H_{CR} (meV)	ΔG_{CS} (eV)	ΔG_{CR} (eV)
6.5	1.790e-3	1.602e-3	-13.6	-15.0	-0.289	-1.467
10.8	6.624e-4	5.803e-4	-5.1	-5.4	-0.243	-1.433
11.8	5.058e-4	4.558e-4	-3.9	-4.3	-0.238	-1.430

Analysis of the results shows that the size dependence of both rates should derive primarily from the quantum mechanical coupling factors H_{CS} and H_{CR} and only weakly from the driving force. The latter changes very slowly with the dot size, as controlled by the electron and hole energy levels. Furthermore, the ratio of the measured rates, $k_{\mathrm{CS}}/k_{\mathrm{CR}}$, is nearly constant with dot size (refer to Table 5.1), reinforcing the proposition that size dependence of the rates is primarily controlled by the orbital overlaps since they show up in the pre-exponential factor. This allows us to introduce the following equivalences, and, linking the "exact", but unknown, quantum mechanical coupling element with the approximate one of Eqs. 5.4 via an undetermined constant α, the same for both processes. Therefore, it is convenient to require that the ratio of the theoretical rates align with the measured one by variation of the unknown λ_{QD}, while the absolute values of the rates are determined by α. With this, the best value of λ_{QD}, in the least squares sense, is found to be 40 meV, and thus the total reorganization energy becomes 0.594 eV. (The resultant rates, with $\alpha = 1$, are depicted in Figure 5.5.) Using the calculated rates, the best value for α which adjusts the absolute values of the rates, also in a least squares sense, is determined to be ~0.33. In other words, the calculated coupling strengths are overestimated, on average over the QD/molecule systems, by about a factor of 3. This result is consistent with the level of theory used in this work, which approximates the true orbital functions by their envelope parts.

In the past, we have argued that the total reorganization energy in cadmium chalcogenide QD/molecule systems is dominated by the molecule's part, that is, $\lambda_{QD}/\lambda_{RhB} \approx 0$, simply based on the size difference and corresponding orbital delocalization effects.[45] The present calculations suggest the ratio is ~0.08 in these perovskite QDs, arguably greater than expected. As a possible interpretation, we propose that these QDs undergo relatively large local structural changes upon oxidation/reduction due to the nature of the $CsPbI_3$ perovskite cell, where both the cation location and orientation and the PbI bond length can respond more readily to charge changes. This finding is consistent with many recent studies that have suggested that carriers in perovskite films form polarons, in which they are stabilized by deformation of the lattice.[48,49]

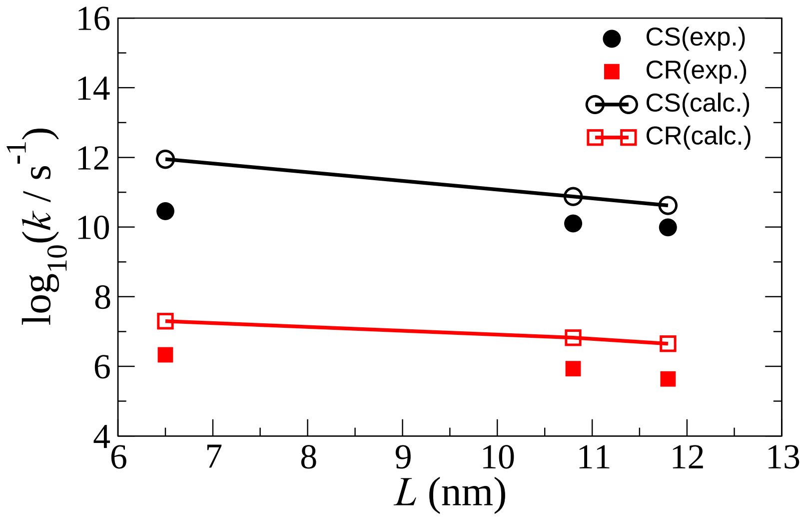

Figure 5.5. Size dependent charge separation (CS) and charge recombination (CR) rates at 300K. Filled circles and squares are the experimental values extracted from XB kinetics (Table 5.1). The lines with open circles and squares are piecewise linear interpolations of the unscaled ($\alpha = 1$) theoretical calculation results (Eq. 5.2). with λ_{QD} variationally determined to be 40 meV.

While in previous reports of size dependent charge transfer from cadmium chalcogenide QD, the driving force term has remarkable influences,[24-25, 93] the size dependent CS and CR rate trends in perovskite QDs result mainly from electronic coupling strength with little influence of driving forces, revealing a distinguishing characteristic. The cadmium chalcogenide QDs studied in previous papers fall in the strong quantum confinement regime, in which both the coupling strength and electron and hole energy change with size. For the perovskite QDs studied here, the effect of quantum confinement is weak (54 meV for the electron and 46 meV for the hole in QD676); in this regime, the energy changes weakly, but the coupling strength changes more pronouncedly with the QD size. In fact, the latter is represented very well by an inverse proportionality law of the overlap squared, i.e. the quantity proportional to QD surface charge density, with the QD volume, as shown in Figure 5.6. This result confirms that in the weak quantum confinement regime, the change of surface electron density results mainly from the change of overall volume of the QD.

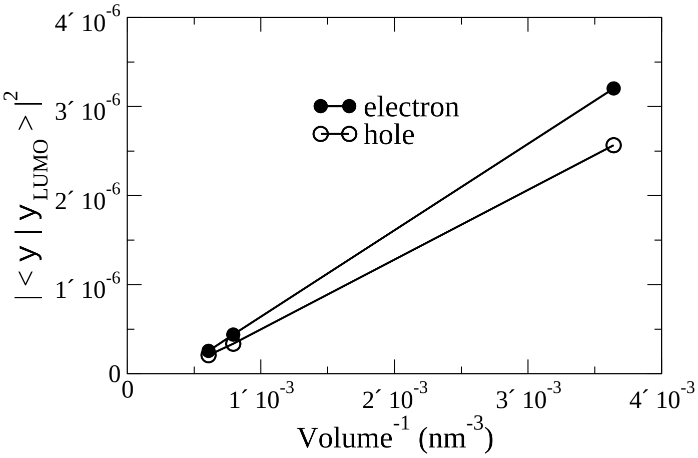

Figure 5.6. Squared overlaps of the electron and hole wavefunctions (ψ) with the LUMO plotted as functions of the inverse volume of the QD, data taken from Table 5.2.

5.3. Conclusion

In conclusion, we have studied the size dependent charge separation and recombination rates in $CsPbI_3$ QD-RhB complexes by transient absorption spectroscopy and computational modelling in this chapter. With average QD size ranging from 6.5 nm to 11.8 nm, the average CS and CR time constants change from ~35.0 ps to ~102.9 ps and from ~468 ns to ~2.3 μs, respectively. Theoretical calculations show that the size dependent electronic coupling strength (H_{CS} and H_{CR}) between the $CsPbI_3$ QD and RhB is the primary factor for the significant decrease of charge transfer rates with the QD size, with virtually negligible contribution from the size dependent driving force change. This behavior for the weakly quantum confined perovskite QDs differs from the more strongly quantum confined cadmium chalcogenide QDs in reported literatures.[24-25, 93] In photovoltaic and photocatalytic applications, fast and efficient charge separation is beneficial, while fast charge recombination limits the carrier extraction efficiency. From this perspective, optimized performance may be achieved by considering the trade-off between CS and CR rates in $CsPbI_3$ QDs with different sizes. In next chapter we start measuring the charge transfer processes in CsPbI3 QD-metal oxide films, which is directly related to the power conversion efficiency of thin-film solar cells.

Appendix 1. XB kinetics fitting model

To extract CS and CR rates from XB kinetics, first we fit the XB kinetics of free QDs with a two-exponential decay function (A.5.1) convoluted with IRF and fit the XB kinetics of QD-RhB5 complexes with a four-exponential decay function (A.5.2) convoluted with IRF:

$$XB(t) = XB(0) \cdot [\sum_{i=3}^{4} a_i \cdot e^{-t/\tau_i} - e^{-t/\tau_f}] \quad (A.5.1),$$

$$XB(t) = XB(0) \cdot [\sum_{i=1}^{4} a_i \cdot e^{-t/\tau_i} - e^{-t/\tau_f}] \quad (A.5.2),$$

where $XB(0)$ is the initial signal size, a_i and τ_i are the amplitude and time constant of multi-exponentials, and τ_f is the signal formation time constant. The fitting parameters are listed in Table A.5.1. The slower time constants in QD-RhB5 are CR time constants (τ_3, τ_4).

Table A.5.1. Fitting parameters for XB kinetics of QD and QD-RhB5

	τ_f/fs	τ_1/ps (a_1)	τ_2/ps (a_2)	τ_3/ns (a_3)	τ_4/ns (a_4)
QD676	400 ± 20	–	–	18.7 ± 1.3 (63.0 ± 3.0%)	98.0 ± 12.0 (37.0 ± 3.0%)
QD676-RhB5	418 ± 32	1.5 ± 0.8 (17.8 ± 2.0%)	13.6 ± 0.4 (40.9 ± 1.0%)	444 ± 40 (20.9 ± 1.8%)	4220 ± 320 (20.4 ± 3.2%)
QD665	358 ± 33	–	–	14.5 ± 0.5 (63.9 ± 2.0%)	56.8 ± 6.2 (36.1 ± 2.0%)
QD665-RhB5	424 ± 20	3.1 ± 0.5 (13.5 ± 2.5%)	14.9 ± 0.6 (41.8 ± 2.7%)	282 ± 14 (28.4 ± 1.4%)	2710 ± 150 (16.3 ± 2.7%)
QD650	450 ± 22	–	–	14.2 ± 0.4 (87.5 ± 1.5%)	51.1 ± 20.0 (12.5 ± 1.5%)

QD650-RhB5	492 ± 24	–	8.4 ± 1.6 (57.2 ± 7.8%)	108 ± 21 (26.5 ± 2.5%)	1054 ± 80 (16.3 ± 4.7%)

Further, we derive the following model to fit the XB kinetics of QD-RhB1 to QD-RhB5 to extract the intrinsic CS time constants. We assume the adsorption number of RhB molecules obeys Poisson distribution:

$$f(n,m) = \frac{m^n e^{-m}}{n!} \qquad (A.5.3)$$

where m is the average number of RhB on a QD.[90] The CS rates are assumed to be proportional to the number of adsorbed RhB molecules. The XB kinetics of QD-RhB complexes can be written as the combination of free QD XB kinetics and QD-RhB XB kinetics as follows:

$$XB(t) = XB(0) \cdot \left\{ e^{-t/\tau_f} - f(0,m) * g(t)_{free\ QD} - \sum_{n=1}^{\infty} f(n,m) * \left(a_e \cdot e^{-nk_1 t} + a_h \cdot e^{-k_r t}\right) \right\} \qquad (A.5.4)$$

where $f(0,m)$ is the proportion of free QDs, $g(t)_{free\ QD}$ is the XB decay function of free QDs, k_1 is the intrinsic CS rate constant, a_e is the electron contribution to XB, k_r is the CR time constant and a_h is the hole contribution to XB. $g(t)_{free\ QD}$, a_e, a_h and two components of k_r can be obtained from Table A.5.1. In the real fitting process, we write the Poisson distribution until n = 15. Also, two components of CS are required to fit the XB kinetics. Therefore, the fitting function of 676 QD-RhB series is:

$$XB(t) = XB(0) \cdot \left\{ e^{-t/\tau_f} - f(0,m) * g(t)_{free\ QD} - \sum_{n=1}^{15} f(n,m) * [0.587 \cdot (a_1 \cdot e^{-nt/\tau_{cs1}} + (1-a_1) \cdot e^{-nt/\tau_{cs2}}) + 0.413 \cdot (a_3 \cdot e^{-t/\tau_{cr1}} + a_4 \cdot e^{-t/\tau_{cr2}})] \right\} \qquad (A.5.5).$$

The fitting function of 665 QD-RhB series is:

$$XB(t) = XB(0) \cdot \left\{ e^{-t/\tau_f} - f(0,m) * g(t)_{free\ QD} - \sum_{n=1}^{15} f(n,m) * [0.553 \cdot (a_1 \cdot e^{-nt/\tau_{cs1}} + (1-a_1) \cdot e^{-nt/\tau_{cs2}}) + 0.447 \cdot (a_3 \cdot e^{-t/\tau_{cr1}} + a_4 \cdot e^{-t/\tau_{cr2}})] \right\} \qquad (A.5.6).$$

The fitting function of 650 QD-RhB series is:

$$XB(t) = XB(0) \cdot \left\{ e^{-t/\tau_f} - f(0,m) * g(t)_{free\ QD} - \sum_{n=1}^{15} f(n,m) * [0.572 \cdot (a_1 \cdot e^{-nt/\tau_{cs1}} + (1-a_1) \cdot e^{-nt/\tau_{cs2}}) + 0.428 \cdot (a_3 \cdot e^{-t/\tau_{cr1}} + a_4 \cdot e^{-t/\tau_{cr2}})] \right\} \qquad (A.5.7).$$

The fitting parameters are m, a_1, τ_{cs1}, τ_{cs2}. The fitting is done by minimizing $\sum(XB_{fit} - XB_{data})^2$ in Excel. The fitting results are plotted in Figure 5.2d, 5.4b and 5.4d. Fitting parameters are listed in Table A.5.2.

Table A.5.2. Fitting parameters for XB kinetics of QD-RhB series

Samples	m	a_1 (%)	τ_{cs1} (ps)	τ_{cs2} (ps)
676 QD-RhB1	0.9	29.4 ± 0.003	2.3 ± 0.03	144.7 ± 31.0
676 QD-RhB2	1.3			
676 QD-RhB3	2.2			
676 QD-RhB4	6.1			
676 QD-RhB5	9.2			
665 QD-RhB1	0.4	27.1 ± 0.004	0.02 ± 0.0002	109.2 ± 44.6
665 QD-RhB2	0.7			
665 QD-RhB3	1.4			
665 QD-RhB4	2.1			
665 QD-RhB5	8.8			
650 QD-RhB1	0.4	32.3 ± 0.012	0.15 ± 0.003	51.6 ± 19.0
650 QD-RhB2	0.8			
650 QD-RhB3	1.3			
650 QD-RhB4	1.8			
650 QD-RhB5	6.5			

Chapter 6. Charge transfer at the interface of $CsPbI_3$ QDs and metal oxide layer

6.1. Introduction

The overall solar to electricity conversion process of perovskite QD solar cells involves many processes, such as carrier transport within the QD film, carrier transfer at the interface with electron and hole extraction layers and competing charge recombination processes. Optimization of the rates of these processes is key to rational improvement of device performance. In this chapter, we investigate the interfacial electron transfer (ET) and charge recombination (CR) dynamics between $CsPbI_3$ perovskite QDs and metal oxide (MO) nanoparticle (NP) films (see Eq. 6.1 and Scheme 6.1).

$$\mathrm{CsPbI_3(e-h)} + \mathrm{MO} \overset{ET}{\rightarrow} \mathrm{CsPbI_3(h)} + \mathrm{MO(e)} \overset{CR}{\rightarrow} \mathrm{CsPbI_3} + \mathrm{MO} \quad (6.1)$$

In Eq. (6.1), MO represents zinc (ZnO) or titanium (TiO_2) oxide. By transient absorption (TA) spectroscopy, we observed that there exist two subpopulations with very different ET and CR rates. For each subpopulation, the ET and CR kinetics can be adequately described by bi-exponential functions. The average ET and CR time constants were determined to be (0.85 ± 0.05 and 5.0 ± 0.5 ns) on ZnO and (0.070 ± 0.007 and 0.90 ± 0.05 ns) on TiO_2, respectively, for ~80% QDs on the films. The remaining 20% shows much slower charge separation and recombination rates. By comparing ET times and the intrinsic electron-hole recombination rate (measured on an ET-inactive substrate, Al_2O_3), we estimated that ET efficiencies from QDs to ZnO and TiO_2 are 61.3% and 88.7%, respectively, suggesting that TiO_2 is a better electrode for electron extraction. We discuss implications of these rates on the efficiency of QD solar cells.

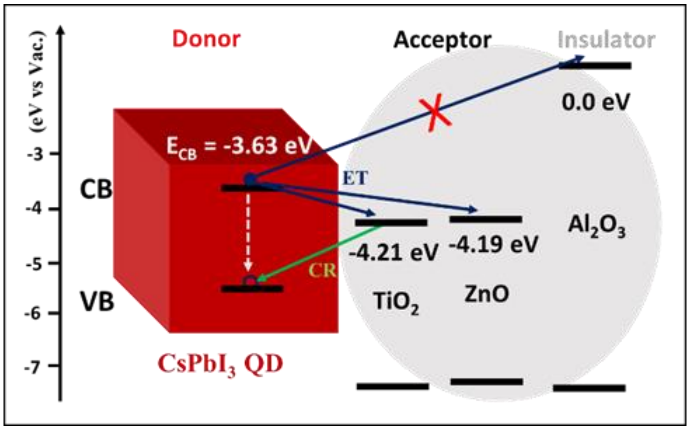

Scheme 6.1. Schematic energy level diagram and charge separation and recombination pathways at the $CsPbI_3$ QD/metal oxide (MO) NP Interface: conduction band (CB) and valence band (VB) edges in $CsPbI_3$, TiO_2, ZnO and Al_2O_3 (black horizontal solid lines), electron transfer (ET) from QD to MO (dark blue arrows), back charge recombination (CR) process (green arrow), and electron-hole recombination inside the QD (dashed grey arrow).

6.2. Results and discussion

6.2.1. Sample characterizations

$CsPbI_3$ QDs were synthesized according to a published hot injection method (see Chapter 2 for details).[19-20, 46] The absorption and emission spectra of $CsPbI_3$ QDs in heptane (Figure 6.1a) show a band gap at ~1.81 eV and broad absorption across most of the visible spectrum. Consistent with previous reports,[7, 19-20, 46, 59, 100] these QDs are in cubic crystal phase and exhibit typically orthorhombic shapes in TEM images (Figure 6.1b) with an average edge length of 12.7 nm. The reported valence band (VB) positions of $CsPbI_3$ bulk crystals (~-5.4 V *vs.* vacuum)[63, 101] and QDs[102] (-5.44 V *vs.* vacuum) are similar because of the weak quantum confinement in these QDs. The CB edge position is estimated to be -3.63 V from the known band gap (1.81 eV) by neglecting the weak e-h coulomb binding energy

(~20 meV[46]). The CB positions of ZnO and TiO_2 NPs were reported to be -4.19 and -4.21 V versus vacuum at the zero point of charge (pH 8.8 and 5.8, respectively)[103-104] (Scheme 6.1). Therefore, the corresponding driving forces for ET and CR are (0.56 and 1.25 eV) and (0.58 and 1.23 eV) at QD/ZnO and QD/TiO_2 interfaces, respectively.

ZnO and TiO_2 nanocrystalline thin films were fabricated by doctor-blading colloidal solution (NP diameter 20-30 nm) onto sapphire substrates and annealing at 450 °C for 1h.[25, 57-58, 105] Al_2O_3 nanocrystalline thin films were also fabricated as a control sample of no electron injection because of its much higher CB band edge.[45, 91] The annealed NP films were immersed in concentrated $CsPbI_3$ QDs solution for 48 h,[25] followed by heptane rinse to remove weakly adsorbed QDs on the films. Adsorption of QDs on these films were confirmed by photographs (Figure 6.1a inset) and absorption spectra (Figure 2.5) of QD-MO NP films. Further details for sample preparation have been described in Chapter 2.

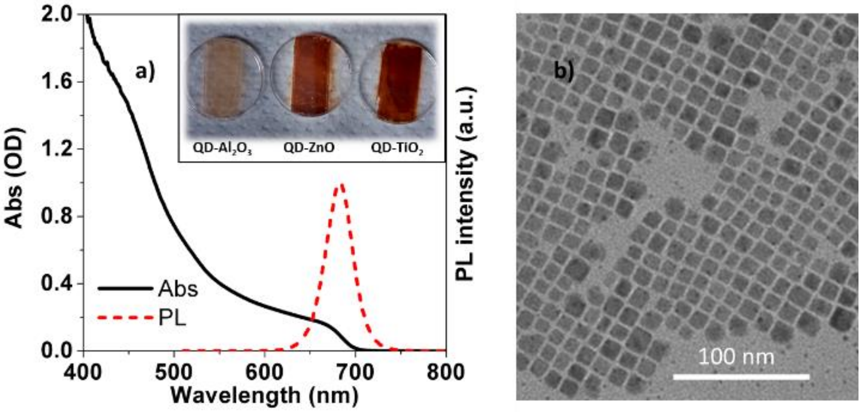

Figure 6.1. Absorption spectrum and TEM image of $CsPbI_3$ perovskite QDs. (a) Absorption (black solid line) and photoluminescence (red dashed line) spectra of $CsPbI_3$ QDs dispersed in heptane. Inset: Photograph of QD-MO NP films. (b) Representative TEM image of QDs. The average edge size is 12.7 nm.

6.2.2. TA study of charge transfer in $CsPbI_3$ QD-metal oxide films

Ultrafast TA spectroscopy measurements were conducted to investigate the ET and CR processes. The details of pump-probe TA setups are described in the Chapter 2. To avoid the influence of multi-exciton dynamics, pump power dependent TA measurements were conducted (see Appendix 1) for details) and all the TA results discussed below were obtained under low pump fluence (0.80-1.09 uJ/cm^2) at which TA signal is dominated by QDs in the single exciton state.

Figure 6.2a, b and c show the TA spectra of $CsPbI_3$ QDs on Al_2O_3, ZnO and TiO_2 NP films, respectively. The TA spectra are dominated by an exciton bleach (XB) feature peaked at ~680 nm, caused by the state filling of the CB electron and VB hole at the band edges. The recovery of XB signal can be used to follow the electron and hole dynamics.

As to the electron and hole contributions to the XB signal, we have presented TA study of QD-Rhodamine B (RhB) complexes in Chapter 4. In these $CsPbI_3$ QDs, the state fillings of electron and hole contribute ~51.6% and 48.4%, respectively, to the XB feature. The result is consistent with the reported similar effective masses of electron and hole in bulk $CsPbI_3$ ($0.11m_0$ and $0.13\ m_0$, respectively; m_0 is the mass of free electron).[46]

Kinetics of XB features of QDs on Al_2O_3, TiO_2, ZnO are compared in Figure 6.2d, and parameters of their multiple exponential fits are listed in Table A.6.1. In all cases, The XB features formed with a rise time of 0.22±0.01 ps, corresponding to the hot carrier relaxation time to the lowest excitonic state (X1) upon 500 nm excitation. The kinetic traces show a fast XB recovery with a time constant (amplitude) of ~4.0 ps (~6.0%) of the total amplitude in all three film samples, including Al_2O_3, in which ET from QD is energetically forbidden (Scheme 6.1). Because this decay component is not observed in TA kinetics measured in solution phase, we attribute it to ultrafast carrier trapping, likely caused by the partial loss of QD passivating ligands upon their transfer to MO surface. The dominant XB recovery time in QD-Al_2O_3 is 2.5 ns (~81.6%), which is considerably faster than that of $CsPbI_3$

QDs in solution (6.3 ns, Figure 6.3b, Table A.4.1), and is attributed to enhanced e-h nonradiative recombination for QDs on oxide surfaces.

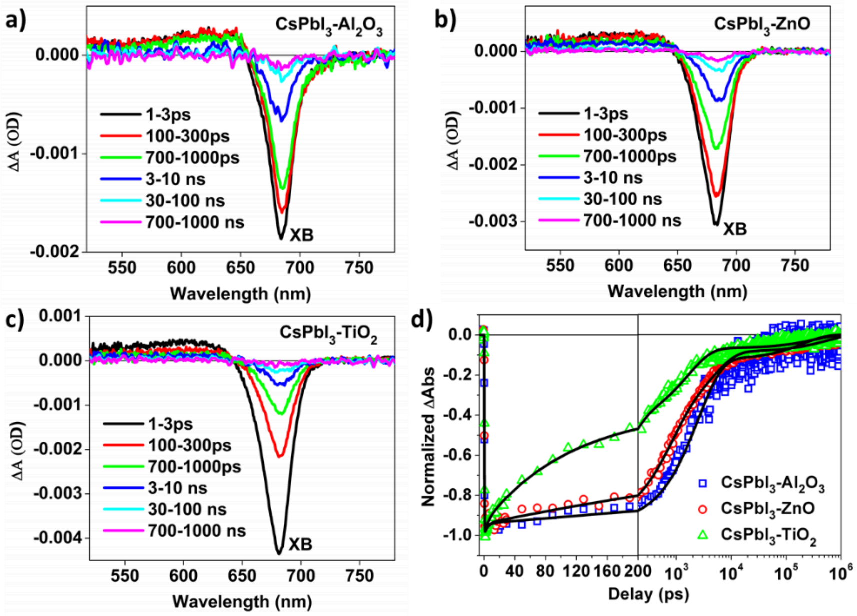

Figure 6.2. TA spectra and kinetics of CsPbI$_3$ perovskite QDs on metal oxide NP films measured with 500 nm excitation. TA spectra of CsPbI$_3$ QDs on Al$_2$O$_3$ (a), ZnO (b) and TiO$_2$ (c) NP films at indicated time delays after 500 nm excitation. The dominant signal is exciton bleach (XB) peaked at ~680 nm. (d) Comparison of XB recovery kinetics of CsPbI$_3$ QDs on Al$_2$O$_3$ (blue squares), ZnO (red circles) and TiO$_2$ (green triangles) NP films. Black solid lines are multi-exponential fits according to the model provided in Appendix 2.

6.2.3. Analysis of PL decay and XB kinetics

In the presence of ZnO and TiO$_2$, the XB recoveries are accelerated (Figure 6.2d), caused by ET from the QD to MO. To further affirm this assignment, time-resolved photoluminescence (PL) decay was measured for the same samples. As shown in Figure 6.3a, the PL decay becomes faster from Al$_2$O$_3$ to ZnO and TiO$_2$, consistent with the trend of XB recovery. It is important to point out that PL decay probes the exciton (e-h pair) dynamics, complete decay of the CB electron (or VB hole) by any pathways (e-h recombination, electron trapping or ET to MO) leads to a complete PL decay. XB bleach probes the sum of electron and hole population and complete decay of CB electron by ET to MO only leads to a partial decay of XB signal (with the hole contribution remaining). Thus, it is informative to compare the PL decay and XB bleach kinetics (Figure 6.3b-d), although the PL decay curves miss data points at short delay time (<110 ps) due to a lower time resolution of PL measurement. For QDs on Al_2O_3 (Figure 6.3b) the PL decay and XB kinetics match well with each other, indicating that electron-hole recombination dominates the excited state decay. For QDs on ZnO and TiO_2 films, there exist slow XB recovery component beyond the complete PL decay (Figure 6.3c and d). These results are consistent with ET from QD to oxides, which leads to complete (and fast) PL decay, while the remaining hole in the QD is responsible for the slower XB recovery (by charge recombination, Scheme 6.1).

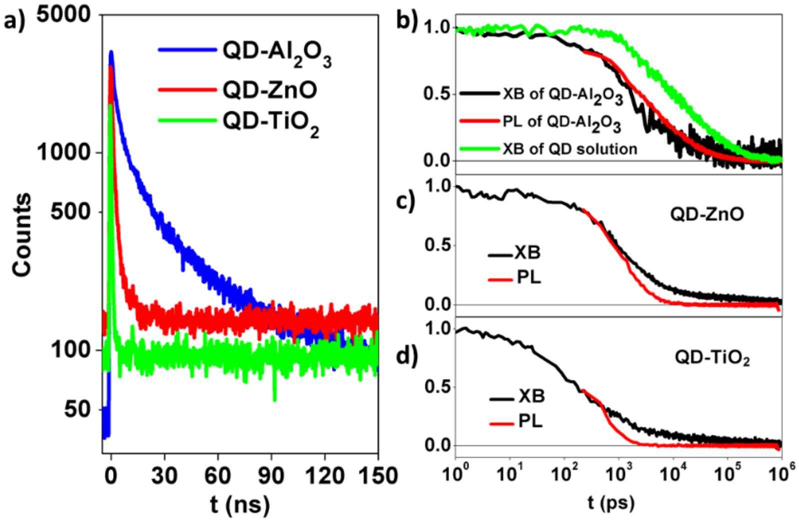

Figure 6.3. PL decay kinetics of $CsPbI_3$ QDs on MO. a) Comparison of PL decay on Al_2O_3, ZnO and TiO_2. b-d) Comparison of PL decay (red) and XB kinetics (black) on b) Al_2O_3, c) ZnO and d) TiO_2. Green curve in panel b) is the XB kinetics of QDs in solution.

The XB bleach and PL decay kinetics can be fit according to a model that accounts for carrier trapping, e-h recombination, interfacial ET and CR (scheme 6.1). Details of the model are provided in Appendix 2. The rate constants for carrier trapping and exciton recombination are assumed to be the same as QDs on Al_2O_3. Best fit of the XB bleach (Figure A.6.6, Table A.6.2, Table A.6.3) reveals two subpopulations: approximate 80% (79.9 ± 1.7% and 81.3 ± 1.5% on ZnO and TiO_2, respectively) of QDs show ET and CR time constants of (0.85 ± 0.05 ns, 5.0 ± 0.5 ns) on ZnO and (0.070 ± 0.007 ns, 0.90 ± 0.05 ns) on TiO_2, respectively; and the remaining ~20% QDs have much slower ET and CR time constants of (60 ± 7 ns, 1300 ± 400 ns) on ZnO and (0.80 ± 0.05 ns, 250 ± 60 ns) on TiO_2, respectively. The same model also fit the PL decay well (Figure A.6.7 and Table A.6.5), providing further support for this model. The existence of two subpopulations of QDs with very different ET and CR rates can be attributed to heterogeneities of QD surfaces and/or QD-MO contacts. [106-107]

6.2.4. Implications on perovskite thin-film solar cells

High conversion efficiency in solar cells requires fast and efficient charge separation, and slow exciton recombination and charge recombination.[108] Electron transfer at the bulk $MAPbI_3$-TiO_2 interfaces, has been reported to occur on the sub-ps time scale,[91, 109-110] much faster than the ET rate at the $CsPbI_3$ QD/TiO_2 interface studied in this work. The reason for such large discrepancy is unclear, although it is possible that ligands on the QD surfaces may reduce the electronic coupling strength with the MO electron extraction layer.[111] These ligands might also induce a heterogeneity in interfacial contact configuration and hence electronic coupling strength between QDs and MO, which is likely responsible for the observed two populations of QDs with very different ET and CR rates. Thus, it is important to critically investigate the interfacial structure and its effect on charge transfer properties in future studies. From the ET and intrinsic e-h recombination rates of QDs on MO, the overall ET efficiencies are estimated to be 61.3% and 88.7% on ZnO and TiO_2 films, respectively (Table A.6.4).

Fast ET from QDs to MO is followed by a fast charge recombination on the nanosecond time scale, which may lead to recombination loss unless there exist faster hole removal pathways through either hole transport through QD films or extraction by hole acceptors. The less than unity electron injection efficiency and considerable recombination loss observed in these perovskite QD/MO interfaces suggest the possibility of further improvement for interfacial charge separation. In the reported $CsPbI_3$ QD solar cells (PCE 10.77%),[9] QDs with less surface ligands achieved by anti-solvent (methyl acetate) washing were used to increase the electronic coupling strengths between stacking QDs as well as between QDs and electron/hole extraction layer. This is probably a key reason why the high power conversion efficiency was achieved. It is also interesting to note that both the ET and CR rates at QD/TiO_2 interface is ~5-10 times faster than those at QD/ZnO interface, suggesting that these processes depend sensitively on the nature of extraction layer material, which may allow rational optimization of these rates.

6.3. Conclusion

In conclusion, we have investigated the interfacial electron transfer and charge recombination kinetics at all-inorganic $CsPbI_3$ perovskite QDs/MO (ZnO and TiO_2) nanoparticle interface by TA and PL decay measurements. By comparison of kinetics of $CsPbI_3$ QDs on Al_2O_3, ZnO and TiO_2 films, we determined the ET time constants to be 0.85 ± 0.05 ns and 0.070 ± 0.007 ns for ~80% QDs on ZnO and TiO_2, respectively, while the remaining ~20% QDs have ET and CR time constants of (60 ± 7 and 1300 ± 400 ns) on ZnO and (0.80 ± 0.05 and 250 ± 60 ns) on TiO_2, respectively. Our study reveals important heterogeneity and MO material dependence in ET and CR rates. In the coming chapter, we go on studying the influence of QDs surface ligand quantity on charge transfer rates in QD-TiO2 films. These works may help identify rational approaches for improving the device performance.

Appendix 1. Pump power dependent TA measurements

To eliminate the multi-exciton interactions in QDs on the films, we used low pump densities and measured the power dependent TA. Figure S3, S4 and S5 show the results of $CsPbI_3$ QDs on Al_2O_3, ZnO and TiO_2 NP films, respectively. From the kinetics plotted in the last panel in each figure, we confirm the single exciton region dominated by QDs in single exciton states. For QDs on Al_2O_3, when pump densities are within 1.40 uJ/cm^2, the XB recovery curves match mutually, indicating the negligibility of multi-exciton effect. Similarly, for QDs on TiO_2 and ZnO, when the excitation densities are 0.28-0.88 uJ/cm^2 and 0.19-1.25 uJ/cm^2, respectively, the XB recovery curves match mutually because of the negligibility of multi-exciton effect. Thus, the TA spectra and kinetics in the main text are within the single exciton region. Figure S6 shows the linear dependence of XB signal amplitudes on excitation densities within single exciton region.

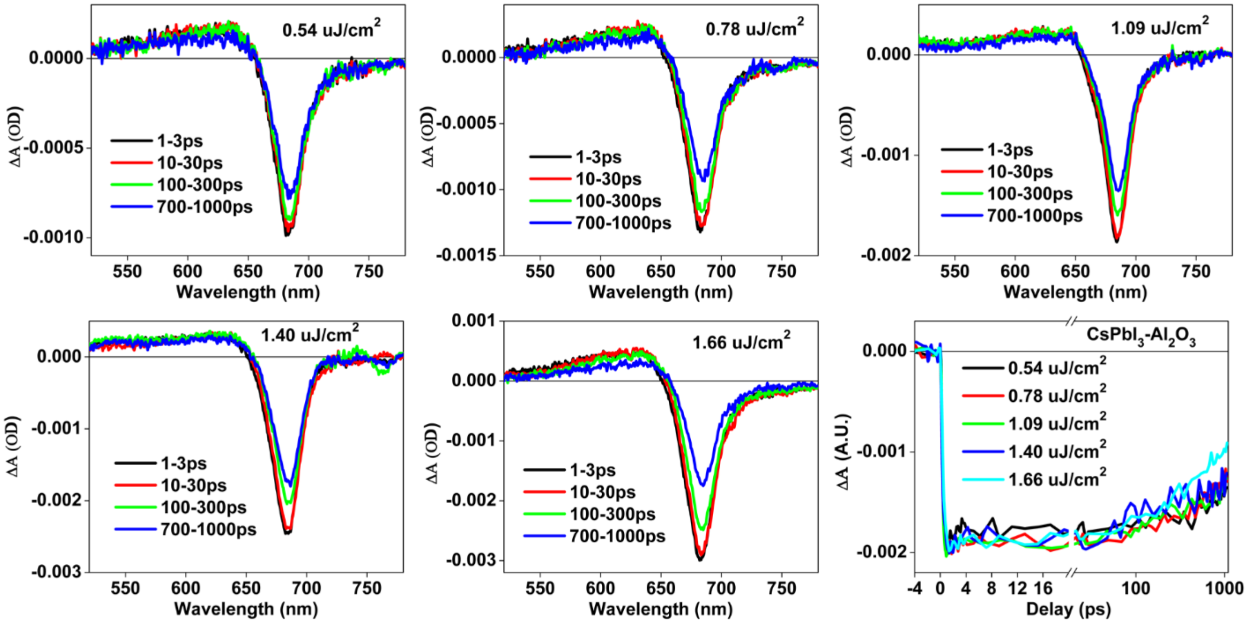

Figure A.6.1. TA spectra of $CsPbI_3$ QDs on Al_2O_3 NP film measured at different excitation densities. The right bottom panel compares the XB recovery kinetics at different excitation densities.

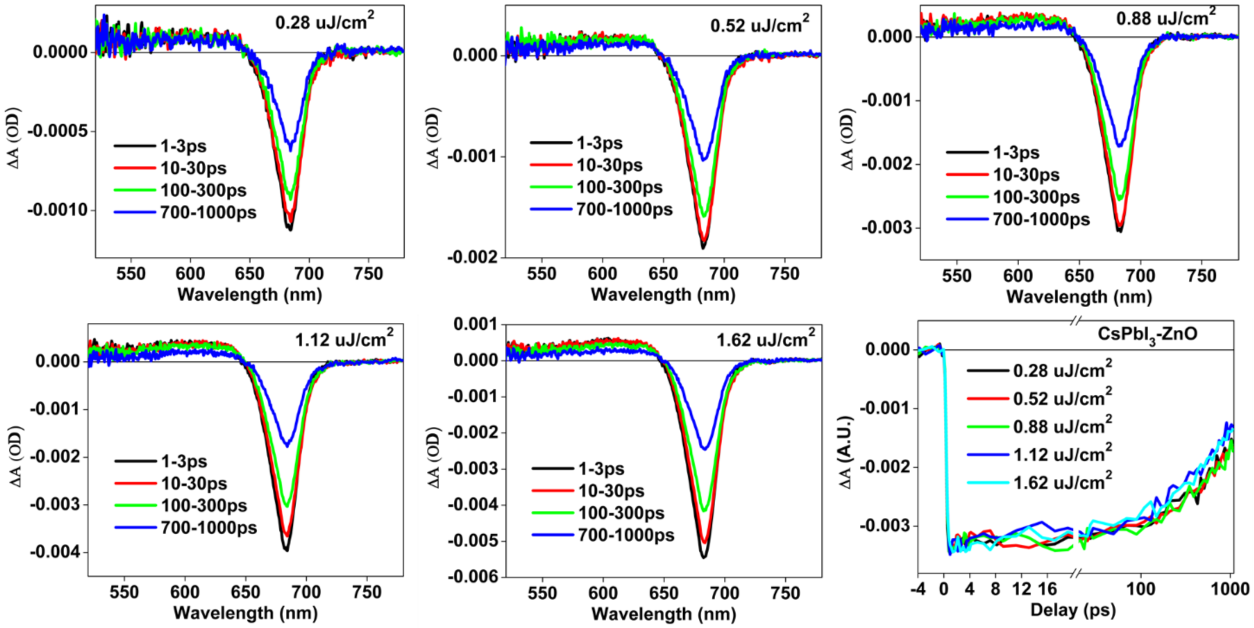

Figure A.6.2. TA spectra of CsPbI$_3$ QDs on ZnO NP film measured at different excitation densities. The right bottom panel compares the XB recovery kinetics at different excitation densities.

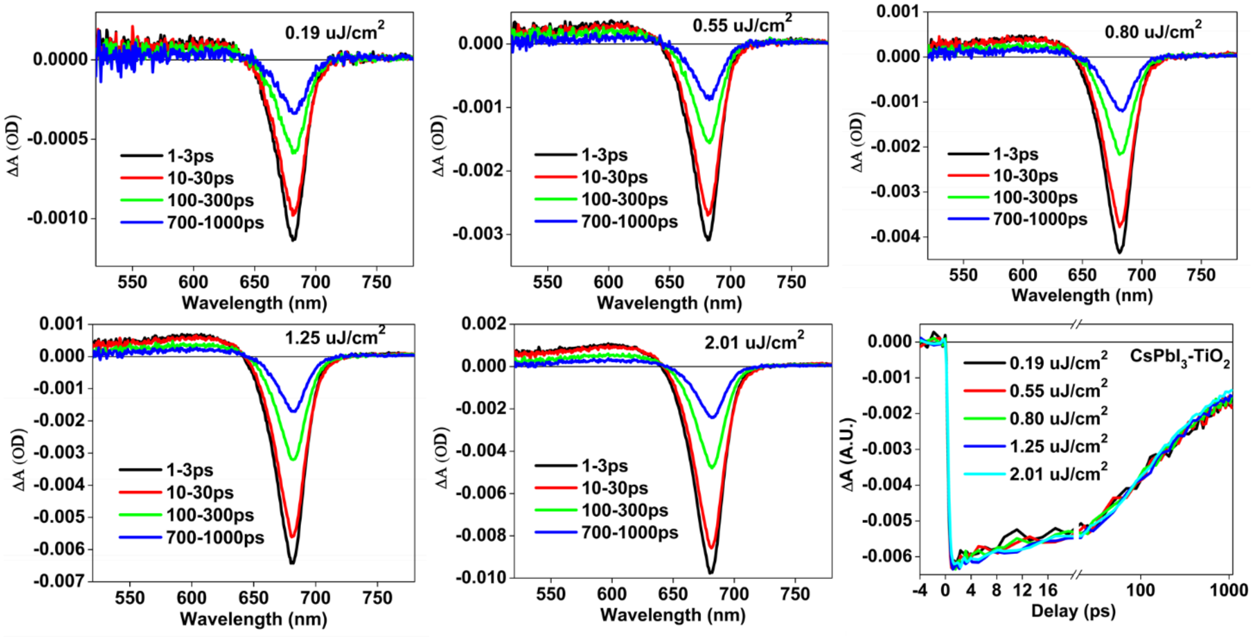

Figure A.6.3. TA spectra of CsPbI$_3$ QDs on TiO$_2$ NP film measured at different excitation densities. The right bottom panel compares the XB recovery kinetics at different excitation densities.

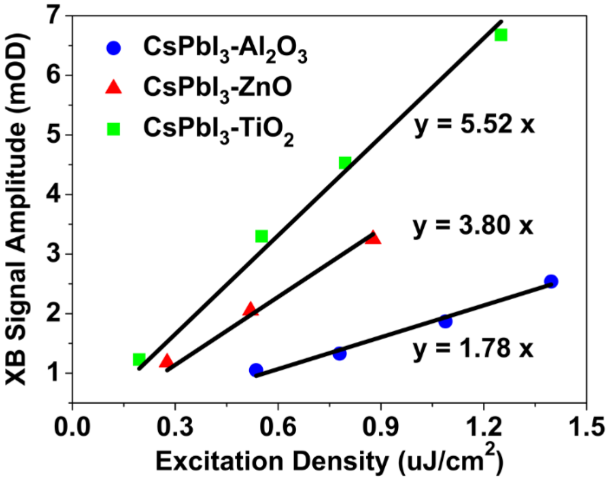

Figure A.6.4. Linear dependence of XB signal amplitudes on excitation densities within single exciton region. The different slopes for three film samples are due to the optical density differences of QDs (Figure 2.5).

Appendix 2. XB kinetics fitting in QD-Metal oxide NP films

To extract ET rate constants, we used following models to fit the XB kinetics.

First, we used equation A.6.1 to fit the XB kinetics of QDs on Al_2O_3 NP film and equation A.6.2 to fit the XB kinetics of QDs on ZnO and TiO_2 NP films. The additional component in the latter samples is for better fitting since ET processes are involved. Fitting results are listed in Table A.6.1.

$$XB(t) = A \cdot [\sum_{i=1}^{3} a_i \cdot e^{-t/\tau_i} - e^{-t/\tau_f}] \qquad (A.6.1)$$

$$XB(t) = A \cdot [\sum_{i=1}^{4} a_i \cdot e^{-t/\tau_i} - e^{-t/\tau_f}] \qquad (A.6.2)$$

In equation A.6.2, a_2 is constrained to be 50% because of the approximate half contribution of electron state filling to the XB feature.

Table A.6.1. Fitting parameters for XB kinetics in $CsPbI_3$ QD-Metal oxide NP films

	τ_f/fs	τ_1/**ps** (a_1)	τ_2/**ps** (a_2)	τ_3 /**ps** (a_3)	τ_3 /**ps** (a_3)
QD-Al_2O_3	224	4.0 (6.0%)	-	2492.5 (81.6%)	200490 (12.4%)
QD-ZnO	211	4.0 (6.0%)	702.7 (50.0%)	4444.4 (35.5%)	524472 (8.5%)
QD-TiO_2	216	4.0 (6.0%)	102.4 (50.0%)	1607.7 (37.2%)	323739 (6.8%)

Subtracting the exciton recombination rate (inverse of 2492.5 ps) from the rate constants involving ET (inverse of 702.7 and 102.4 ps, respectively),[93] we obtain pure ET time constants of 978.6 ps and 106.8 ps for $CsPbI_3$-ZnO and $CsPbI_3$-TiO_2, respectively.

From above fitting results, we know the ET rate from QD to ZnO is not fast enough so that a significant portion of electron will recombine with hole instead of transferring to ZnO. To extract the ET rates in a more physically meaningful way, we derive the following second model to fit the kinetics.

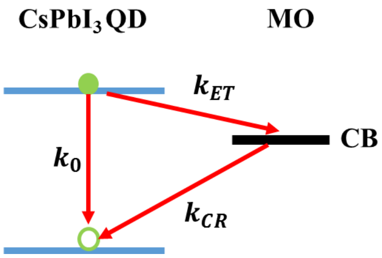

Figure A.6.5. The charge transfer and recombination processes in $CsPbI_3$ QD-MO NP films.

As shown in Figure A.6.5, after excitation, there exist three states in QD-MO pairs: excited state (E), charge transfer state (CT) and ground state (G), which are related to the population of excited state electron and hole. The step-by-step derivation has been written in Chapter 4, Appendix 2. The electron and hole populations can be expressed as:

$$[e] = [E] = N_0\, exp[-(k_0 + k_{ET})t] \qquad \text{(A.6.3),}$$

$$[h] = N_0 \frac{k_0 - k_{CR}}{k_0 + k_{ET} - k_{CR}} \exp[-(k_0 + k_{ET})t] + N_0 \frac{k_{ET}}{k_0 + k_{ET} - k_{CR}} \exp(-k_{CR}t) \qquad \text{(A.6.4).}$$

Considering the electron and hole contributions to the XB signal, the XB decay kinetics can be expressed as:

$$XB(t) = -(0.516[e] + 0.484[h]) = -N_0 \Big\{0.516\, exp[-(k_0 + k_{ET})t] +$$

$$0.484 \left[\frac{k_0 - k_{CR}}{k_0 + k_{ET} - k_{CR}} \exp[-(k_0 + k_{ET})t] + \frac{k_{ET}}{k_0 + k_{ET} - k_{CR}} \exp(-k_{CR}t)\right]\Big\} \qquad \text{(A.6.5).}$$

The XB recovery in QD-Al_2O_3 does not involve ET and CR. The three exponential decay components (equation A.6.1 and Table A.6.1) should be considered as competing processes in QD-ZnO and QD-TiO_2. Thus, the XB kinetics in QD-ZnO and QD-TiO_2 can be written as,

$$XB(t) = -\sum_{i=1}^{3} a_i \cdot \Big\{0.516\, exp[-(k_{i0}+k_{ET})t] + 0.484\Big[\frac{k_{i0}-k_{CR}}{k_{i0}+k_{ET}-k_{CR}}\exp[-(k_{i0}+k_{ET})t] + \frac{k_{ET}}{k_{i0}+k_{ET}-k_{CR}}\exp(-k_{CR}t)\Big]\Big\} \qquad \text{(A.6.6),}$$

where $\sum_{i=1}^{3} a_i \cdot e^{-k_{i0}t} = \sum_{i=1}^{3} a_i \cdot e^{-t/\tau_i}$ were obtained from the three exponential decay fitting (equation A.6.1 and Table A.6.1).

By preliminary fitting, we found that one component of ET and CR is not enough for fitting the XB kinetics well. The reason might be the inhomogeneity of QDs leading to different ET, CR rates. Thus, we added another component and used equation A.6.7 to fit the XB kinetics in QD-ZnO and QD-TiO$_2$:

$$\begin{aligned} XB(t) = -\sum_{i=1}^{3} a_i \cdot \{b \cdot \Big\{0.516\, exp[-(k_{i0}+k_{ET1})t] + 0.484\Big[b\cdot\frac{k_{i0}-k_{CR1}}{k_{i0}+k_{ET1}-k_{CR1}}\exp[-(k_{i0} + \\ k_{ET1})t] + b\cdot\frac{k_{ET1}}{k_{i0}+k_{ET1}-k_{CR1}}\exp(-k_{CR1}t) + (1-b)\cdot\frac{k_{i0}-k_{CR2}}{k_{i0}+k_{ET1}-k_{CR2}}\exp[-(k_{i0}+k_{ET1})t] + \\ (1-b)\cdot\frac{k_{ET1}}{k_{i0}+k_{ET1}-k_{CR2}}\exp(-k_{CR2}t)\Big]\Big\} + (1-b)\cdot\Big\{0.516\, exp[-(k_{i0}+k_{ET2})t] + \\ 0.484\Big[b\cdot\frac{k_{i0}-k_{CR1}}{k_{i0}+k_{ET2}-k_{CR1}}\exp[-(k_{i0}+k_{ET2})t] + b\cdot\frac{k_{ET2}}{k_{i0}+k_{ET2}-k_{CR1}}\exp(-k_{CR1}t) + (1-b)\cdot \\ \frac{k_{i0}-k_{CR2}}{k_{i0}+k_{ET2}-k_{CR2}}\exp[-(k_{i0}+k_{ET2})t] + (1-b)\cdot\frac{k_{ET2}}{k_{i0}+k_{ET2}-k_{CR2}}\exp(-k_{CR2}t)\Big]\Big\}\} \qquad \text{(A.6.7),} \end{aligned}$$

where b is the fraction of QDs contributing to k_{ET1} and k_{CR1}, and (1-b) is the proportion of QDs contributing to k_{ET2} and k_{CR2}. Using k_{ET1}, k_{ET2}, k_{CR1}, k_{CR2}, and b as variable parameters, fitting results by equation A.6.7 are plotted in Figure A.6.6 and listed in Table A.6.2.

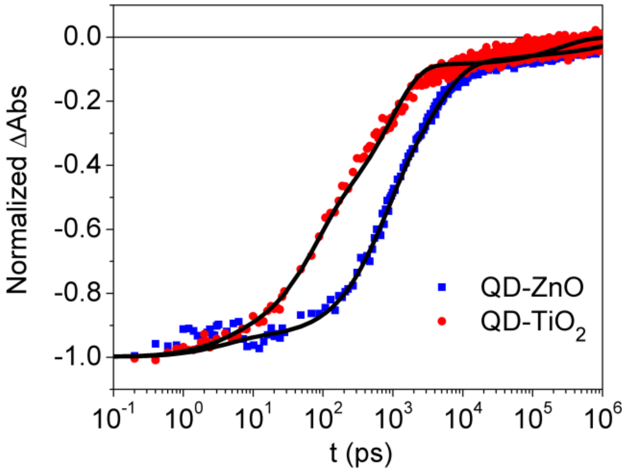

Figure A.6.6. XB recovery kinetics of QDs on ZnO and TiO$_2$ NP films. Black solid lines are fits by equation A.6.7.

Table A.6.2. Fitting parameters for XB kinetics in CsPbI$_3$ QD-MO NP films by A.6.7

	$k_{ET1}\ (ns^{-1})$	$k_{ET2}\ (ns^{-1})$	$k_{CR1}\ (ns^{-1})$	$k_{CR2}\ (ns^{-1})$	b
QD-ZnO	1.2 ± 0.1	0.017 ± 0.002	0.20 ± 0.02	$(7.7 \pm 1.8) \times 10^{-4}$	$(79.9 \pm 1.7)\%$
QD-TiO$_2$	14 ± 1	1.25 ± 0.08	1.11 ± 0.06	$(4.0 \pm 0.9) \times 10^{-3}$	$(81.3 \pm 1.5)\%$

From above, we have ET and CR rate constants, the inverse of which are time constants listed below (Table A.6.3) and we use these values in the main text. Based on the ET rate constants, exciton trapping and recombination rate constants obtained above, we calculated the efficiencies of ET. The results are listed in Table A.6.4.

Table A.6.3. Time constants of ET and CR in $CsPbI_3$ QD-MO NP films

	$\tau_{ET1}/\mathbf{ns}$	$\tau_{ET2}/\mathbf{ns}$	$\tau_{CR1}/\mathbf{ns}$ (a_1)	$\tau_{CR2}/\mathbf{ns}$ (a_2)
QD-ZnO	0.85 ± 0.05 (79.9%)	60 ± 7 (20.1%)	5.0 ± 0.5 (79.9%)	1300 ± 400 (20.1%)
QD-TiO_2	0.070 ± 0.007 (81.3%)	0.80 ± 0.05 (18.7%)	0.90 ± 0.05 (81.3%)	250 ± 60 (18.7%)

Table A.6.4. ET efficiencies

	ET efficiency 1 (~80%)	ET efficiency 2 (~20%)	Overall ET efficiency
QD-ZnO	73.5%	12.9%	61.3%
QD-TiO_2	92.1%	74.2%	88.7%

Appendix 3. PL decay kinetics fitting

PL decay reflects the decay of excited state. Based on equation A.6.3, the PL decay rates should be the sum of exciton recombination and ET (equation A.6.8).

$$PL(t) = PL(0)\, exp[-(k_0 + k_{ET})t] \qquad \text{(A.6.8).}$$

Since there are two different ET components from XB kinetics, the PL decay should also have two components. Indeed, we can fit the PL kinetics with bi-exponential decay function convoluted with IRF.

$$PL(t) = \sum_{i=1}^{2} a_i \cdot e^{-t/\tau_i} \otimes IRF \qquad \text{(A.6.9),}$$

where a_i and τ_i are the amplitude and time constant of bi-exponentials. Fitting results are plotted in Figure A.6.7 and parameters are listed in Table A.6.5. PL decay fitting results are consistent with ET rate constants obtained in XB kinetics fitting, thus confirming that two batches of QDs contribute to different ET rates.

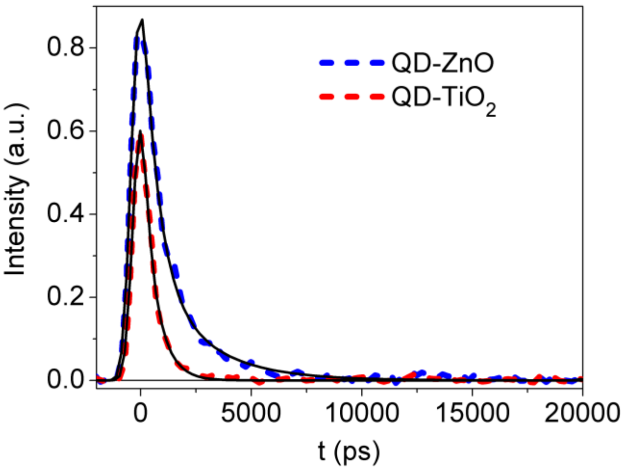

Figure A.6.7. Scaled PL decay curves of QDs on ZnO and TiO$_2$ NP films. Black solid lines are bi-exponential decay fits.

Table A.6.5. Bi-exponential decay fitting parameters for PL kinetics

	$\tau_1/\mathbf{ps}$ (a_1)	$\tau_2/\mathbf{ps}$ (a_2)
QD-ZnO	650 ± 30 $(78.3 \pm 2.2)\%$	2400 ± 130 $(21.7 \pm 2.2)\%$
QD-TiO_2	67.6 ± 0.4 $(79.8 \pm 0.9)\%$	624 ± 20 $(20.2 \pm 0.9)\%$

Chapter 7. Charge transfer study on $CsPbI_3$ QD-TiO_2 films and the influence of different post-synthesis treatments

7.1. Introduction

Organic-inorganic hybrid lead halide perovskite photovoltaic devices have attracted tremendous attention with quick power conversion efficiencies upsurge in recent years, exceeding 23%.[108, 112] However, the low stability of organic-inorganic hybrid perovskite materials limits their commercial implementation.[108, 113-115] Incorporating inorganic cations (Cs^+ or Rb^+)[4-6] to form all-inorganic $CsPbI_3$ perovskites[7-9] can improve device stability. The cubic phase of $CsPbI_3$ can be stabilized at room temperature in quantum dot (QD) form for months, and the efficiency of $CsPbI_3$ QD solar cells (13.43%)[12] can exceed that of non-perovskite QD solar cells, suggesting great promise for perovskite QD based solar cell technology.[89, 108]

As mentioned in the last chapter, the overall solar to electricity conversion process of perovskite QD solar cells involves many elementary processes, such as carrier transport within the QD film, carrier transfer at the interface charge carrier extraction layers and competing charge recombination processes. Understanding these processes is important to the rational improvement of device performance. In recent reports of $CsPbI_3$ QD photovoltaic devices, a post-synthesis purification method using methyl acetate (MeOAc) as anti-solvent to precipitate QDs was found to improve the device performance,[7, 12] compared to devices prepared with QDs purified with direct precipitation method.[46] It was reported that after washing by MeOAc for twice, most surface ligands on QDs are removed.[7] These findings may suggest the important role of QD surface ligand density on the overall device performance. The organic surface ligands may lower the charge transport between QD and slow down interfacial charge transfer between QDs and electron and hole accepting layers.

During our working on this project, two reports are published about electron transfer from inorganic perovskite nanocrystals to TiO_2 mesoporous films.[116-117] Feng Liu et al. studied size dependent electron transfer from $CsPbI_3$ QDs to TiO_2 films with injection efficiency close to 99% and they used this system to fabricate a QD-sensitized solar cell with a power conversion efficiency of 5%.[116] In this study, $CsPbI_3$ QDs are purified with MeOAc washing once. The influences of ligand quantity and purification methods on electron transfer rates are not considered. Also, they only observed charge separation but did not observe charge recombination process in the transient absorption study. Prashant Kamat's group reported charge transfer between $CsPbBr_3$ nanocrystals and TiO_2 and their observation of the degradation of $CsPbBr_3$ nanocrystals induced by the charge transfer.[117] Similarly, they have not considered the influence of ligands and did not observe the charge recombination process in the study, which are important aspects of the charge carrier dynamics.

In this chapter, we study the effect of post-synthesis treatment of QDs on the interfacial electron transfer (ET), or charge separation (CS), and charge recombination (CR) dynamics between $CsPbI_3$ perovskite QDs and TiO_2 nanoparticle (NP) films (see Eq. 7.1 and Scheme 7.1).

$$\mathrm{CsPbI_3(e-h) + TiO_2 \overset{CS}{\rightarrow} CsPbI_3(h) + TiO_2(e) \overset{CR}{\rightarrow} CsPbI_3 + TiO_2} \quad (7.1)$$

By transient absorption (TA) spectroscopy and time-resolved PL decay measurement, we observed that QDs washed with MeOAc, compared with QDs purified with direct precipitation decrease the CS constant from 457 ± 4 ps and 288 ± 1 ps at $\mathrm{QD/TiO_2}$ interface, increase the CS efficiency from 89.9 ± 0.3% to 98.3 ± 0.01%, and increase the average CR time constant from 346 ± 18 ns to 1180 ± 60 ns. Fourier tranform infrared (FTIR) spectrocopy measurements reveal that different amounts of ligands in the films might be a possible factor influencing the ET rates. These results suggest the necessity to purify the QDs with MeOAc washing to benefit the performance of $CsPbI_3$ QD solar cells.

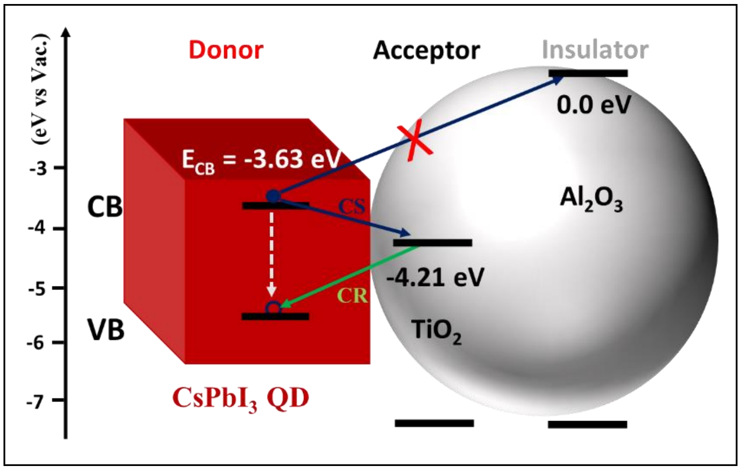

Scheme 7.1. Schematic energy level diagram and charge separation and recombination pathways at the $CsPbI_3$ QD/TiO_2 NP interface: conduction band (CB) and valence band (VB) edges in $CsPbI_3$, TiO_2 and Al_2O_3 (black horizontal solid lines), charge separation (CS) from QD to TiO_2 (dark blue arrows), charge recombination (CR) process (green arrow), and electron-hole recombination inside the QD (dashed grey arrow).

7.2. Results and discussion

7.2.1. Sample characterizations

$CsPbI_3$ QDs were synthesized according to a published hot injection method (Chapter 2).[7, 19-20, 46] Two batches of QDs with different ligand coverage were obtained through different post-synthesis treatments, denoted as QD original and QD washed in the figures, respectively. The absorption and emission spectra of both $CsPbI_3$ QDs in heptane (Figure 7.1a and 7.1d) show band gaps at ~1.81 eV and broad absorption across most of the visible spectrum. The photoluminescence quantum yields (PL QY 24.2% and 21.7% for QD original and QD washed, respectively) and PL decay kinetics (Figure 7.1e) vary only slightly for these two batches of QDs. Consistent with previous reports,[7, 19-20, 46, 59, 100] these QDs have a cubic crystal phase and exhibit cuboidal shapes in TEM images (Figure 7.1b and 7.1c) with average edge lengths of 13.5 ± 2.7 nm and 14.3±3.3 nm, for the original and washed QDs, respectively. Figure 7.1f shows a comparison of normalized infrared (IR) absorption spectra of QDs spin-coated on sapphire windows prepared with the original and washed QDs. The normalization factors are determine by their absorbance at 680 nm, such that the normalized IR spectra correspond to the same amount of QDs on the films. The film prepared from the washed QDs shows lower IR absorbance in the CH stretching mode region,[7] indicating lower ligand coverage in these films.

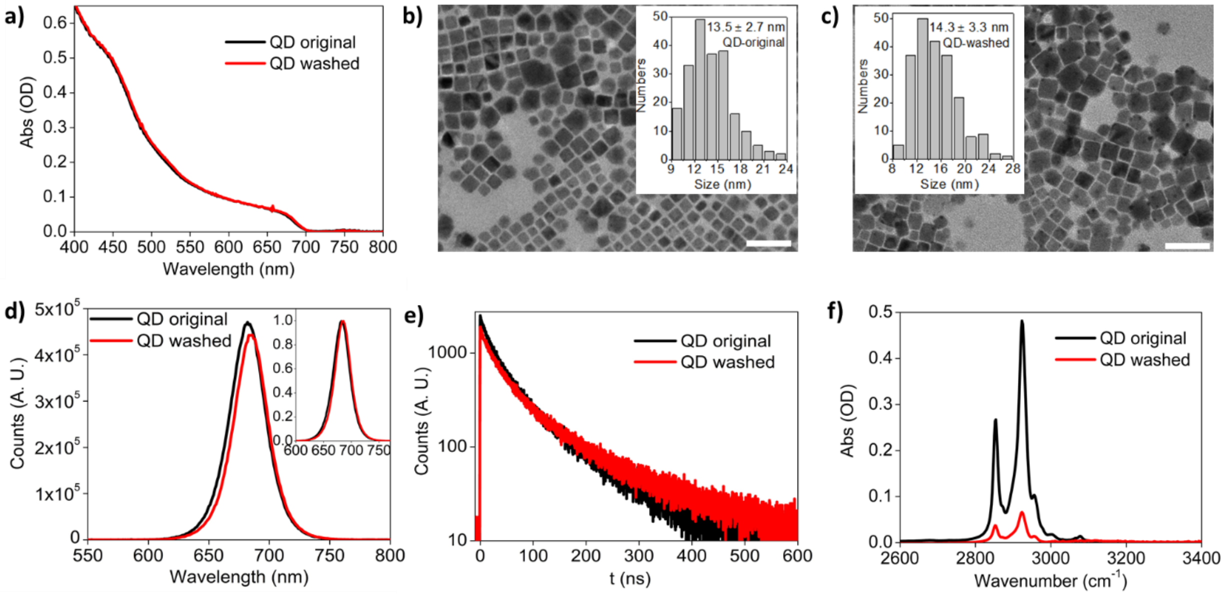

Figure 7.1. Spectroscopic and TEM characterization of QDs. a) UV-vis absorption spectra of original QDs and washed QDs in hexane. b) and c) TEM images of original QDs and washed QDs. Scale bar: 50 nm. Insets are size distribution statistics. d) PL spectra of QD solutions in a). Inset is the normalized spectra. e) PL decay kinetics of QD solutions in a), excited at 490 nm. f) FTIR spectra of original QDs and washed QDs spin-coated on the sapphire windows. The amplitudes have been corrected with QD absorption at 680 nm to compare the ligand quantity on QDs.

TiO_2 nanocrystalline thin films were fabricated by doctor-blading colloidal dispersions (NP diameter 30 nm) onto sapphire substrates and annealing at 450 ℃ for 1h.[25, 57-58, 105] TiO_2 films coated with ~1.3 nm Al_2O_3 films via atomic layer deposition (ALD) were used as control systems, in which the higher CB band edge of Al_2O_3 prevents electron injection.[45, 91] These films are referred to as ALD TiO_2 hereafter. The TiO_2 and ALD TiO_2 films were immersed in concentrated $CsPbI_3$ QDs solution for 48 h,[25] followed by a heptane rinse to remove weakly adsorbed QDs on the films. Adsorption of QDs on these films were confirmed by photographs (Figure 7.2 insets) and UV/vis absorption spectra (Figure 7.3) of QD-TiO_2 and QD-ALD TiO_2 films. Fourier transform IR spectra were measured to determine the ligand absorption on the films (Figure 7.2). FTIR absorption value at 2925 cm^{-1} divided by visible absorption value at 680 nm (IR/Vis) was used as the measure of total ligand quantity relative to the QD quantity on QD/TiO_2 films because the IR absorption amplitudes and visible absorption amplitudes were proportional to the quantity of ligands and the number of QDs, respectively. Note that here IR/Vis ratio cannot be considered as the ligand coverage of QDs because the ligands can also distribute at the surface of TiO_2 and ALD TiO_2 surfaces (Figure A.7.1). Table 7.1 lists the IR/Vis values on the films. Compared with QDs on the sapphire, QD original suffered significant ligand loss when adsorbed into TiO_2 and ALD TiO_2 films. However, both the QD original-ALD TiO_2 and QD original-TiO_2 had higher IR/Vis values than the QD washed-ALD TiO_2 and QD washed TiO_2, respectively, as shown in Figure 7.2 and Table 7.1.

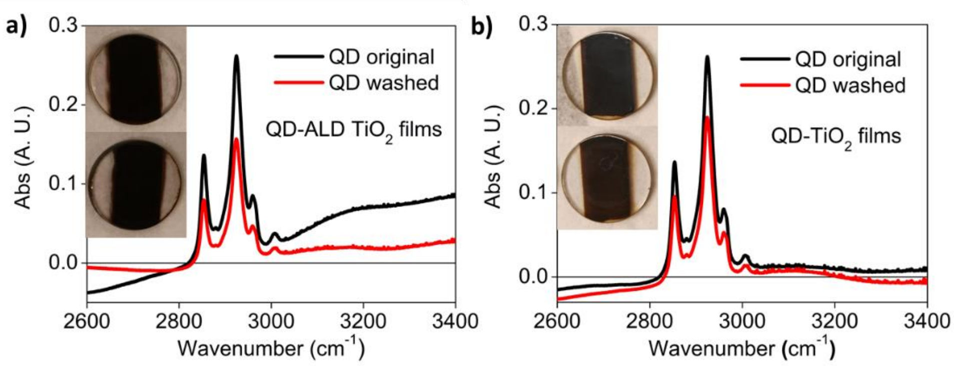

Figure 7.2. FTIR spectra of QDs on a) ALD TiO$_2$ and b) TiO$_2$ films prepared with (QD washed) and without (QD original) post-synthesis MeOAc wash of QDs. The amplitudes have been scaled with QD absorption at 680 nm to compare the relative ligand quantities. Insets are photos of the QD sensitized films.

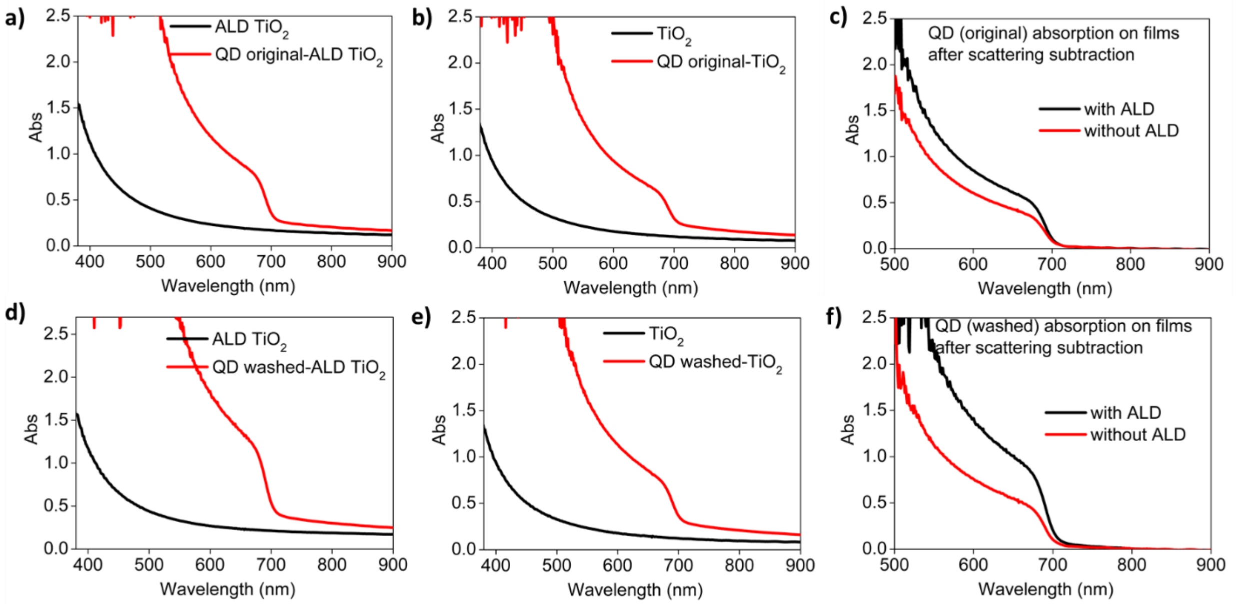

Figure 7.3. a), b), d) and e) UV-vis absorption of films before and after QD adsorption. c) and f) Absorption spectra of QDs on the film after scattering subtraction.

Table 7.1. IR/Vis values of films determined by FTIR and UV-vis absorption

Films	Abs @ 680nm	IR @ 2925cm^{-1}	IR/Vis
QD original-sapphire	0.117	0.482	4.120
QD original-ALD TiO_2	0.441	0.262	0.594
QD original-TiO_2	0.309	0.262	0.848
QD washed-sapphire	0.092	0.052	0.565
QD washed-ALD TiO_2	0.731	0.260	0.356
QD washed-TiO_2	0.385	0.237	0.616

7.2.2. TA study on QD-TiO_2 films

Ultrafast TA spectroscopy measurements were conducted to investigate the CS and CR processes. The details of TA setups are presented in Chapter 2. Briefly, a 500 nm pump pulse was focused to excite the QDs, and an overlapped white light continuum probe pulse was used to detect the absorbance change (ΔA) as a function of pump-probe delay time. Figure 7.4a, b, d and e show the TA spectra of $CsPbI_3$ QDs on ALD TiO_2 and TiO_2 films. The TA spectra are dominated by an exciton bleach (XB) feature peaked at ~680 nm, caused by the state filling of the CB electron and VB hole at the band edges.[31] The recovery of XB signal can be used to follow the electron and hole dynamics. The electron and hole contributions to the XB signal are about half and half as discussed in Chapter 4 and Chapter 6. Note that the electron and hole contributions to XB feature may vary due to sample variations. For the original QDs and washed QDs in solution, the electron contributions are measured to be 53.1% and 57.2%, respectively (Appendix 2).

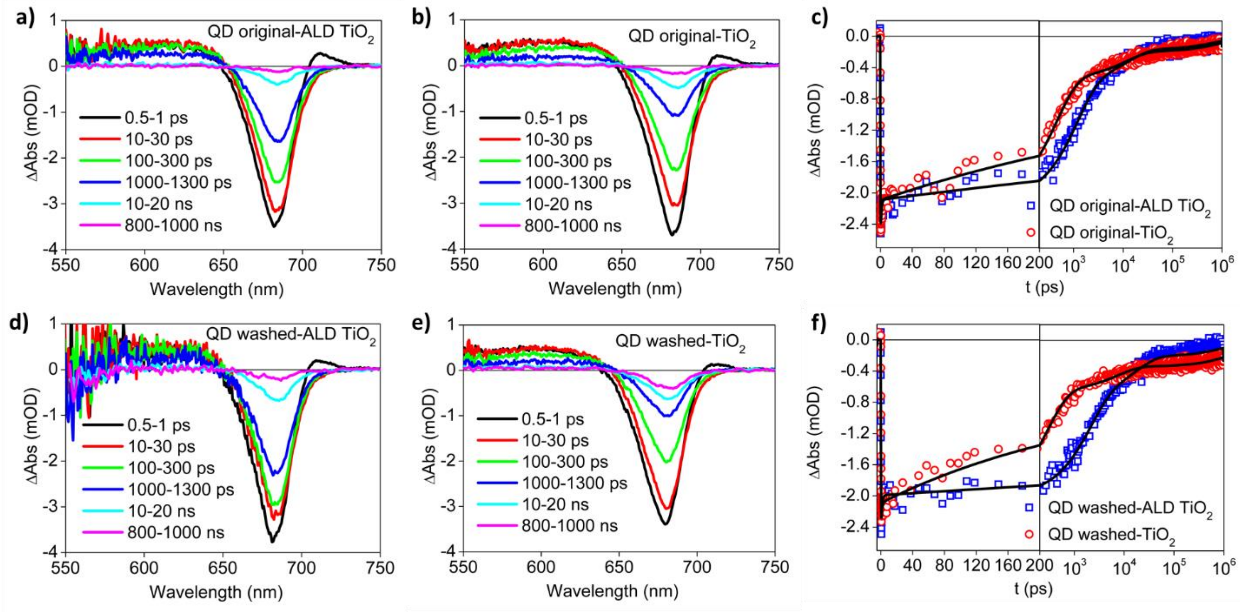

Figure 7.4. TA spectra and kinetics of $CsPbI_3$ perovskite QDs on metal oxide films measured with 500 nm excitation. TA spectra of original QDs on (a) ALD TiO_2 and (b) TiO_2 films at indicated time delays after 500 nm excitation. c) Comparison of XB recovery kinetics of original QDs on ALD TiO_2 (blue squares) and TiO_2 (red circles) films. TA spectra of washed QDs on (d) ALD TiO_2 (d) and (e) TiO_2 films at indicated time delays after 500 nm excitation. f) Comparison of XB recovery kinetics of washed QDs on ALD TiO_2 (blue squares) and TiO_2 (red circles) NP films. Black solid lines are multi-exponential fits according to the model provided in Appendix 3.

The QD XB recovery kinetics on ALD TiO_2 and TiO_2 films are compared in Figure 7.4c and f for original and washed QDs, respectively. Compared to QDs on ALD TiO_2, the XB decay of QDs on TiO_2 shows a faster decay on the < 10 ns time scale and a slower decay on the >10 ns time scale. This is consistent with a fast electron decay (by electron transfer to TiO_2) and slow hole decay (by charge recombination with the transferred electron in TiO_2).

7.2.3. Analysis of PL decay and XB kinetics

To further confirm the above assignment, time-resolved photoluminescence (PL) decay kinetics were measured for the same samples. As shown in Figure 7.5a and d, the PL decays are accelerated with the appearance of TiO_2 instead of ALD TiO_2 because of the rise of additional ET process, whose trends are consistent with those of XB recovery. As mentioned in Chapter 6, PL decay probes the exciton (e-h pair) dynamics, complete decay of the CB electron (or VB hole) by any pathways (e-h recombination, electron trapping or ET to TiO_2) leads to a complete PL decay. XB bleach probes the sum of electron and hole population and complete decay of CB electron by ET to TiO_2 only leads to a partial decay of XB signal (with the hole contribution remaining). Therefore, it is informative to compare the PL decay and XB bleach kinetics (Figure 7.5b, c and e, f), although the PL decay curves miss data points at short delay time (<10 ps) due to its lower time resolution. For QDs on ALD TiO_2 (Figure 7.5b and e) the PL decay and XB kinetics match well with each other, indicating that electron-hole recombination dominates the excited state decay, consistent with the expected lack of interfacial electron transfer in this sample.

For QDs on TiO_2 films (Figure 7.5c and f), PL decays completely by ~ 1 ns, much faster than that for QDs on ALD TiO_2, suggesting the quenching of QD excitons by ET to TiO_2. Furthermore, a normalized comparison of XB bleach and PL decay shows that PL decay and XB decay agrees with each other at < 1 ns (Figure A.7.4), and there exist slow XB recovery components at > 1 ns (Figure 7.5c and f). These results are consistent with ET from QD to oxides, which leads to complete (and fast) PL decay and the formation of a charge separated state. In the charge separate state, the VB hole remaining in the QD is responsible for the longer lived XB signal, the decay of which can be used to follow the charge recombination process (Scheme 1).

Based on above analysis, we used a multi-exponential fitting model to extract the charge separation and charge recombination time constants. Details are provided in Appendix 3. Briefly, we fit the PL decays in QD-ALD TiO_2 films and QD-TiO_2 films to extract the CS time constants. The CS time constants are calculated to be 457 ± 4 ps and 288 ± 1 ps in QD original-TiO_2 and QD washed-TiO_2 films, respectively (Table A.7.3). The corresponding CS efficiencies are $89.9 \pm 0.3\%$ and $98.3 \pm 0.01\%$. Averaging the long components in XB recovery kinetics with corresponding amplitudes (Table A.7.4), we obtained the average charge recombination time constants are 346 ± 18 ns and 1180 ± 60 ns in QD original-TiO_2 and QD washed-TiO_2 films, respectively.

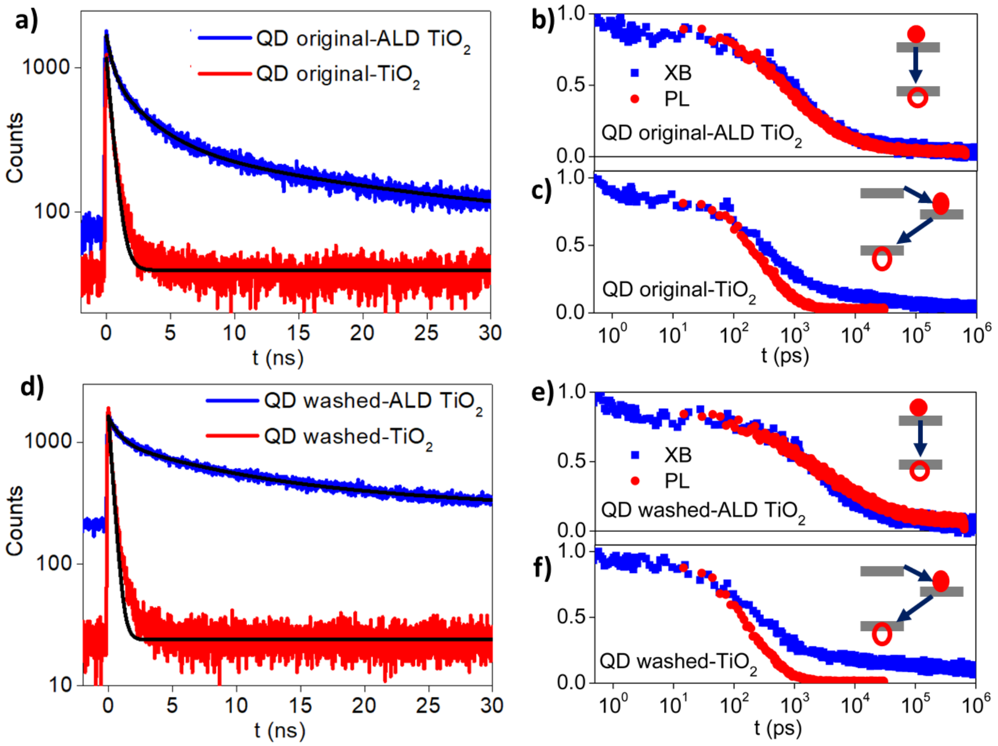

Figure 7.5. PL decay kinetics of $CsPbI_3$ QDs on NP films. a) and d) Comparison of PL decay on ALD TiO_2 and TiO_2. Black solid lines are fitting of PL decays described in Appendix 3. b), c) and e), f) Comparison of PL decay (red) and XB kinetics (blue) of QDs on NP films. Insets are the dominant processes in each film: exciton recombination or electron transfer and charge recombination.

In addition to the electron transfer process, different ligand quantity per QD may also influence the XB decay and PL decay rates. To quantify this factor, we plotted the PL decay rate versus IR/Vis value in Figure 7.6. As indicated by the red line in the figure, average PL decay rates vary with IR/Vis value slightly, whereas the decay rates of QDs on TiO_2 films (blue stars) are far above the red line, indicating the differences of PL decay rates between QD-TiO_2 and QD-ALD TiO_2 (Figure 7.5a and d) are mainly caused by ET, not by the ligand quantity per QD.

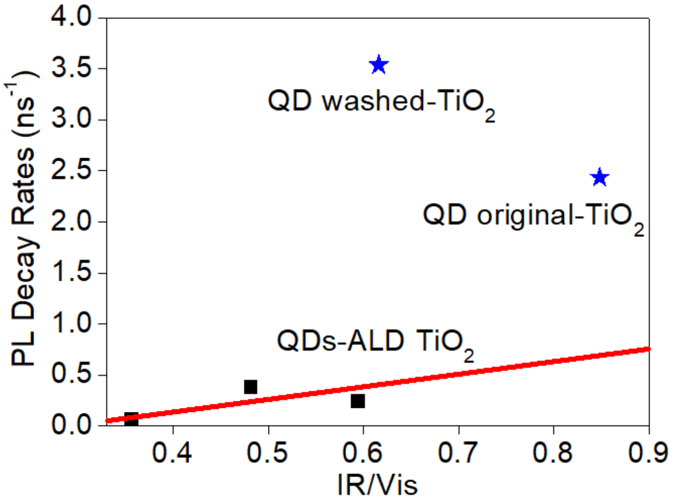

Figure 7.6. The influence of ligand quantity per QD (IR/Vis) on PL decay rates (Data adopted from Table A.7.3). Average PL decay rates vary with IR/Vis value slightly (red line). PL decay rates of QDs on TiO_2 films (blue stars) are far above the red line, indicating the existence of electron transfer process.

7.2.4. Implications on perovskite QD devices

In Chapter 6, we infer that ligands on the QD surfaces may slow the charge transfer rates through reducing the electronic coupling strength with the TiO_2 electron extraction layer.[111] Our study herein shows that: (1) ligands do exist in QD-TiO_2 films in both original and washed QD cases and (2) the higher IR/Vis value (ligand quantity per QD in films) might be one reason for these lower ET rates. With ~27% IR/Vis value decreasing, the CS rate increases and CS efficiency increases by 8.4%. Also, the charge recombination time is much longer in the lower QD-TiO_2 sample (1180 ± 60 ns) with lower IR/Vis value than that in the higher sample (346 ± 18 ns), suggesting less recombination loss in the former. Since we cannot measure the ligand quantity at the QD/TiO_2 interfaces, the influence of ligand quantity on ET and CR processes is inconclusive in this study. The comparison between washed QD and original QD indicates that purifying $CsPbI_3$ QDs with methyl acetate is necessary and beneficial for fabricating high efficiency solar cells. However, we cannot deprive all the ligands from QD surfaces because QDs suffered severe aggregation and degradation with further anti-solvent washing. More efforts are required to address this stability problem to make $CsPbI_3$ QDs industrially applicable.

7.3. Conclusion

In conclusion, we have investigated interfacial charge separation and charge recombination kinetics at all-inorganic $CsPbI_3$ perovskite QDs/TiO_2 nanoparticle interface and the influence of post-synthesis treatment by FTIR, TA and PL decay measurements. Although original QDs lost most ligands during adsorption into the TiO_2 films, the remaining ligand quantity per QD was still larger than the washed ones, which might slow down the CS rate. With ~27% lower IR/Vis value, CS time constant decreases from 457 ± 4 ps (QD original-TiO_2) to 288 ± 1 ps in QD washed-TiO_2 films and CS efficiency increases from 89.9 ± 0.3 % to 98.3 ± 0.01 %. Plus, the average charge recombination time constants are 346 ± 18 ns and 1180 ± 60 ns in QD original-TiO_2 and QD washed-TiO_2 films, respectively. MeOAc washed QDs have faster CS rate and slower charge recombination rate, which could benefit the solar cell performance with higher CS efficiency and less recombination loss.

Appendix 1. FTIR of films adsorbed with ligands

Blank TiO_2 and ALD TiO_2 films were soaked in dilute ligand (OAm and OA) solution (OA: OAm: Hexane = 1: 1: 32 (volume ratio)) for 42 h and rinsed with hexane. FTIR were measured to see whether ligands can be adsorbed onto the films. Figure A.7.1 shows that the films did adsorb ligands. Since the ligands on perovskite QD surfaces are flexible to detach, in QD-TiO_2 and QD-ALD TiO_2 films, the ligands can distribute on both QD surfaces and TiO_2 surfaces.

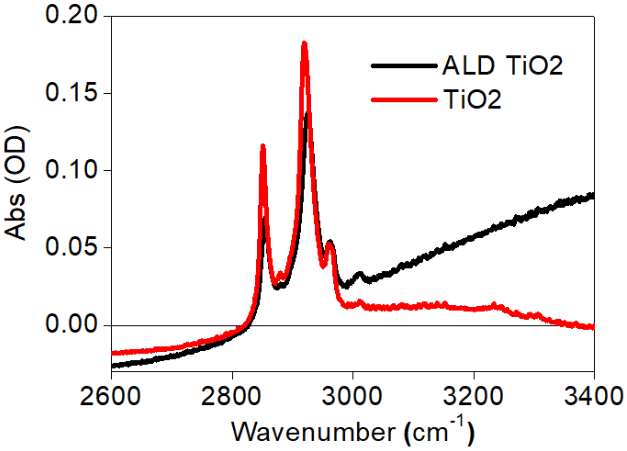

Figure A.7.1. FTIR spectra of films after soaking in dilute ligand solution for 42 h.

Appendix 2. Electron and hole contribution to XB

We conducted TA measurements to the free QDs and QD-RhB complexes for both original QDs and washed QDs. Figure A.7.2 shows the results of original QDs. According to the multiexponential fitting parameters of XB kinetics (Table A.7.1), the electron and hole contributions to the XB feature of original QDs are 53.1% and 46.9%. Figure A.7.3 shows the results of washed QDs. According to the fitting parameters of XB kinetics (Table A.7.2), the electron and hole contributions to the XB feature of washed QDs are 57.2% and 42.8%. The differences are due to sample variations.

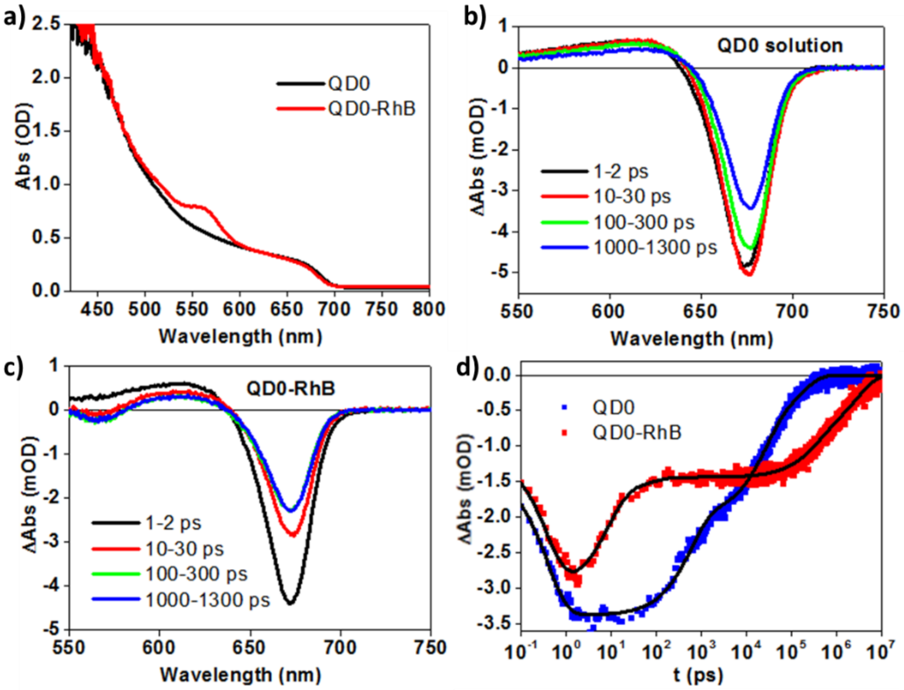

Figure A.7.2. TA study of free original QDs and QD-RhB complexes in solution. a) Absorption spectra of free original QDs and QD-RhB complexes. b) TA spectra of free original QDs measured with 500 nm pump at indicated delay time. c) TA spectra of original QD-RhB complexes measured at the same conditions as the free QDs. d) XB kinetics of original QDs and QD-RhB complexes. Black lines are multiexponential fits.

Table A.7.1. Fitting parameters of XB kinetics in original QDs and QD-RhB complexes

	τ_f/ps	τ_1/**ps** (a_1)	τ_2/**ps** (a_2)	τ_3 /**ns** (a_3)	τ_3 /**ns** (a_3)
Original QD	0.39	587.7 (41.6%)	24539 (37.0%)	164.2 (21.4%)	-
QD-RhB	0.39	8.56 (45.9%)	68.88 (7.2%)	336.9 (18.3%)	2959 (28.6%)

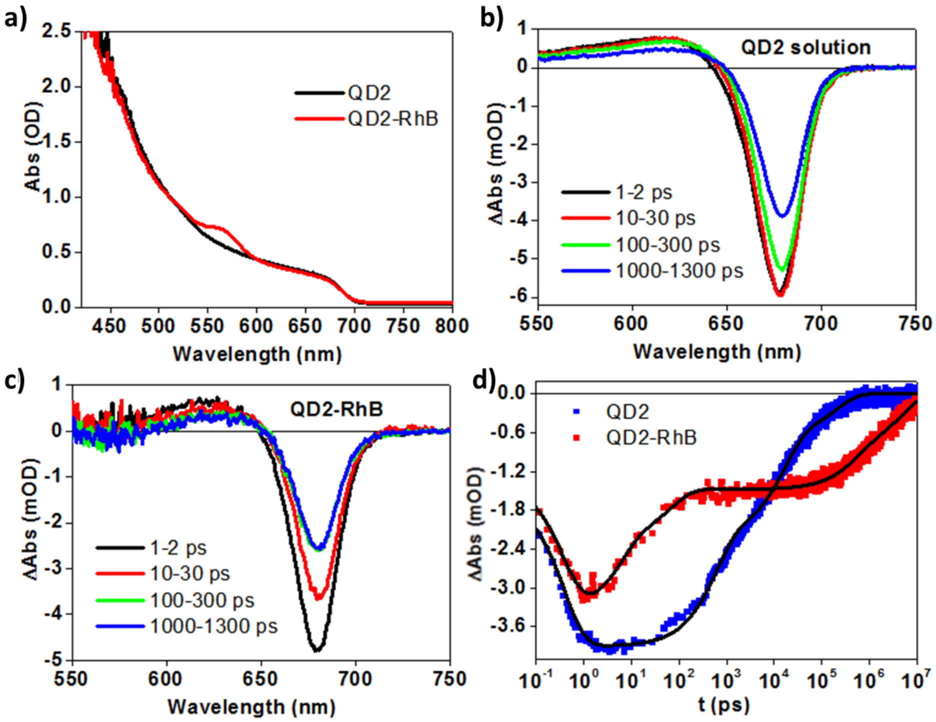

Figure A.7.3. TA study of washed QDs and QD-RhB complexes in solution. a) Absorption spectra of washed QDs and QD-RhB complexes. b) TA spectra of free washed QDs measured with 500 nm pump at indicated delay time. c) TA spectra of washed QD-RhB complexes measured at the same conditions as the free QDs. d) XB kinetics of washed QDs and QD-RhB complexes. Black lines are multiexponential fits.

Table A.7.2. Fitting parameters of XB kinetics in washed QDs and QD-RhB complexes

	τ_f/ps	τ_1/**ps** (a_1)	τ_2/**ps** (a_2)	τ_3 /**ns** (a_3)	τ_3 /**ns** (a_3)
Original QD	0.39	596.3 (43.8%)	16164 (39.3%)	205.8 (16.9%)	-
QD-RhB	0.39	5.97 (34.8%)	69.82 (22.4%)	497.2 (17.7%)	5084 (25.1%)

Appendix 3. XB kinetics and PL decay kinetics fitting in QD-Metal oxide NP films

To extract CS and CR time constants, we fit the XB kinetics and PL decay kinetics by the following model.

For the QD-TiO_2 films, as shown in the main text, PL decay is dominated by the CS process and XB kinetics involves both CS and CR processes. We can scale the PL decay kinetics to match part of the XB kinetics, which can be treated as CS dominant time range. See Figure A.7.4.

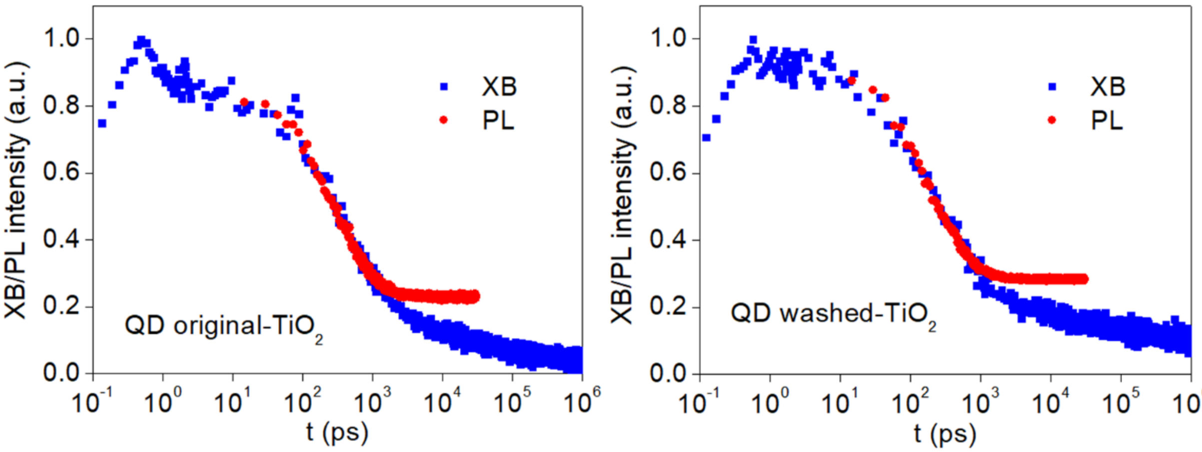

Figure A.7.4. Scaled PL decay curves to match the XB kinetics in QD-TiO_2 films. The matching part of XB kinetics is the CS dominant time range.

First, we can fit the PL decay kinetics to extract CS time constants. PL decays in QD-ALD TiO_2 films are fit with triexponential decay function (S3). PL decays in QD-TiO_2 films are fit with single exponential decay function.

$$PL(t) = \sum_{i=1}^{3} a_i \cdot e^{-t/\tau_i} \qquad \text{(A.7.1)}$$

Fitting parameters are listed in Table A.7.3. By subtracting the PL decay rate of QD-ALD TiO_2 from the PL decay rate of QD-TiO_2, we obtain the CS rate in QD-TiO_2 films. The CS time constants are also listed in Table A.7.3. Using these time constants, we calculated the CS efficiency to be $89.9 \pm 0.3\%$ and $98.3 \pm 0.01\%$ in original QD-TiO_2 film and washed QD-TiO_2 film, respectively.

Table A.7.3. PL decay fitting parameters and CS time constants calculated from PL decays

	τ_1/ns (a_1)	**τ_2/ns (a_2)**	**τ_3/ns (a_3)**	**Average (ns)**	**CS time constant (ns)**
QD0-ALD TiO_2 (original)	0.47 ± 0.01 ($48.0 \pm 0.6\%$)	2.72 ± 0.06 ($37.1 \pm 0.5\%$)	18.80 ± 0.34 ($14.9 \pm 0.3\%$)	4.03 ± 0.08	-
QD0-TiO_2 (original)	0.411 ± 0.002 (100%)	-	-	0.411 ± 0.002	0.457 ± 0.004
QD2-ALD TiO_2 (washed)	0.84 ± 0.02 ($40.6 \pm 0.5\%$)	7.74 ± 0.16 ($39.7 \pm 0.4\%$)	56.27 ± 1.25 ($19.7 \pm 0.4\%$)	14.50 ± 0.32	-
QD2-TiO_2 (washed)	0.283 ± 0.001 (100%)	-	-	0.283 ± 0.001	0.288 ± 0.001
QD1-ALD TiO_2 (washed once)	0.42 ± 0.01 ($47.4 \pm 0.8\%$)	2.07 ± 0.05 ($40.7 \pm 0.7\%$)	12.82 ± 0.25 ($11.9 \pm 0.3\%$)	2.57 ± 0.05	-

Next, we used function A.7.2 to fit the XB kinetics of QD-TiO_2 films by constraining time constant of the second decay component, which has been determined in PL decay fitting. The fitting results are listed in Table A.7.4.

$$XB(t) = A \cdot \left[\sum_{i=1}^{4} a_i \cdot e^{-t/\tau_i} - e^{-t/\tau_f}\right] \qquad \text{(A.7.2)}$$

The second decay component (Table S4) amplitudes a_2 of original QD-TiO_2 and washed QD-TiO_2 are 47.4% and 63.0% respectively, which is consistent with the approximate half contribution of electron state filling to the XB feature. The difference between these values and those in solutions are due to the difference of environments and sample variations. The QDs in films are only part of the QDs in solutions. The adsorbed QDs may deviate from the average property of QDs in solution. Also, QDs in films have obvious trapping process. The contributions of electron and hole to the trapping are unclear and may vary with different samples.

Except the fast trapping and the CS processes, the remaining two slow decay components of XB kinetics in QD-TiO_2 films are attributed the CR process. The average CR time constants are 346 ± 18 ns and 1180 ± 60 ns in QD original-TiO_2 and QD washed-TiO_2 films, respectively, by averaging their long components with amplitudes a_3 and a_4 (Table A.7.4).

Table A.7.4. XB Kinetics fitting in QD-Metal oxide NP films

	τ_f/fs	**τ_1/ps (a_1)**	**τ_2/ps (a_2)**	**τ_3/ns (a_3)**	**τ_4/ns (a_4)**
QD0-ALD TiO_2 (original)	210 ± 21	1.00 ± 0.17 (25.9 ± 7.2%)	1163 ± 35 (53.0 ± 0.9%)	12.5 ± 0.9 (15.2 ± 0.8%)	878 ± 68 (5.9 ± 0.2%)
QD0-TiO_2 (original)	204 ± 21	0.74 ± 0.09 (33.2 ± 6.9%)	410.6 (47.4%)	8.6 ± 0.3 (13.0 ± 0.2%)	1032 ± 53 (6.4 ± 0.1%)
QD2-ALD TiO_2 (washed)	205 ± 22	1.06 ± 0.18 (27.1 ± 6.6%)	1964 ± 84 (45.2 ± 1.1%)	16.5 ± 1.1 (20.0 ± 1.1%)	1296 ± 113 (7.7 ± 0.2%)
QD2-TiO_2 (washed)	165 ± 9	10 ± 2.75 (7.6 ± 0.6%)	282.8 (63.0%)	7.7 ± 0.4 (14.1 ± 0.3%)	2260 ± 114 (15.3 ± 0.1%)
QD1-ALD TiO_2 (washed once)	200 ± 22	0.78 ± 0.12 (34.2 ± 9.1%)	1325 ± 50 (43.5 ± 1.0%)	10.4 ± 0.7 (17.0 ± 1.0%)	928 ± 70 (5.3 ± 0.1%)

Chapter 8. Summary

In summary, we conduct comprehensive studies on charge transfer processes involving $CsPbI_3$ QDs by time-resolved spectroscopy. By measuring ultrafast TA spectroscopy of free QDs and QD-RhB complexes in nonpolar organic solvent, we reveal the unique intrinsic charge carrier properties of $CsPbI_3$ QDs: 1) The electron and the hole both contribute to the XB signal, with amplitudes around half and half; 2) in the family of $CsPbX_3$ (X=Br, I, or mixture of Br and I) QDs, more iodide as the anion composition, faster the charge transfer rates tend to be; 3) Reducing the size of $CsPbI_3$ QDs can accelerate the charge transfer (both CS and CR) rates, in which case, the electronic coupling strength increase is the main contributor instead of the driving force change.

By studying TA and PL decay of QD-metal oxide mesoporous films, we obtain some insights on the charge carrier behavior of $CsPbI_3$ QDs related to solid state devices: 1) Interfacial charge transfer rates are sensitive to the property of metal oxide. TiO_2, compared with ZnO, favors faster electron transfer and charge recombination between $CsPbI_3$ QDs and the electron extraction layer; 2) Using MeOAc wash to remove most QD surface ligands in solution before device fabrication may improve the PCE because the CS rate between $CsPbI_3$ QDs and TiO_2 will increase but the CR process will be slower.

Above all, reflecting on the influencing factors mentioned in Chapter 1, we have investigated the influences of chemical composition (anion dependence, Chapter 4), morphology (size dependence, Chapter 5), property of electron acceptor (metal oxide type dependence, Chapter 6) and interfacial contact (ligand quantity dependence, Chapter 7). Also mentioned in Chapter 1, these factors may not be independent mutually. For example, when we change the anion composition of QDs, the size will also change, thus complicating the influence factors on charge transfer rates. Another example is in Chapter 7, when we try to study the ligand quantity dependent CT. Although the results seem supporting that with less ligand quantity, electron can transfer faster from QDs to TiO_2, we cannot explain why the CR rate can be slower with less ligands. Some other factors must function in this case, such as surface rearrangement during the MeOAc washing and/or the adsorption onto films. We do not have direct evidence for the existence or inexistence of ligands at the interface between QD and TiO_2. But thermodynamically, the hydrophobic C-H chains of ligands (OA/OAm) should be prone to point to the air instead of to contact with the ionic surface. Therefore, we speculate the quantity of ligands at the interface between QD and TiO_2 may be negligible. That is why we can only conclude that post-synthesis treatments influence the CT rates in films, not that the ligand quantity, at least not the interfacial ligand quantity, influences the CT rates. As to how on earth the post-synthesis treatments influence the charge carrier dynamics, it is too complicated and beyond the scope of Chapter 7. Further progress is required.

In addition, another two points about the experimental studies need some clarifications here.

First, initially in solution phase study, we used sonication method (see Chapter 2) to attach RhB on QDs in the anion dependent study. Years later, when studying the size dependent CT, we found too much RhB would be adsorbed onto the QDs if we used the same sonication method, probably due to sample variations. The QD-RhB complexes with too much RhB would lead to QDs aggregation within experimental time, as reflected in the UV-Vis spectra. So, in Chapter 5, we used the solution mixing method to add RhB to QDs and conducted TA study of a series of QD-RhB samples to obtain the intrinsic CS time constants.

The second point is about the experiments in film studies. We first used the Al_2O_3 nanoparticle films as control, like in Chapter 6. But the texture of Al_2O_3 films is very different from the TiO_2 films. The disadvantages are that Al_2O_3 films are not uniform and usually cannot adsorb enough quantity of QDs like TiO_2 films. Later we adopted ALD TiO_2 films as controls, which are as uniform as TiO_2 films and can adsorb QDs sufficiently. Notably, the ALD TiO_2 films can adsorb more QDs than TiO_2 (Figure

7.3). The possible reasons might be: 1) Al_2O_3 surface is less repulsive to the hydrophobic ligands on QDs than TiO_2; or 2) Because TiO_2 film adsorbs more ligands (Figure A.7.1), less sites are left for QD adsorption; Or the combination of above two reasons.

Overall, we have conducted above experimental research on charge transfer dynamics in $CsPbI_3$ QDs. The insights from these studies may not help $CsPbI_3$ QDs become a superior photovoltaic material over all other candidates. But we do reveal the unique properties of intrinsic charge carrier and charge transfer processes in $CsPbI_3$ QDs. Understanding the uniqueness of the material is the basis for better and further exploitation of the material, just as understanding the uniqueness of reality is the basis for a brighter future.

References

1. Kojima, A.; Teshima, K.; Shirai, Y.; Miyasaka, T., Organometal Halide Perovskites as Visible-Light Sensitizers for Photovoltaic Cells. *Journal of the American Chemical Society* **2009,** *131* (17), 6050-6051.
2. Best Research-Cell Efficiency Chart. *https://www.nrel.gov/pv/cell-efficiency.html*.
3. Li, B.; Li, Y.; Zheng, C.; Gao, D.; Huang, W., Advancements in the stability of perovskite solar cells: degradation mechanisms and improvement approaches. *RSC Adv.* **2016,** *6* (44), 38079-38091.
4. Saliba, M.; Matsui, T.; Domanski, K.; Seo, J.-Y.; Ummadisingu, A.; Zakeeruddin, S. M.; Correa-Baena, J.-P.; Tress, W. R.; Abate, A.; Hagfeldt, A.; Grätzel, M., Incorporation of rubidium cations into perovskite solar cells improves photovoltaic performance. *Science* **2016**.
5. Saliba, M.; Matsui, T.; Seo, J. Y.; Domanski, K.; Correa-Baena, J. P.; Nazeeruddin, M. K.; Zakeeruddin, S. M.; Tress, W.; Abate, A.; Hagfeldt, A.; Gratzel, M., Cesium-containing triple cation perovskite solar cells: improved stability, reproducibility and high efficiency. *Energy Environ Sci* **2016,** *9* (6), 1989-1997.
6. McMeekin, D. P.; Sadoughi, G.; Rehman, W.; Eperon, G. E.; Saliba, M.; Hörantner, M. T.; Haghighirad, A.; Sakai, N.; Korte, L.; Rech, B.; Johnston, M. B.; Herz, L. M.; Snaith, H. J., A mixed-cation lead mixed-halide perovskite absorber for tandem solar cells. *Science* **2016,** *351* (6269), 151-155.
7. Swarnkar, A.; Marshall, A. R.; Sanehira, E. M.; Chernomordik, B. D.; Moore, D. T.; Christians, J. A.; Chakrabarti, T.; Luther, J. M., Quantum dot–induced phase stabilization of α-$CsPbI_3$ perovskite for high-efficiency photovoltaics. *Science* **2016,** *354* (6308), 92-95.
8. Eperon, G. E.; Paterno, G. M.; Sutton, R. J.; Zampetti, A.; Haghighirad, A. A.; Cacialli, F.; Snaith, H. J., Inorganic caesium lead iodide perovskite solar cells. *Journal of Materials Chemistry A* **2015,** *3* (39), 19688-19695.
9. Beal, R. E.; Slotcavage, D. J.; Leijtens, T.; Bowring, A. R.; Belisle, R. A.; Nguyen, W. H.; Burkhard, G. F.; Hoke, E. T.; McGehee, M. D., Cesium Lead Halide Perovskites with Improved Stability for Tandem Solar Cells. *The Journal of Physical Chemistry Letters* **2016,** *7* (5), 746-751.
10. Wang, K.; Jin, Z.; Liang, L.; Bian, H.; Bai, D.; Wang, H.; Zhang, J.; Wang, Q.; Shengzhong, L., All-inorganic cesium lead iodide perovskite solar cells with stabilized efficiency beyond 15. *Nat Commun* **2018,** *9* (1), 4544.
11. Wang, Y.; Zhang, T.; Kan, M.; Zhao, Y., Bifunctional Stabilization of All-Inorganic alpha-CsPbI3 Perovskite for 17% Efficiency Photovoltaics. *J Am Chem Soc* **2018,** *140* (39), 12345-12348.
12. Sanehira, E. M.; Marshall, A. R.; Christians, J. A.; Harvey, S. P.; Ciesielski, P. N.; Wheeler, L. M.; Schulz, P.; Lin, L. Y.; Beard, M. C.; Luther, J. M., Enhanced mobility $CsPbI_3$ quantum dot arrays for record-efficiency, high-voltage photovoltaic cells. *Science Advances* **2017,** *3* (10).
13. Marcus, R. A.; Sutin, N., Electron transfers in chemistry and biology. *Biochimica et Biophysica Acta (BBA) - Reviews on Bioenergetics* **1985,** *811* (3), 265-322.
14. Zhang, F.; Zhong, H.; Chen, C.; Wu, X.-g.; Hu, X.; Huang, H.; Han, J.; Zou, B.; Dong, Y., Brightly Luminescent and Color-Tunable Colloidal CH3NH3PbX3 (X = Br, I, Cl) Quantum Dots: Potential Alternatives for Display Technology. *ACS Nano* **2015,** *9* (4), 4533-4542.
15. Protesescu, L.; Yakunin, S.; Bodnarchuk, M. I.; Bertolotti, F.; Masciocchi, N.; Guagliardi, A.; Kovalenko, M. V., Monodisperse Formamidinium Lead Bromide Nanocrystals with Bright and Stable Green Photoluminescence. *J Am Chem Soc* **2016**.
16. Chen, L.-J.; Lee, C.-R.; Chuang, Y.-J.; Wu, Z.-H.; Chen, C., Synthesis and Optical Properties of Lead-Free Cesium Tin Halide Perovskite Quantum Rods with High-Performance Solar Cell Application. *The Journal of Physical Chemistry Letters* **2016**, 5028-5035.

17. Liu, F.; Ding, C.; Zhang, Y.; Ripolles, T. S.; Kamisaka, T.; Toyoda, T.; Hayase, S.; Minemoto, T.; Yoshino, K.; Dai, S.; Yanagida, M.; Noguchi, H.; Shen, Q., Colloidal Synthesis of Air-Stable Alloyed CsSn1-xPbxI3 Perovskite Nanocrystals for Use in Solar Cells. *J Am Chem Soc* **2017**.

18. Akkerman, Q. A.; Meggiolaro, D.; Dang, Z.; De Angelis, F.; Manna, L., Fluorescent Alloy CsPbxMn1–xI3 Perovskite Nanocrystals with High Structural and Optical Stability. *ACS Energy Letters* **2017,** *2* (9), 2183-2186.

19. Akkerman, Q. A.; D'Innocenzo, V.; Accornero, S.; Scarpellini, A.; Petrozza, A.; Prato, M.; Manna, L., Tuning the Optical Properties of Cesium Lead Halide Perovskite Nanocrystals by Anion Exchange Reactions. *Journal of the American Chemical Society* **2015,** *137* (32), 10276-10281.

20. Nedelcu, G.; Protesescu, L.; Yakunin, S.; Bodnarchuk, M. I.; Grotevent, M. J.; Kovalenko, M. V., Fast Anion-Exchange in Highly Luminescent Nanocrystals of Cesium Lead Halide Perovskites (CsPbX3, X = Cl, Br, I). *Nano Letters* **2015,** *15* (8), 5635-5640.

21. Brus, L. E., Electron–electron and electron‐hole interactions in small semiconductor crystallites: The size dependence of the lowest excited electronic state. *The Journal of Chemical Physics* **1984,** *80* (9), 4403-4409.

22. Lin, J.; Gomez, L.; de Weerd, C.; Fujiwara, Y.; Gregorkiewicz, T.; Suenaga, K., Direct observation of bandstructure modifications in nanocrystals of CsPbBr3 perovskite. *Nano Lett* **2016**.

23. Brennan, M. C.; Herr, J. E.; Nguyen-Beck, T. S.; Zinna, J.; Draguta, S.; Rouvimov, S.; Parkhill, J.; Kuno, M., Origin of the Size-Dependent Stokes Shift in CsPbBr3 Perovskite Nanocrystals. *J Am Chem Soc* **2017,** *139* (35), 12201-12208.

24. Zhu, H.; Yang, Y.; Hyeon-Deuk, K.; Califano, M.; Song, N.; Wang, Y.; Zhang, W.; Prezhdo, O. V.; Lian, T., Auger-assisted electron transfer from photoexcited semiconductor quantum dots. *Nano Lett* **2014,** *14* (3), 1263-9.

25. Tvrdy, K.; Frantsuzov, P. A.; Kamat, P. V., Photoinduced electron transfer from semiconductor quantum dots to metal oxide nanoparticles. *Proc Natl Acad Sci U S A* **2011,** *108* (1), 29-34.

26. CLOSS, G. L.; MILLER, J. R., Intramolecular Long-Distance Electron Transfer in Organic Molecules. *Science* **1988,** *240* (4851), 440-447.

27. Asbury, J. B.; Hao, E.; Wang, Y.; Lian, T., Bridge Length-Dependent Ultrafast Electron Transfer from Re Polypyridyl Complexes to Nanocrystalline TiO2 Thin Films Studied by Femtosecond Infrared Spectroscopy. *The Journal of Physical Chemistry B* **2000,** *104* (50), 11957-11964.

28. Yang, Y.; Qin, H.; Jiang, M.; Lin, L.; Fu, T.; Dai, X.; Zhang, Z.; Niu, Y.; Cao, H.; Jin, Y.; Zhao, F.; Peng, X., Entropic Ligands for Nanocrystals: From Unexpected Solution Properties to Outstanding Processability. *Nano Lett* **2016,** *16* (4), 2133-8.

29. Asbury, J. B.; Hao, E.; Wang, Y.; Ghosh, H. N.; Lian, T., Ultrafast Electron Transfer Dynamics from Molecular Adsorbates to Semiconductor Nanocrystalline Thin Films. *The Journal of Physical Chemistry B* **2001,** *105* (20), 4545-4557.

30. Anderson, N. A.; Lian, T., Ultrafast electron injection from metal polypyridyl complexes to metal-oxide nanocrystalline thin films. *Coordination Chemistry Reviews* **2004,** *248* (13–14), 1231-1246.

31. Wu, K.; Liang, G.; Shang, Q.; Ren, Y.; Kong, D.; Lian, T., Ultrafast Interfacial Electron and Hole Transfer from CsPbBr3 Perovskite Quantum Dots. *Journal of the American Chemical Society* **2015,** *137* (40), 12792-12795.

32. Jung, E. H.; Jeon, N. J.; Park, E. Y.; Moon, C. S.; Shin, T. J.; Yang, T. Y.; Noh, J. H.; Seo, J., Efficient, stable and scalable perovskite solar cells using poly(3-hexylthiophene). *Nature* **2019,** *567* (7749), 511-515.

33. Duan, J.; Zhao, Y.; He, B.; Tang, Q., High-Purity Inorganic Perovskite Films for Solar Cells with 9.72 % Efficiency. *Angew Chem Int Ed Engl* **2018**.

34. Yang, W. S.; Park, B.-W.; Jung, E. H.; Jeon, N. J.; Kim, Y. C.; Lee, D. U.; Shin, S. S.; Seo, J.; Kim, E. K.; Noh, J. H.; Seok, S. I., Iodide management in formamidinium-lead-halide–based perovskite layers for efficient solar cells. *Science* **2017,** *356* (6345), 1376-1379.

35. Grancini, G.; Roldan-Carmona, C.; Zimmermann, I.; Mosconi, E.; Lee, X.; Martineau, D.; Narbey, S.; Oswald, F.; De Angelis, F.; Graetzel, M.; Nazeeruddin, M. K., One-Year stable perovskite solar cells by 2D/3D interface engineering. *Nat Commun* **2017,** *8*, 15684.

36. Chen, H.; Ye, F.; Tang, W.; He, J.; Yin, M.; Wang, Y.; Xie, F.; Bi, E.; Yang, X.; Gratzel, M.; Han, L., A solvent- and vacuum-free route to large-area perovskite films for efficient solar modules. *Nature* **2017**.

37. Arora, N.; Dar, M. I.; Hinderhofer, A.; Pellet, N.; Schreiber, F.; Zakeeruddin, S. M.; Grätzel, M., Perovskite solar cells with CuSCN hole extraction layers yield stabilized efficiencies greater than 20%. *Science* **2017**.

38. Saliba, M.; Matsui, T.; Domanski, K.; Seo, J.-Y.; Ummadisingu, A.; Zakeeruddin, S. M.; Correa-Baena, J.-P.; Tress, W. R.; Abate, A.; Hagfeldt, A.; Grätzel, M., Incorporation of rubidium cations into perovskite solar cells improves photovoltaic performance. *Science* **2016,** *354* (6309), 206-209.

39. Li, X.; Bi, D.; Yi, C.; Décoppet, J.-D.; Luo, J.; Zakeeruddin, S. M.; Hagfeldt, A.; Grätzel, M., A vacuum flash–assisted solution process for high-efficiency large-area perovskite solar cells. *Science* **2016,** *353* (6294), 58-62.

40. Bella, F.; Griffini, G.; Correa-Baena, J.-P.; Saracco, G.; Grätzel, M.; Hagfeldt, A.; Turri, S.; Gerbaldi, C., Improving efficiency and stability of perovskite solar cells with photocurable fluoropolymers. *Science* **2016**.

41. Yang, W. S.; Noh, J. H.; Jeon, N. J.; Kim, Y. C.; Ryu, S.; Seo, J.; Seok, S. I., High-performance photovoltaic perovskite layers fabricated through intramolecular exchange. *Science* **2015,** *348* (6240), 1234-1237.

42. Jeon, N. J.; Noh, J. H.; Yang, W. S.; Kim, Y. C.; Ryu, S.; Seo, J.; Seok, S. I., Compositional engineering of perovskite materials for high-performance solar cells. *Nature* **2015,** *517* (7535), 476-480.

43. Mei, A.; Li, X.; Liu, L.; Ku, Z.; Liu, T.; Rong, Y.; Xu, M.; Hu, M.; Chen, J.; Yang, Y.; Grätzel, M.; Han, H., A hole-conductor–free, fully printable mesoscopic perovskite solar cell with high stability. *Science* **2014,** *345* (6194), 295-298.

44. Burschka, J.; Pellet, N.; Moon, S. J.; Humphry-Baker, R.; Gao, P.; Nazeeruddin, M. K.; Gratzel, M., Sequential deposition as a route to high-performance perovskite-sensitized solar cells. *Nature* **2013,** *499* (7458), 316-9.

45. Lee, M. M.; Teuscher, J.; Miyasaka, T.; Murakami, T. N.; Snaith, H. J., Efficient Hybrid Solar Cells Based on Meso-Superstructured Organometal Halide Perovskites. *Science* **2012,** *338* (6107), 643-647.

46. Protesescu, L.; Yakunin, S.; Bodnarchuk, M. I.; Krieg, F.; Caputo, R.; Hendon, C. H.; Yang, R. X.; Walsh, A.; Kovalenko, M. V., Nanocrystals of Cesium Lead Halide Perovskites ($CsPbX_3$, X = Cl, Br, and I): Novel Optoelectronic Materials Showing Bright Emission with Wide Color Gamut. *Nano Letters* **2015,** *15* (6), 3692-3696.

47. Nan, W.; Niu, Y.; Qin, H.; Cui, F.; Yang, Y.; Lai, R.; Lin, W.; Peng, X., Crystal Structure Control of Zinc-Blende CdSe/CdS Core/Shell Nanocrystals: Synthesis and Structure-Dependent Optical Properties. *Journal of the American Chemical Society* **2012,** *134* (48), 19685-19693.

48. Gao, Y.; Peng, X., Crystal Structure Control of CdSe Nanocrystals in Growth and Nucleation: Dominating Effects of Surface versus Interior Structure. *Journal of the American Chemical Society* **2014,** *136* (18), 6724-6732.

49. Wu, K.; Liu, Z.; Zhu, H.; Lian, T., Exciton annihilation and dissociation dynamics in group II-V Cd3P2 quantum dots. *J Phys Chem A* **2013,** *117* (29), 6362-72.

50. Yu, W. W.; Qu, L.; Guo, W.; Peng, X., Experimental Determination of the Extinction Coefficient of CdTe, CdSe, and CdS Nanocrystals. *Chemistry of Materials* **2003,** *15* (14), 2854-2860.

51. Boulesbaa, A.; Issac, A.; Stockwell, D.; Huang, Z.; Huang, J.; Guo, J.; Lian, T., Ultrafast Charge Separation at CdS Quantum Dot/Rhodamine B Molecule Interface. *Journal of the American Chemical Society* **2007,** *129* (49), 15132-15133.

52. Jin, M.; Hong, H.; Xie, J.; Malval, J.-P.; Spangenberg, A.; Soppera, O.; Wan, D.; Pu, H.; Versace, D.-L.; Leclerc, T.; Baldeck, P.; Poizat, O.; Knopf, S., [small pi]-conjugated sulfonium-based photoacid generators: an integrated molecular approach for efficient one and two-photon polymerization. *Polymer Chemistry* **2014,** *5* (16), 4747-4755.

53. Zhu, H.; Song, N.; Lian, T., Controlling Charge Separation and Recombination Rates in CdSe/ZnS Type I Core−Shell Quantum Dots by Shell Thicknesses. *Journal of the American Chemical Society* **2010,** *132* (42), 15038-15045.

54. Huang, J.; Huang, Z.; Jin, S.; Lian, T., Exciton Dissociation in CdSe Quantum Dots by Hole Transfer to Phenothiazine. *The Journal of Physical Chemistry C* **2008,** *112* (49), 19734-19738.

55. Morris-Cohen, A. J.; Frederick, M. T.; Cass, L. C.; Weiss, E. A., Simultaneous Determination of the Adsorption Constant and the Photoinduced Electron Transfer Rate for a Cds Quantum Dot–Viologen Complex. *Journal of the American Chemical Society* **2011,** *133* (26), 10146-10154.

56. Wu, K.; Du, Y.; Tang, H.; Chen, Z.; Lian, T., Efficient Extraction of Trapped Holes from Colloidal CdS Nanorods. *J Am Chem Soc* **2015,** *137* (32), 10224-30.

57. Ai, X.; Anderson, N. A.; Guo, J.; Lian, T., Electron Injection Dynamics of Ru Polypyridyl Complexes on SnO2 Nanocrystalline Thin Films. *The Journal of Physical Chemistry B* **2005,** *109* (15), 7088-7094.

58. She, C.; Anderson, N. A.; Guo, J.; Liu, F.; Goh, W.-H.; Chen, D.-T.; Mohler, D. L.; Tian, Z.-Q.; Hupp, J. T.; Lian, T., pH-Dependent Electron Transfer from Re-bipyridyl Complexes to Metal Oxide Nanocrystalline Thin Films. *The Journal of Physical Chemistry B* **2005,** *109* (41), 19345-19355.

59. Makarov, N. S.; Guo, S.; Isaienko, O.; Liu, W.; Robel, I.; Klimov, V. I., Spectral and Dynamical Properties of Single Excitons, Biexcitons, and Trions in Cesium–Lead-Halide Perovskite Quantum Dots. *Nano Letters* **2016**.

60. Kane, E. O., Energy band structure in p-type germanium and silicon. *Journal of Physics and Chemistry of Solids* **1956,** *1* (1), 82-99.

61. Kane, E. O., Band structure of indium antimonide. *Journal of Physics and Chemistry of Solids* **1957,** *1* (4), 249-261.

62. Kane, E. O., The semi-empirical approach to band structure. *Journal of Physics and Chemistry of Solids* **1959,** *8*, 38-44.

63. Schulz, P.; Edri, E.; Kirmayer, S.; Hodes, G.; Cahen, D.; Kahn, A., Interface energetics in organo-metal halide perovskite-based photovoltaic cells. *Energy & Environmental Science* **2014,** *7* (4), 1377-1381.

64. Stoumpos, C. C.; Malliakas, C. D.; Peters, J. A.; Liu, Z.; Sebastian, M.; Im, J.; Chasapis, T. C.; Wibowo, A. C.; Chung, D. Y.; Freeman, A. J.; Wessels, B. W.; Kanatzidis, M. G., Crystal Growth of the Perovskite Semiconductor CsPbBr3: A New Material for High-Energy Radiation Detection. *Crystal Growth & Design* **2013,** *13* (7), 2722-2727.

65. Ripolles, T. S.; Nishinaka, K.; Ogomi, Y.; Miyata, Y.; Hayase, S., Efficiency enhancement by changing perovskite crystal phase and adding a charge extraction interlayer in organic amine free-perovskite solar cells based on cesium. *Solar Energy Materials and Solar Cells* **2016,** *144*, 532-536.

66. Kitazawa, N.; Watanabe, Y.; Nakamura, Y., Optical properties of CH3NH3PbX3 (X = halogen) and their mixed-halide crystals. *Journal of Materials Science 37* (17), 3585-3587.

67. Stamplecoskie, K. G.; Manser, J. S.; Kamat, P. V., Dual nature of the excited state in organic-inorganic lead halide perovskites. *Energy & Environmental Science* **2015,** *8* (1), 208-215.

68. Kovalenko, M. V.; Protesescu, L.; Bodnarchuk, M. I., Properties and potential optoelectronic applications of lead halide perovskite nanocrystals. *Science* **2017,** *358* (6364), 745-750.

69. Zhang, Z.; Chen, Z.; Yuan, L.; Chen, W.; Yang, J.; Wang, B.; Wen, X.; Zhang, J.; Hu, L.; Stride, J. A.; Conibeer, G. J.; Patterson, R. J.; Huang, S., A New Passivation Route Leading to Over 8% Efficient PbSe Quantum-Dot Solar Cells via Direct Ion Exchange with Perovskite Nanocrystals. *Adv Mater* **2017**.

70. Song, J.; Li, J.; Li, X.; Xu, L.; Dong, Y.; Zeng, H., Quantum Dot Light-Emitting Diodes Based on Inorganic Perovskite Cesium Lead Halides (CsPbX3). *Advanced Materials* **2015**, n/a-n/a.

71. Li, G.; Rivarola, F. W.; Davis, N. J.; Bai, S.; Jellicoe, T. C.; de la Pena, F.; Hou, S.; Ducati, C.; Gao, F.; Friend, R. H.; Greenham, N. C.; Tan, Z. K., Highly Efficient Perovskite Nanocrystal Light-Emitting Diodes Enabled by a Universal Crosslinking Method. *Adv Mater* **2016,** *28* (18), 3528-34.

72. Li, J.; Xu, L.; Wang, T.; Song, J.; Chen, J.; Xue, J.; Dong, Y.; Cai, B.; Shan, Q.; Han, B.; Zeng, H., 50-Fold EQE Improvement up to 6.27% of Solution-Processed All-Inorganic Perovskite CsPbBr3 QLEDs via Surface Ligand Density Control. *Adv Mater* **2016**.

73. Li, X.; Wu, Y.; Zhang, S.; Cai, B.; Gu, Y.; Song, J.; Zeng, H., CsPbX3 Quantum Dots for Lighting and Displays: Room-Temperature Synthesis, Photoluminescence Superiorities, Underlying Origins and White Light-Emitting Diodes. *Advanced Functional Materials* **2016,** *26* (15), 2435-2445.

74. Pan, J.; Quan, L. N.; Zhao, Y.; Peng, W.; Murali, B.; Sarmah, S. P.; Yuan, M.; Sinatra, L.; Alyami, N. M.; Liu, J.; Yassitepe, E.; Yang, Z.; Voznyy, O.; Comin, R.; Hedhili, M. N.; Mohammed, O. F.; Lu, Z. H.; Kim, D. H.; Sargent, E. H.; Bakr, O. M., Highly Efficient Perovskite-Quantum-Dot Light-Emitting Diodes by Surface Engineering. *Adv Mater* **2016,** *28* (39), 8718-8725.

75. Zhang, X.; Lin, H.; Huang, H.; Reckmeier, C.; Zhang, Y.; Choy, W. C. H.; Rogach, A. L., Enhancing the Brightness of Cesium Lead Halide Perovskite Nanocrystal Based Green Light-Emitting Devices through the Interface Engineering with Perfluorinated Ionomer. *Nano Letters* **2016,** *16* (2), 1415-1420.

76. Zhang, X.; Sun, C.; Zhang, Y.; Wu, H.; Ji, C.; Chuai, Y.; Wang, P.; Wen, S.; Zhang, C.; Yu, W. W., Bright Perovskite Nanocrystal Films for Efficient Light-Emitting Devices. *J Phys Chem Lett* **2016**.

77. Yao, E. P.; Yang, Z.; Meng, L.; Sun, P.; Dong, S.; Yang, Y.; Yang, Y., High-Brightness Blue and White LEDs based on Inorganic Perovskite Nanocrystals and their Composites. *Adv Mater* **2017,** *29* (23).

78. Zhang, S.; Yi, C.; Wang, N.; Sun, Y.; Zou, W.; Wei, Y.; Cao, Y.; Miao, Y.; Li, R.; Yin, Y.; Zhao, N.; Wang, J.; Huang, W., Efficient Red Perovskite Light-Emitting Diodes Based on Solution-Processed Multiple Quantum Wells. *Adv Mater* **2017,** *29* (22).

79. Zhang, X.; Xu, B.; Wang, W.; Liu, S.; Zheng, Y.; Chen, S.; Wang, K.; Sun, X. W., Plasmonic Perovskite Light-Emitting Diodes Based on the Ag-CsPbBr3 System. *ACS Appl Mater Interfaces* **2017,** *9* (5), 4926-4931.

80. Zou, S.; Liu, Y.; Li, J.; Liu, C.; Feng, R.; Jiang, F.; Li, Y.; Song, J.; Zeng, H.; Hong, M.; Chen, X., Stabilizing Cesium Lead Halide Perovskite Lattice through Mn(II) Substitution for Air-Stable Light-Emitting Diodes. *J Am Chem Soc* **2017,** *139* (33), 11443-11450.

81. Yakunin, S.; Protesescu, L.; Krieg, F.; Bodnarchuk, M. I.; Nedelcu, G.; Humer, M.; De Luca, G.; Fiebig, M.; Heiss, W.; Kovalenko, M. V., Low-threshold amplified spontaneous emission and lasing from colloidal nanocrystals of caesium lead halide perovskites. *Nat Commun* **2015,** *6*.

82. Xu, Y.; Chen, Q.; Zhang, C.; Wang, R.; Wu, H.; Zhang, X.; Xing, G.; Yu, W. W.; Wang, X.; Zhang, Y.; Xiao, M., Two-Photon-Pumped Perovskite Semiconductor Nanocrystal Lasers. *Journal of the American Chemical Society* **2016,** *138* (11), 3761-3768.

83. Zhang, Q.; Su, R.; Liu, X.; Xing, J.; Sum, T. C.; Xiong, Q., High-Quality Whispering-Gallery-Mode Lasing from Cesium Lead Halide Perovskite Nanoplatelets. *Advanced Functional Materials* **2016**, n/a-n/a.

84. Wang, Y.; Li, X.; Nalla, V.; Zeng, H.; Sun, H., Solution-Processed Low Threshold Vertical Cavity Surface Emitting Lasers from All-Inorganic Perovskite Nanocrystals. *Advanced Functional Materials* **2017**, 1605088.

85. Meinardi, F.; Akkerman, Q. A.; Bruni, F.; Park, S.; Mauri, M.; Dang, Z.; Manna, L.; Brovelli, S., Doped Halide Perovskite Nanocrystals for Reabsorption-Free Luminescent Solar Concentrators. *ACS Energy Letters* **2017,** *2* (10), 2368-2377.

86. Xu, Y. F.; Yang, M. Z.; Chen, B. X.; Wang, X. D.; Chen, H. Y.; Kuang, D. B.; Su, C. Y., A CsPbBr3 Perovskite Quantum Dot/Graphene Oxide Composite for Photocatalytic CO2 Reduction. *J Am Chem Soc* **2017**.

87. Parobek, D.; Dong, Y.; Qiao, T.; Rossi, D.; Son, D. H., Photoinduced Anion Exchange in Cesium Lead Halide Perovskite Nanocrystals. *J Am Chem Soc* **2017**.

88. Kramer, I. J.; Sargent, E. H., The Architecture of Colloidal Quantum Dot Solar Cells: Materials to Devices. *Chemical Reviews* **2014,** *114* (1), 863-882.

89. Carey, G. H.; Abdelhady, A. L.; Ning, Z.; Thon, S. M.; Bakr, O. M.; Sargent, E. H., Colloidal Quantum Dot Solar Cells. *Chemical Reviews* **2015**.

90. Zhu, H.; Yang, Y.; Wu, K.; Lian, T., Charge Transfer Dynamics from Photoexcited Semiconductor Quantum Dots. *Annual Review of Physical Chemistry* **2016,** *67* (1), null.

91. Marchioro, A.; Teuscher, J.; Friedrich, D.; Kunst, M.; van de Krol, R.; Moehl, T.; Gratzel, M.; Moser, J.-E., Unravelling the mechanism of photoinduced charge transfer processes in lead iodide perovskite solar cells. *Nat Photon* **2014,** *8* (3), 250-255.

92. Tan, H.; Jain, A.; Voznyy, O.; Lan, X.; García de Arquer, F. P.; Fan, J. Z.; Quintero-Bermudez, R.; Yuan, M.; Zhang, B.; Zhao, Y.; Fan, F.; Li, P.; Quan, L. N.; Zhao, Y.; Lu, Z.-H.; Yang, Z.; Hoogland, S.; Sargent, E. H., Efficient and stable solution-processed planar perovskite solar cells via contact passivation. *Science* **2017**.

93. Robel, I.; Kuno, M.; Kamat, P. V., Size-Dependent Electron Injection from Excited CdSe Quantum Dots into TiO2 Nanoparticles. *Journal of the American Chemical Society* **2007,** *129* (14), 4136-4137.

94. Makarov, N. S.; Guo, S.; Isaienko, O.; Liu, W.; Robel, I.; Klimov, V. I., Spectral and Dynamical Properties of Single Excitons, Biexcitons, and Trions in Cesium–Lead-Halide Perovskite Quantum Dots. *Nano Letters* **2016,** *16* (4), 2349-2362.

95. Marcus, R. A., Chemical and Electrochemical Electron-Transfer Theory. *Annual Review of Physical Chemistry* **1964,** *15* (1), 155-196.

96. Becke, A. D., Density-functional exchange-energy approximation with correct asymptotic behavior. *Physical Review A* **1988,** *38* (6), 3098-3100.

97. Lee, C.; Yang, W.; Parr, R. G., Development of the Colle-Salvetti correlation-energy formula into a functional of the electron density. *Physical Review B* **1988,** *37* (2), 785-789.

98. Frisch, M. J. T., G. W.; Schlegel, H. B.; Scuseria, G. E.; Robb, M. A.; Cheeseman, J. R.; Scalmani, G.; Barone, V.; Mennucci, B.; Petersson, G. A.; Nakatsuji, H.; Caricato, M.; Li, X.; Hratchian, H. P.; Izmaylov, A. F.; Bloino, J.; Zheng, G.; Sonnenberg, J. L.; Hada, M.; Ehara, M.; Toyota, K.; Fukuda, R.; Hasegawa, J.; Ishida, M.; Nakajima, T.; Honda, Y.; Kitao, O.; Nakai, H.; Vreven, T.; Montgomery, J. A., Jr.; Peralta, J. E.; Ogliaro, F.; Bearpark, M.; Heyd, J. J.; Brothers, E.; Kudin, K. N.; Staroverov, V. N.; Kobayashi, R.; Normand, J.; Raghavachari, K.; Rendell, A.; Burant, J. C.; Iyengar, S. S.; Tomasi, J.; Cossi, M.; Rega, N.; Millam, M. J.; Klene, M.; Knox, J. E.; Cross, J. B.; Bakken, V.; Adamo, C.; Jaramillo, J.; Gomperts, R.; Stratmann, R. E.; Yazyev, O.; Austin, A. J.; Cammi, R.; Pomelli, C.; Ochterski, J. W.; Martin, R. L.; Morokuma, K.; Zakrzewski, V. G.; Voth, G. A.; Salvador, P.; Dannenberg, J. J.; Dapprich, S.; Daniels, A. D.; Farkas, Ö.; Foresman, J. B.; Ortiz, J. V.; Cioslowski, J.; Fox, D. J., Gaussian 09, Revision D.01. *Gaussian, Inc., Wallingford CT* **2009**.

99. Fischer, A. B.; Bronstein-Bonte, I., Photoinduced electron transfer quenching of rhodamine B in polymer films. *Journal of Photochemistry* **1985,** *30* (4), 475-485.

100. Park, Y.-S.; Guo, S.; Makarov, N. S.; Klimov, V. I., Room Temperature Single-Photon Emission from Individual Perovskite Quantum Dots. *ACS Nano* **2015,** *9* (10), 10386-10393.

101. Noh, J. H.; Im, S. H.; Heo, J. H.; Mandal, T. N.; Seok, S. I., Chemical Management for Colorful, Efficient, and Stable Inorganic–Organic Hybrid Nanostructured Solar Cells. *Nano Letters* **2013,** *13* (4), 1764-1769.

102. Ravi, V. K.; Markad, G. B.; Nag, A., Band Edge Energies and Excitonic Transition Probabilities of Colloidal CsPbX3(X = Cl, Br, I) Perovskite Nanocrystals. *ACS Energy Letters* **2016**, 665-671.

103. Xu, Y.; Schoonen Martin, A. A., The absolute energy positions of conduction and valence bands of selected semiconducting minerals. In *American Mineralogist*, 2000; Vol. 85, p 543.

104. Yang, Y.; Rodriguez-Cordoba, W.; Xiang, X.; Lian, T., Strong electronic coupling and ultrafast electron transfer between PbS quantum dots and TiO2 nanocrystalline films. *Nano Lett* **2012,** *12* (1), 303-9.

105. Ai, X.; Guo, J.; Anderson, N. A.; Lian, T., Ultrafast Electron Transfer from Ru Polypyridyl Complexes to Nb2O5 Nanoporous Thin Films. *The Journal of Physical Chemistry B* **2004,** *108* (34), 12795-12803.

106. Zidek, K.; Zheng, K.; Ponseca, C. S., Jr.; Messing, M. E.; Wallenberg, L. R.; Chabera, P.; Abdellah, M.; Sundstrom, V.; Pullerits, T., Electron transfer in quantum-dot-sensitized ZnO nanowires: ultrafast time-resolved absorption and terahertz study. *J Am Chem Soc* **2012,** *134* (29), 12110-7.

107. Guijarro, N.; Lana-Villarreal, T.; Shen, Q.; Toyoda, T.; Gómez, R., Sensitization of Titanium Dioxide Photoanodes with Cadmium Selenide Quantum Dots Prepared by SILAR: Photoelectrochemical and Carrier Dynamics Studies. *The Journal of Physical Chemistry C* **2010,** *114* (50), 21928-21937.

108. Polman, A.; Knight, M.; Garnett, E. C.; Ehrler, B.; Sinke, W. C., Photovoltaic materials: Present efficiencies and future challenges. *Science* **2016,** *352* (6283).

109. Ponseca, C. S.; Savenije, T. J.; Abdellah, M.; Zheng, K.; Yartsev, A.; Pascher, T.; Harlang, T.; Chabera, P.; Pullerits, T.; Stepanov, A.; Wolf, J.-P.; Sundström, V., Organometal Halide Perovskite Solar Cell Materials Rationalized: Ultrafast Charge Generation, High and Microsecond-Long Balanced Mobilities, and Slow Recombination. *Journal of the American Chemical Society* **2014,** *136* (14), 5189-5192.

110. Piatkowski, P.; Cohen, B.; Javier Ramos, F.; Di Nunzio, M.; Nazeeruddin, M. K.; Gratzel, M.; Ahmad, S.; Douhal, A., Direct monitoring of ultrafast electron and hole dynamics in perovskite solar cells. *Physical Chemistry Chemical Physics* **2015,** *17* (22), 14674-14684.

111. Pernik, D. R.; Tvrdy, K.; Radich, J. G.; Kamat, P. V., Tracking the Adsorption and Electron Injection Rates of CdSe Quantum Dots on TiO2: Linked versus Direct Attachment. *The Journal of Physical Chemistry C* **2011,** *115* (27), 13511-13519.

112. Green, M. A.; Emery, K.; Hishikawa, Y.; Warta, W.; Dunlop, E. D., Solar cell efficiency tables (Version 45). *Progress in Photovoltaics: Research and Applications* **2015,** *23* (1), 1-9.

113. Gratzel, M., The light and shade of perovskite solar cells. *Nat Mater* **2014,** *13* (9), 838-842.

114. Nazeeruddin, M. K., In retrospect: Twenty-five years of low-cost solar cells. *Nature* **2016,** *538* (7626), 463-464.

115. Boix, P. P.; Agarwala, S.; Koh, T. M.; Mathews, N.; Mhaisalkar, S. G., Perovskite Solar Cells: Beyond Methylammonium Lead Iodide. *J Phys Chem Lett* **2015,** *6* (5), 898-907.

116. Liu, F.; Zhang, Y.; Ding, C.; Toyoda, T.; Ogomi, Y.; Ripolles, T. S.; Hayase, S.; Minemoto, T.; Yoshino, K.; Dai, S.; Shen, Q., Ultrafast Electron Injection from Photoexcited Perovskite CsPbI3

QDs into TiO2 Nanoparticles with Injection Efficiency near 99%. *The Journal of Physical Chemistry Letters* **2018,** *9* (2), 294-297.

117. Scheidt, R. A.; Kerns, E.; Kamat, P. V., Interfacial Charge Transfer between Excited CsPbBr3 Nanocrystals and TiO2: Charge Injection versus Photodegradation. *J Phys Chem Lett* **2018**, 5962-5969.